UC Santa Barbara

UC Santa Barbara Electronic Theses and Dissertations

Title

Engineering Tailor-Made Polymers and Networks via Active Ester and Flow Chemistry

Permalink

https://escholarship.org/uc/item/8wz5w43v

Author

Shannon, Declan

Publication Date

2024

Peer reviewed|Thesis/dissertation

eScholarship.org Powered by the California Digital Library
University of California

UNIVERSITY OF CALIFORNIA

Santa Barbara

Engineering Tailor-Made Polymers and Networks *via* Active Ester and Flow Chemistry

A dissertation submitted in partial satisfaction of the

requirements for the degree Doctor of Philosophy

in Materials

by

Declan Patrick Shannon

Committee in charge:

Professor Craig J. Hawker, Chair

Professor Megan Valentine

Professor Christopher Bates

Professor Angela Pitenis

June 2024

The dissertation of Declan Patrick Shannon is approved.

_____

Megan Valentine

_____

Christopher Bates

_____

Angela Pitenis

_____

Craig Hawker, Committee Chair

June 2024

Engineering Tailor-Made Polymers and Networks *via* Active Ester and Flow Chemistry

Copyright © 2024

by

Declan Patrick Shannon

DEDICATION

This thesis is dedicated to several individuals, both those who have been very dear to me, and those whom I will never meet.

First and foremost, this thesis is dedicated to my family, and significantly to my grandfather, Bill Shannon. You were always as sharp as a tack, with the profound depth and breadth knowledge that comes with being a professor. You were such a critical influence during my childhood that it is hard to imagine a world without you in it. You filled roles I didn't even realize were empty and made it possible for me to shoot for the stars. I miss you terribly, but I am glad you are free from your fight with dementia. It was hard to watch your struggle, with the loss of the very abilities which made you who you are. I am relieved you are finally at peace, even if it comes with heavy sorrow at your absence.

Secondarily, there is a quote I have seen circulating online for many years: "I don't think people realize how much strength it takes to pull yourself out of a dark place mentally. So if you have done that today, or any day, I am proud of you." If you have done that – if you have pulled yourself back from the brink, or out of a deep, dark hole – this thesis is also dedicated in part to you. Grad school is a challenging time for many of us, and those struggles are exacerbated by the isolating nature of the work required for a doctorate degree. There is a quote from *The Good Place*, which while originally used in another context, I think is apt here: 'The point is, people improve when they get external love and support. How can we hold it against them when they don't?' So if you are feeling isolated or at your limit, hang in there, step back from the brink. I'm rooting for you, even if I don't know you, I support you, I believe in you.

ACKNOWLEDGEMENTS

While there are numerous people who I have to thank for getting me to the finish line of my graduate degree, first and foremost I have to thank my mom. As a single parent, she put in incredible effort to ensure I had access to opportunities in STEM. She nurtured my love of science and engineering from a young age, and really set me on this path. From the at home experiments as a kid, to the driving too and from robotics practice, and all the hours spent listening to random bits of scientific info along the way, thank you, I would not have made it here without you.

I would like to additionally express my deepest gratitude to the many excellent mentors and colleagues I have had along the way. I would especially like to thank (now) Professors Josh Moon and Yumeng Xi. You both taught me so much in vastly different but crucial areas of my graduate degree. Your inputs on how to approach problems from the engineering and synthetic perspectives have been crucial, and I deeply appreciate all the time you invested in helping me develop my skillsets as a scientist.

Additionally, I would like to thank my group members for all the wonderful discussions and feedback. In particular, I must thank Pat, Ronnie, Mike, and Lindsay. From the late nights on campus, to bonding over the many hours spent cleaning vacuum pumps, you all have been one of the best cohorts anyone could ask for. You all have been truly excellent friends, and I cannot wait to see what amazing things you will accomplish next.

Lastly and most certainly not least, I would like to thank my graduate advisor Professor Craig Hawker. Craig provided one of the most welcoming, diverse, collaborative, and engaging research environments imaginable. He has encouraged me to develop and pursue my own ideas during my Ph. D. and challenged me to push my own limits. His instruction on

clear and effective scientific communication has been invaluable, and his feedback on how to develop and approach challenging scientific problems has been excellent. Craig has not only crafted an amazing research group environment for his students and post-docs, but his high standards for scientific rigor have promoted outstanding research among his group members. I consider myself incredibly fortunate that I have been able to work in your group, and I will be forever grateful. Sincerely, thank you.

VITA OF DECLAN PATRICK SHANNON

June 2024

EDUCATION

University of California, Santa Barbara, College of Engineering 2019 – 2024
Ph.D. in Polymer Materials Synthesis and Engineering – GPA: 3.89/4.0
Research Advisor: Professor Craig Hawker

University of Michigan, Ann Arbor, College of Engineering 2015 – 2019
Bachelor of Science in Engineering – *Suma Cum Laude*, GPA 3.91/4.0
Major: Materials Science and Engineering, Minor: Physics
Research Advisor: Professor Brian Love

HONORS AND AWARDS

2023	Heeger Travel Fellowship
2018	Alfred H. White Memorial Scholarship for excellence in Materials Science
2018	Sprayregen Global Scholars Program Scholarship for academic student travel
2017	James B. Angel Scholar: Awarded for consecutive 4.0 semesters
2016	William J. Branstrom Freshman Prize awarded to top 5% of students per college
2015 – 2019	Univ. of Michigan Engineering Deans List
2015 – 2019	Univ. of Michigan Honors
2017 – 2019	Univ. of Michigan Global Scholars Program

PROFESSIONAL EMPLOYMENT

University of California, Santa Barbara – Hawker Group Santa Barbara, CA
Graduate Student Researcher 2019 – Present

- Led a team collaboration and published first author paper on engineering of catechol–PEG-acrylate films with tunable mechanical properties (up to 100x increase in Young's moduli) via iron catechol chelation. Developed methods for patterning iron inclusion, forming novel composite-like materials (**Shannon, D.** et al., Macromolecules 2023)
- Designed microfluidic flow reactor for synthesizing active ester polymer microparticles to study in-situ water diffusivity and impact of sidechain and polymer chemistry via spectroscopic methods (*pub. in prep.*)
- Tech-transfer with Mitsubishi Chemical Center for Advanced Materials to develop methods for flow synthesis of polymer materials. Key focuses included preparation of high molecular weight, low dispersity polymers via biphasic (PET-)RAFT polymerization (*patent in preparation*). Additional efforts were concentrated on flow synthesis of polyaniline materials (*patent in preparation*). Lastly, preparation of hyperbranched polyacrylate samples and utilization of machine learning approaches for high throughput sample screening was conducted (*patent in preparation*).
- Managed laboratory safety by training workers on the potential hazards of chemicals and equipment

Tesla Palo Alto, CA
Polymers Engineering Intern May 2018 – August 2018

- Analyzed and validated mechanical performance of new adhesive formulations for battery pack materials; prepared research deliverables in a cross-functional team covering key changes in performance with formulation change.
- Conducted material screening, qualification, and analysis of biobased polymers and low carbon footprint alternative materials to reduce vehicle CO_2 equivalent carbon footprint. Internal review provided to materials manager.
- Conducted materials quality control review and screening of polymer material wear and fouling resistance for vehicle cabin materials.

University of Michigan, Ann Arbor – Love Group Ann Arbor, MI
Undergraduate Student Researcher 2017 – 2019

- Analyzed mechanical performance and stress relaxation of various athletic tapes available for treatment of muscle strain and rehabilitation
- Research findings and a poster were presented at the Biomedical Engineering Society (BMES) Annual Meeting (2018)

PUBLICATIONS & PRESENTATIONS

1. **Shannon, D.,** Cerdan-Gomez, K., Kim, M., Kuklinski, O., Valentine, M., Hawker, C., Bioinspired Metal-Ligand Networks: Facile Preparation of Hydroxypyridinone (HOPO) Functionalized Materials with Tunable and Patternable Properties, *In preparation.*
2. Webber, T.*, **Shannon, D.*,** Nordness, O., Hawker, C., Segalman, R., Han, S., Solution-like Water Transport Across Molecular to Macroscopic Length Scales in Crosslinked Poly(Ethylene Glycol Diacrylate) Networks with Tailored Sidechains, *In preparation* (*equal contribution)
3. **Shannon, D.**, Moon, J., Barney, C., *Materials Research Society (MRS), Spring Meeting*, San Francisco, CA – 2023
4. **Shannon, D.**, Moon, J., Barney, C., Sinha, N., Yang, K., Jones, S., Garcia, R., Helgeson, M., Segalman, R., Valentine, M., Hawker, C., Modular Synthesis and Patterning of High-Stiffness Networks by Postpolymerization Functionalization with Iron–Catechol Complexes, *Macromolecules* 2023, 56, 2268-2276.
5. **Shannon, D.**, Love, B., *Biomedical Engineering Society (BMES), Annual Meeting*, Atlanta, GA – 2018

LEADERSHIP EXPERIENCE

Materials Student Association: Prof. Development Committee Lead 2022-2024

- Committed to and expanded student engagement with the broader professional community by leading the organization of seminars, workshops, and networking events for students and industry professionals

- Organized a monthly, invited industry speaker series and end of year panel to highlight key skills needed to transition into industry. Hosted industry presenters from 13 companies across divisions of semiconducting, optical, structural, biological, and polymer materials.

Global Scholars Program: Student Advisory Council Member 2018-2019

- Worked as a member of the student advisory board to organize events for Global Scholars Program members while educating on and implementing sustainable and zero-waste practices

Global Scholars Program: Discussion Group Facilitator 2017-2018

- Lead a collaborative group of first year students in the Global Scholars Program while developing project management skills to help them complete their Global Engagement Internship.

VOLUNTEERING & OUTREACH

- Materials Student Association: Prof. Development Committee – May 2022 to January 2024
- Materials Research Laboratory Elementary School Outreach – 2019 to 2024 (various)
- Materials Student Association: First Year Mentorship Program – Fall 2020 and Fall 2021

ABSTRACT

Engineering Tailor-Made Polymers and Networks *via* Active Ester and Flow Chemistry

by

Declan Patrick Shannon

Natural network polymers are ubiquitous, leveraged for a diverse range of functions, and controlled by modular chemical motifs at the molecular level. Synthetically, there is a desire to borrow many of nature's methods to build network materials with modular approaches for screening and engineering materials properties. Yet in spite of the range of chemical transformations available, most network development follows the classic approach of network formulation, formation, and examination. This conventional methodology often entails challenges in precise control of network structures, as well as limitations in functional group compatibility with network polymerization approaches. Consequentially, there is a need for modular, scalable synthetic strategies which can be performed as post polymerization modifications of network pendant motifs for facile derivatization and screening of materials properties. To address this, we can turn to active ester chemistry as a versatile, scalable platform for control and manipulation of network functionalities using mild conditions and simple wash protocols. Through integration of active ester containing monomer units into widely used free radical network polymerizations, this thesis demonstrates the utility of this straightforward approach for materials screening and design. Key discussions highlight the ability to install biomimetic metal-ligand crosslinking motifs; modulate an array of properties including mechanical, magnetic, and fluorescent behavior; and lastly leverage simple derivatization strategies to interrogate the impact of chemical substituents on nanoscale water transport behavior.

To begin we can take direct structural inspiration from well characterized iron-catechol crosslinks of marine mussels and adapt these natural motifs to synthetic networks for tuning and patterning mechanical properties. Through utilization of a pentafluorophenyl acrylate as an active ester monomer unit, we can directly install catechol containing dopamine into the network, crucially without the need for protection or deprotection of phenolic moieties and avoiding their oxidation during substitution. Through this synthetic approach, large scale films could be prepared with an array of catechol and covalent crosslinking contents, followed by complexation and crosslinking of catechol groups with Fe^{3+} salts to achieve increases in elastic moduli of nearly two orders of magnitude. Moreover, by conceptually mirroring the mussels' core-shell iron localization in the byssal thread, we can design diffusion controlled gradients in ion incorporation in catechol functionalized networks to prepare materials with patterned ion installation and heterogeneous, composite-like mechanical properties. Results demonstrated sub-millimeter scale resolution control and appreciable changes in mechanical behavior.

Building from these approaches, we can turn to other biological inspirations for preparation of oxidation resistant materials which provide even greater degrees of tunability through increased metal chelation scope. While literature examples abound of potential ligands of interest, hydroxypyridinone (HOPO) motifs, adapted from the L-mimosine amino acid used in plants, present an enticing moiety to work with. Structurally, these ligands are similar to that of catechol moieties, but they have added benefits of increased oxidative stability and wider metal ion chelation scope through their altered ring structure. Present work builds on recent literature methods to prepare an active ester compatible, amine terminated HOPO ligand in a one pot approach, without the need for multiple protection and deprotection

steps. Leveraging the active ester network platform, ligands could be installed and complexed with an array of metal salts, allowing for comparison mechanical reinforcement differences between catechol and HOPO functionalized materials after complexation. By building on prior patterning methods and utilizing the improved properties of the HOPO motif, materials with heterogeneous mechanical, magnetic, and fluorescent responses could be prepared, opening new doors for material preparation for soft robotic and encryption applications.

Lastly, this topology consistent approach for network substituent modification was leveraged in hydrogel systems for measuring the impact of chemical identity on nanoscale water transport behavior. To conduct such measurements, Overhauser Dynamic Nuclear Polarization (ODNP) was leveraged as a combined electron paramagnetic and nuclear magnetic resonance (EPR and NMR) technique to measure interactions between passing water molecules and a nitroxide radical spin probe tethered to the network. Critically, ODNP measurements place significant restriction on sample geometry and must be conducted in narrow bore (0.6mm ID) capillaries. To address this challenge, prior work on active ester network polymerizations was extended to a biphasic flow synthesis, enabling the formation of microparticle networks with varied crosslinker and active ester content to modulate final water content and network substituents. Moreover, *via* this approach, large batches of parent materials could be prepared, split, and derivatized with both nitroxide spin labels and hydrophobic or hydrophilic sidechains, allowing for measurement of final hydrogel materials with consistent network topology and repeat unit sequence. Present results provide fundamental insight into nanoscale water behavior at the polymer network surface and highlight the impact of chemical identity on nanoscale water diffusivity, providing guiding design rules for next generation membrane materials.

TABLE OF CONTENTS

Chapter 1. Introduction 1

1.1 Polymer Networks: Diverse Structure Function Relationships 1

1.1.1 Motivation 1

1.1.2 Network Formation and Utility of Biomimetic Crosslinkers 2

1.1.3 Active Ester Chemistry for Polymeric Materials and Networks 6

1.1.4 Polymer Synthesis and Network Formation in Flow 10

1.2 References 15

Chapter 2. Modular Synthesis and Patterning of High Stiffness Networks by Post Polymerization Functionalization with Iron-Catechol Complexes 25

2.1 Abstract 25

2.2 Introduction 26

2.3 Results and Discussion 28

2.4 Conclusion 45

2.5 References 46

Chapter 3. Bioinspired Metal-Ligand Networks: Facile Preparation of Hydroxypyridinone (HOPO) Functionalized Materials with Tunable and Patternable Properties 53

3.1 Abstract 53

3.2 Introduction 53

3.3 Results and Discussion 56

3.4 Conclusions & Future Work 71

3.5 References 73

Chapter 4. Solution-like Water Transport Across Molecular to Macroscopic Length Scales in Crosslinked Poly(ethylene glycol diacrylate) Networks with Tailored Sidechains 80

4.1 Abstract 80

4.2 Introduction 81

4.3 Results and Discussion 85

4.4 Methods 101

4.5 Conclusions and Future Work 108

4.6 References 110

Chapter 5. Conclusions 117
Appendix A. Supporting Information for Chapter 2 121
Appendix B. Supporting Information for Chapter 3 143
Appendix C. Supporting Information for Chapter 4 163

Chapter 1. Introduction

1.1 Polymer Networks: Diverse Structure Function Relationships

1.1.1 Motivation

Polymeric and soft materials are widely leveraged in natural and synthetic systems with varied macromolecular architectures including examples from simple linear chains to combs, brushes, hyperbranched systems, and crosslinked network materials[1–4]. Among these, polymer network materials represent a critical class of polymer architectures for their utilization of crosslinking motifs between chains, providing structure and stability in both dry and solvated systems ranging from rubbers to hydrogels. While simple in concept, crosslinking of polymer structures results in a range of materials properties and emergent, challenging to predict phenomena arising from the chemistry of the crosslinking site and statistical nature of network architecture[2,4,5]. In response to challenges in predicting network behavior from chemistry and crosslinking functionality, literature has developed an array of models of network behavior, including affine[6], phantom[7], and now real elastic network theory[5,8,9]. However, model development is ongoing, and in-situ characterization of both networks and defects remains an active area of materials research, with challenges multiplexed by the nature and dynamics of the crosslinker chemistry[5].

In developing our understanding of polymer network structure and contextualizing its impact, we can build from the molecular level of the crosslinker up. Moreover, we can look to both natural network systems[1,3,10–12] and the history of synthetic crosslinked materials from Staudinger onwards[13]. However, this incredibly broad swath of materials research still offers many opportunities for fundamental insight and design due to challenges of predicting

structure property relationships from molecular structure and tuning materials properties as a function of substituents and crosslinker chemistry [2,4,5,14].

1.1.2 Network Formation and Utility of Biomimetic Crosslinkers

In understanding the synthesis and formation of network polymers, it is essential to grasp the significance of the crosslinker and its pivotal role in determining network properties. Crosslinking units within network polymers can range from simple static, covalently bonded linkages between chains to more complex dynamic or transient motifs designed to modulate network behavior. Natural systems offer valuable inspiration for chemists and engineers, and often circumvent classical synthetic property tradeoffs through cleverly architected crosslinking strategies[1,3,11,15][could expand ref]. Building on biological approaches, biomimetic and bioinspired synthetic systems have had success through modulation of crosslinker chemistry and incorporation of a range of structures including transient crosslinking species such as dynamic covalent bonding motifs, hydrogen bonding crosslinkers, and metal-ligand bonds[2,3,16–25].

Among these approaches, biomimetic metal ligand bonds represent a crucial area of synthetic materials development as they provide a facile, modular method for both network crosslinking and tuning of crosslink strength through selection of the metal-ligand pair[17,18,26][expand ref]. Various well characterized natural systems provide excellent approaches, including marine mussels[11], invertebrate jaws[15,27,28], and others[29,30][expand ref], which leverage metal-ligand crosslinking motifs for various functions, such as mechanical reinforcement and stress dissipation. Utilization of this strategy can be contextualized in light of fundamental, well documented chemical interactions at the metal-ligand crosslinking site,

namely the association constants, dynamics, and stability of the metal ligand pair[17,31–33]. Such interactions can be tuned as a function of individual metal ion species, or through mixed metal ion systems to control materials properties[17,34]. Moreover, metal-ligand crosslinking chemistry provides a facile route to change the crosslink functionality, or number of potentially crosslinked chains[17] [expand ref], through modulation of the ligand coordination geometry. Such changes can be done either statically through selection of metal ion[34–36], or in more responsive contexts as a function of environmental variables such as pH[17,37]. These inherent aspects of metal-ligand crosslinking motifs provide them with unparalleled ease of tunability relative to other crosslinking strategies.

Expanding from the scale of an individual crosslink, be it static or dynamic, one must then consider the impact of network formation and structure. While various methods of network synthesis and crosslinker chemistry can be leveraged, the present discussion will focus around the case of free radically polymerized networks, and various considerations of crosslinking in this approach are extensible to other network systems[4,5,25]. It is worth noting however, that such free radical systems deviate in both properties and topology from more well controlled networks with ideal end linking of crosslinkers or preformed star polymers[5,25,38]. Free radically polymerized networks play a key role in succeeding chapters, and this method of network formation still represents an incredibly diverse group of materials. In a classic free radical network polymerization, analogous to its linear analogues, materials are prepared through initiation from a reactive radical species and propagation of the growing chain end through reactive motifs of monomer units, such as the double bonds in vinyl, (meth)acrylic, and related monomers. However, unlike linear analogues, multifunctional monomer units are leveraged to intentionally form crosslinking sites needed to generate the

network[4]. As demonstrated in **Figure 1.1**, the radical chain end can react with vinyl motifs from both free monomers, as well as pendant, unreacted motifs of the same chain or other macromolecules, forming intra or intermolecular crosslinks[4,5], with comparable propagation events occurring for related (meth)acrylic or (meth)acrylamide systems. Tuning the relative distributions and types of crosslinking motifs can allow for reduction in network loop defects and drastically alter system topology, and in some cases, keep the system below the gelation threshold, forming hyperbranched, soluble materials[4,5,39–41]. However, for classical free radical systems, topological control is limited and depends heavily on the structure and functionality of crosslinking monomers as well as other pre-polymerization conditions (e.g. solvent, concentration, etc.)[4,25,42–44]. Consequentially, it can be challenging to determine the impact of subtle variations in network topology and sequence during pendant group screening, making direct comparisons of functionality challenging. Moreover, resultant materials can present with heterogenous microstructures and fluctuations in crosslinking density leading to statistical, emergent properties which can be challenging to predict from a molecular understanding, which deviates from ideal, end linked networks[4,5,25,38,42,45].

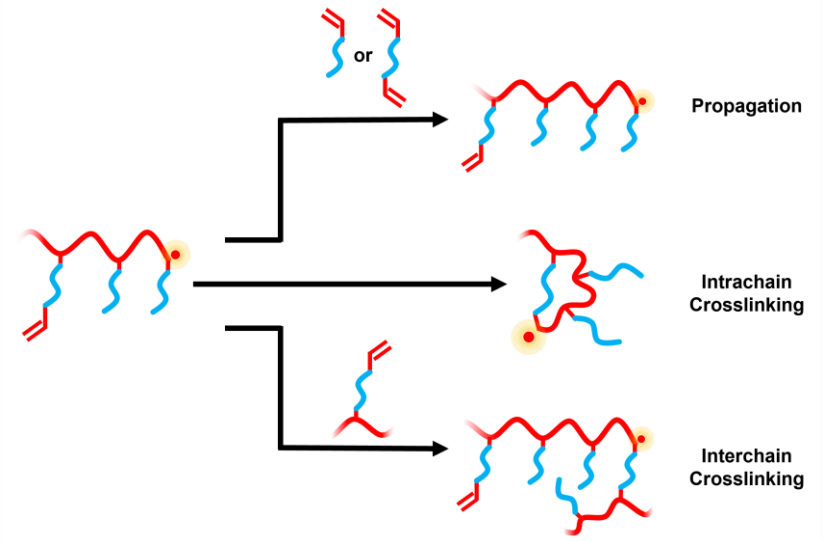
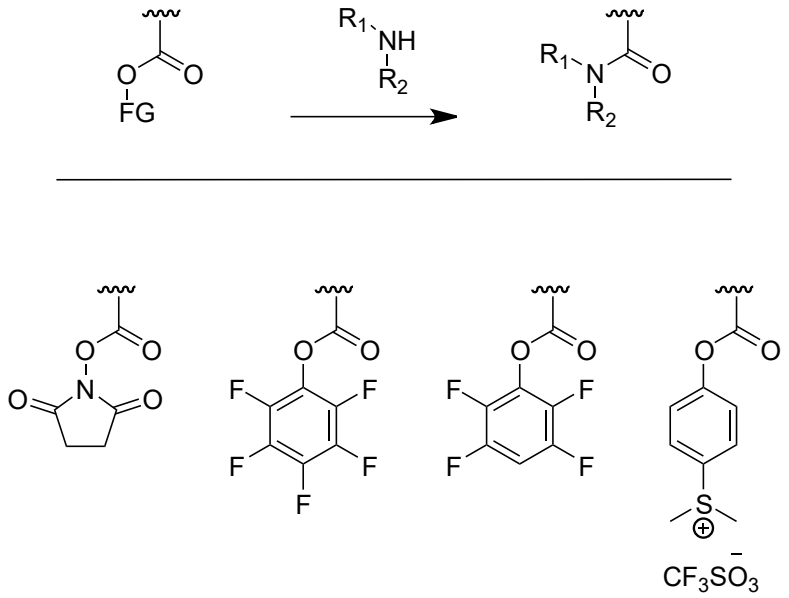


Figure 1.1: Potential propagation events in free radical network polymerization. From top to bottom: (top) propagation with unincorporated monomers; (middle) intramolecular crosslinking with pendant motifs; (bottom) interchain crosslinking with pendant motifs from other macromolecular chains.

Despite the topological limits, free radical network polymerization has seen wide adoption for network formation, and provided an efficient, effective method for forming a diverse array of materials. It has been applicable at varied scopes from the chemical and network architectural level, to larger scale applications in 3D printing and beyond[22,46–52][expand ref]. The compatibility of this strategy with conventional vinyl, (meth)acrylic, and acrylamide monomer chemistries has lowered the barrier to entry for preparing bespoke monomer units and crosslinker chemistries which offer additional functionality and further modulate materials properties[36,53] [expand ref]. While challenges in network sequence and topology can still exist during library formulation, post functionalization strategies can be employed to conduct more direct comparison on substituent effects on the network without concerns of changing polymerization conditions[47].

1.1.3 Active Ester Chemistry for Polymeric Materials and Networks

The use of active ester chemistry has been leveraged to prepare modular products for a diverse range of applications due to its wide substrate scope, and it is an excellent method to bring modularity to macromolecular and network material design[47,54–56]. This chemistry offers facile installation at reactive ester sites which are easily amidated (**Scheme 1.1 – top** to afford a range of products. As such, macromolecules bearing these motifs can be easily derivatized, and crucially, post polymerization modification can be leveraged to compare the impact of sidechain chemistry in materials with identical polymer properties (e.g. M_n, M_w, $Đ$, or network topology)[47,54,57–60]. These approaches have found success in comparative screening of macromolecular materials properties. While other approaches are available and widely effective, such as thiol-ene click[61], copper(I) catalyzed azide-alkyne click[62], or strain promoted azide-alkyne click[63,64], active ester chemistry finds its niche in being a radical and metal-free technique to install a diverse array of amine functionalities, harnessing both biologic amine terminated reagents, as well as cheap and widely available synthetic amine building blocks.



Scheme 1.1: (Top) Substitution of active ester motif represented by FG. (Bottom) Example groups used in active ester chemistry. Left to right: NHS ester, pentafluorophenyl ester, tetrafluorophenyl ester, phenyldimethylsulfonium triflate ester.

An array of activated ester chemistries has been developed to tune reactivity of the pendant active ester moiety as well as impart added functionality. Common examples (**Scheme 1.1 – bottom**) include moieties such as N-hydroxysuccinimide[65] (NHS) and fluorinated phenyl esters (pentafluoro and tetrafluorophenyl esters)[54,66,67]. However, more advanced species exist which provide systems with selective deactivation of active ester motifs[68]. Regardless of pendant moiety of choice, it is crucial to the success of this strategy to identify both a functional motif which can be readily attached to monomer or initiating groups, as well as survive polymerization and work up conditions, as some motifs are prone to hydrolysis[54]. Many active ester derivatives have been extensively used as (meth)acrylate monomers in radical polymerizations[54,57,69], and further examples are seen in modification of small molecule chain end moieties, including RAFT agents and ATRP initiators[54,70,71]. Such

incorporation strategies have proven effective in both systems leveraging single activated ester motifs, as well as copolymers of active ester structures with different reactivities[55,59], allowing for preferential installation of different pendant groups at respective active ester moieties.

While this approach is of great utility for screenings of soluble macromolecular architectures, the utility of the active ester chemistry in network systems is comparable, if not more useful, as it preserves network topology and monomer sequencing upon derivatization. Network materials, as discussed in Section 1.1.1, present a challenging optimization problem as many material properties function as emergent phenomena deriving from network substituent chemical properties and statistical, architectural motifs of the network[4,5]. While various preparation strategies are available for forming network materials, alteration of initial network polymerization conditions, monomer species, and solvent-monomer interactions can significantly impact the incorporation, sequence, and structure of the network polymer[4,42,44,45]. Consequentially preparation of libraries with varied network functionalities will likely result in systems with both intentionally varied chemical motifs, and unintentionally altered network topology; and disentangling the impact of these potentially subtle changes on materials properties can become incredibly difficult. Even simple, single component poly(ethylene glycol diacrylate) networks formed in free radical polymerization have shown mild changes in solvent ratios can lead to heterogeneous networks with porous microstructures[42]. As a result, being able to post-modify the network structure is of great utility for studying fundamental materials properties in polymer networks and can be achieved *via* active ester chemistry.

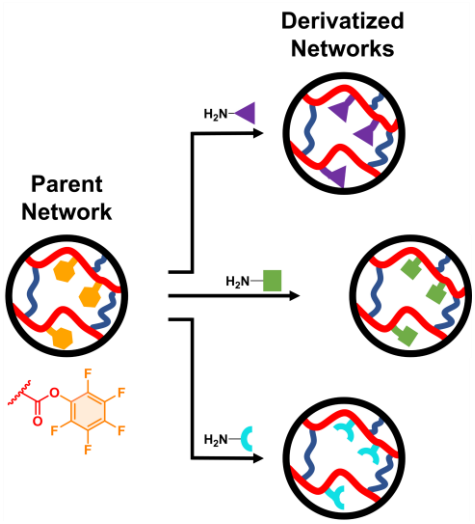


Figure 1.2. Conceptual demonstration of pentafluorophenyl ester substitution in a network polymer with varied primary amines creating an array of derivatized networks which maintain the same network topology.

In addition to maintaining network topology during derivatization, post polymerization modification opens doors to preparation of a wide array of materials systems which would be challenging by other means. Notable advantages of active ester substitution have been demonstrated for the preparation of systems with challenging or reactive monomers, as well as heterogeneous, immiscible components. Present discourse focuses around relevant examples of this approach and readers are encouraged to consult comprehensive reviews for this synthetic method[54]. As detailed in literature[43,47] and Chapter 2, active ester chemistry has demonstrated the capability to directly install challenging motifs, such as easily oxidized catechol moieties. This is in contrast to prior incorporation strategies of dopamine-mimetic motifs which require various protection and deprotection strategies to avoid oxidation[16,72,73]. Similarly, post polymerization modification has been leveraged in the literature to prepare a range of tunable networks containing highly hydrophobic PDMS acrylate and hydrophilic acrylamide motifs[58,74]. Such approaches highlight the versatility and

effectiveness of this strategy, as their library preparation strategy maintains system topology despite the highly immiscible monomer components, which would prove challenging by other synthetic methods. In summary, post polymerization modification of network materials, particularly through the use of active esters, offers many advantages for facile preparation and derivatization of macromolecular systems. By bypassing concerns of pre-polymerization condition changes impacting topology or network structure, such approaches enable greater creativity in network design, facilitating the incorporation of challenging pendant groups with differing properties than the parent material.

1.1.4 Polymer Synthesis and Network Formation in Flow

Present discourse has largely focused around examples of network materials leveraged on the bulk, macroscopic scale, but comparable free radical network polymerizations have seen wide adoption for microparticle networks prepared through flow and microfluidic synthesis[75,76]. As a result, active ester chemistry for facile network substitution and derivatization can be utilized as an equally effective tool in tandem with flow synthesis for microparticle network systems. Flow synthesis for preparation of polymer materials presents an attractive area of research and development for its advantages over batch synthesis which stem from its unique reactor geometry[77,78]. Crucially, reactions in flow have greater tunability in their surface area to volume ratios without the concomitant limitations of batch reactions under similar constraints. This altered form factor allows for more uniform internal reaction conditions with improved heat or light flux into the reactor either *via* improved heat dissipation or reduced light attenuation[77,78]. Moreover, by controlling reactor geometry, one can leverage micro- and meso-scale reactors to access small length scale interfacial and

droplet based reactions for preparing a range of products, which can be challenging to scale at the macroscopic, batch level[79,80]. While the reader is referred to many excellent literature reviews for comprehensive discussions of synthesis in flow for both small molecules[77,78,81] and macromolecules[82,83], an overview of relevant flow synthesis techniques is included here.

Critical to an understanding of flow synthesis is an appreciation of changes in reaction conditions upon transition from batch to flow. While the impact of changing surface area to volume ratio has already been touched on above, there are also notable impacts on the reaction fluid behavior resulting from the reduced length scale and moving fluid stream. To characterize the state the fluid flow operates in, various properties of fluid can be modeled in terms of their dimensionless numbers, such as Reynolds number (Re), Capillary number (Ca), Weber number (We, multiphase flows), etc., and an in depth discussion of these factors is conducted in the literature[77,84]. Moreover, at the relevant length scales for microfluidic systems, there is increased impact of fluid properties, e.g. viscosity, wetting, and interfacial tension, on fluid behavior and droplet generation[75,84–86]. While the increased impact of fluidic properties may seem challenging, an understanding of these parameters can be harnessed to generate a range of conditions in-situ and control various types of fluid flows. Liebfarth[87–89], Guirronet[90–93], Di Carlo[94], and others[95,96][add refs] have demonstrated the impacts and utility of various microfluidic flows on polymer product formation, and similar approaches are used herein (Chapter 4) for biphasic plug flow synthesis. While other more complex microfluidic droplet generation and mixing approaches are areas of ongoing research, they are beyond the scope of this introduction and the reader is referred to more recent literature[75,77,97].

Biphasic plug flow provides a facile method to access a range of desirable flow reactor behaviors, namely controlled residence time, droplet generation, and interfacial reactions. In

a conventional biphasic plug flow system, two immiscible phases are used, a carrier phase which wets the surface of tubing, and a droplet phase which segments the continuous carrier (**Figure 1.3**)[77,82,84,86,98]. Many systems are employed which use biphasic gas-liquid systems where the dispersed phase is an inert gas bubble, and the reaction occurs in the carrier solution media. Similarly, liquid-liquid plug flows can be leveraged for higher viscosity biphasic flows[99,100], which avoid challenges of gas bubble compression. In liquid-liquid systems, reactions can be conducted in either immiscible phase or at the droplet interface, leveraging the high interfacial area. Example media include aqueous-organic, immiscible organic phases, and frequently fluorous-organic systems using highly fluorinated oils as the carrier[85,86,90,95,101]. These approaches can be merged to create increasingly complex multiphase flows utilizing three or more phases[101,102]. Regardless of selected medium, biphasic flow can be tuned to control the relative volume and distribution of droplet and carrier phases through modulation of flow rate, volumetric flow ratios, and critical dimension of reactor tubing in both gas-liquid and liquid-liquid flows[103–107].

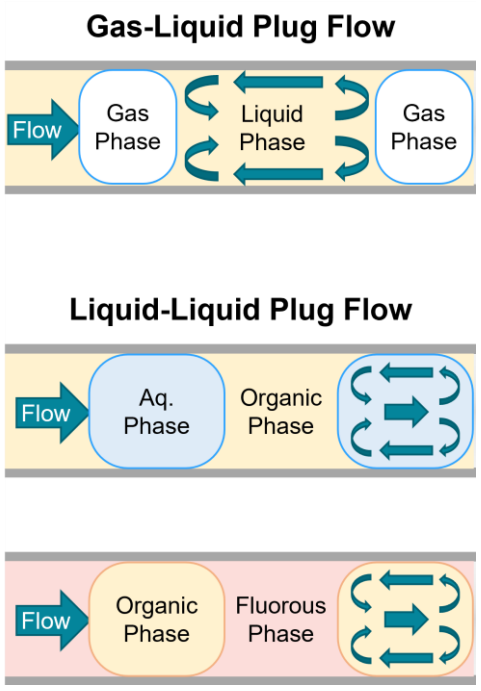


Figure 1.3: Example diagrams of gas-liquid and liquid-liquid biphasic plug flow.

Liquid-liquid plug flow provides a facile method for droplet generation and microparticle formation via in-situ network polymerization and is amenable to a range of fluidic conditions[75]. In particular, fluorous-organic plug flow offers unique advantages through the use of highly fluorinated oils, which are frequently immiscible with common radical polymerization monomers (e.g. methacrylates, acrylates, and acrylamides) and will preferentially wet many (fluoro)polymer tubing walls[77,85,101,108]. Such properties allow for effective organic droplet encapsulation and reduce challenges associated with particle sticking and reactor clogging[85,109]. Moreover, free radical network polymerizations can be carried out in dispersed droplet phases, forming the network in-situ, with controlled geometry. The synthetic ease and versatility of this approach make such droplet formation strategies amenable to a range of initiation conditions dependent on the system chemistry of interest.

Such flow synthesis approaches represent a powerful tool to extend well studied network chemistries to microparticle materials with controlled size and morphology for novel applications[75,76,108]. Through utilization of these synthetic strategies, in tandem with post polymerization modification of active ester networks, we can combine these approaches to design microparticle network systems which can be easily substituted from a single batch of active ester materials, as demonstrated in Chapter 4.

1.2 References

(1) Fratzl, P.; Weinkamer, R. Nature's Hierarchical Materials. *Prog. Mater. Sci.* **2007**, *52* (8), 1263–1334. https://doi.org/10.1016/j.pmatsci.2007.06.001.

(2) Zhao, X.; Chen, X.; Yuk, H.; Lin, S.; Liu, X.; Parada, G. Soft Materials by Design: Unconventional Polymer Networks Give Extreme Properties. *Chem. Rev.* **2021**, *121* (8), 4309–4372. https://doi.org/10.1021/acs.chemrev.0c01088.

(3) Ganewatta, M. S.; Wang, Z.; Tang, C. Chemical Syntheses of Bioinspired and Biomimetic Polymers toward Biobased Materials. *Nat. Rev. Chem. 2021 511* **2021**, *5* (11), 753–772. https://doi.org/10.1038/s41570-021-00325-x.

(4) Gao, Y.; Zhou, D.; Lyu, J.; A, S.; Xu, Q.; Newland, B.; Matyjaszewski, K.; Tai, H.; Wang, W. Complex Polymer Architectures through Free-Radical Polymerization of Multivinyl Monomers. *Nat. Rev. Chem.* **2020**, *4* (4), 194–212. https://doi.org/10.1038/s41570-020-0170-7.

(5) Danielsen, S. P. O.; Beech, H. K.; Wang, S.; El-Zaatari, B. M.; Wang, X.; Sapir, L.; Ouchi, T.; Wang, Z.; Johnson, P. N.; Hu, Y.; Lundberg, D. J.; Stoychev, G.; Craig, S. L.; Johnson, J. A.; Kalow, J. A.; Olsen, B. D.; Rubinstein, M. Molecular Characterization of Polymer Networks. *Chem. Rev.* **2021**, *121* (8), 5042–5092. https://doi.org/10.1021/acs.chemrev.0c01304.

(6) Flory, P. J. *Principles of Polymer Chemistry*; Cornell University Press, 1953.

(7) Treloar, L. R. G. *The Physics of Rubber Elasticity: By L.R.G. Treloar*, 3rd ed.; Oxford classic texts in the physical sciences; Oxford University Press: New York: Oxford : New York, 1975.

(8) Zhong, M.; Wang, R.; Kawamoto, K.; Olsen, B. D.; Johnson, J. A. Quantifying the Impact of Molecular Defects on Polymer Network Elasticity. *Science* **2016**, *353* (6305), 1264–1268. https://doi.org/10.1126/SCIENCE.AAG0184/SUPPL_FILE/ZHONG.SM.PDF.

(9) Rubinstein, M.; Colby, R. H. *Polymer Physics*; Oxford University Press, 2003. https://doi.org/10.1093/oso/9780198520597.001.0001.

(10) Qin, G.; Hu, X.; Cebe, P.; Kaplan, D. L. Mechanism of Resilin Elasticity. *Nat. Commun.* **2012**, *3* (1), 1003. https://doi.org/10.1038/ncomms2004.

(11) Harrington, M. J.; Masic, A.; Holten-Andersen, N.; Waite, J. H.; Fratzl, P. Iron-Clad Fibers: A Metal-Based Biological Strategy for Hard Flexible Coatings. *Science* **2010**, *328* (5975), 216–220. https://doi.org/10.1126/science.1181044.

(12) Thurmond, F.; Trotter, J. Morphology and Biomechanics of the Microfibrillar Network of Sea Cucumber Dermis. *J. Exp. Biol.* **1996**, *199* (8), 1817–1828. https://doi.org/10.1242/jeb.199.8.1817.

(13) Staudinger, H.; Husemann, E. Über Hochpolymere Verbindungen, 116. Mitteil.: Über Das Begrenzt Quellbare Poly-Styrol. *Berichte Dtsch. Chem. Ges. B Ser.* **1935**, *68* (8), 1618–1634. https://doi.org/10.1002/cber.19350680841.

(14) Lin, X.; Wang, X.; Zeng, L.; Wu, Z. L.; Guo, H.; Hourdet, D. Stimuli-Responsive Toughening of Hydrogels. *Chem. Mater.* **2021**, *33* (19), 7633–7656. https://doi.org/10.1021/ACS.CHEMMATER.1C01019.

(15) Joester, D.; Brooker, L. R. The Chiton Radula: A Model System for Versatile Use of Iron Oxides. In *Iron Oxides*; John Wiley & Sons, Ltd, 2016; pp 177–206. https://doi.org/10.1002/9783527691395.ch8.

(16) Filippidi, E.; Cristiani, T. R.; Eisenbach, C. D.; Waite, J. H.; Israelachvili, J. N.; Ahn, B. K.; Valentine, M. T. Toughening Elastomers Using Mussel-Inspired Iron-Catechol Complexes. *Science* **2017**, *358* (6362), 502–505. https://doi.org/10.1126/science.aao0350.

(17) Khare, E.; Holten-Andersen, N.; Buehler, M. J. Transition-Metal Coordinate Bonds for Bioinspired Macromolecules with Tunable Mechanical Properties. *Nat. Rev. Mater.* **2021**, *0123456789*. https://doi.org/10.1038/s41578-020-00270-z.

(18) Shi, L.; Ding, P.; Wang, Y.; Zhang, Y.; Ossipov, D.; Hilborn, J. Self-Healing Polymeric Hydrogel Formed by Metal–Ligand Coordination Assembly: Design, Fabrication, and Biomedical Applications. *Macromol. Rapid Commun.* **2019**, *40* (7), 1800837. https://doi.org/10.1002/marc.201800837.

(19) Oku, T.; Furusho, Y.; Takata, T. A Concept for Recyclable Cross-Linked Polymers: Topologically Networked Polyrotaxane Capable of Undergoing Reversible Assembly and Disassembly. *Angew. Chem. Int. Ed.* **2004**, *43* (8), 966–969. https://doi.org/10.1002/ANIE.200353046.

(20) Liu, J.; Tan, C. S. Y.; Yu, Z.; Li, N.; Abell, C.; Scherman, O. A. Tough Supramolecular Polymer Networks with Extreme Stretchability and Fast Room-Temperature Self-Healing. *Adv. Mater.* **2017**, *29* (22), 1605325. https://doi.org/10.1002/adma.201605325.

(21) Wu, J.; Cai, L.-H.; Weitz, D. A.; Wu, J.; Cai, L.-H.; Weitz, D. A. Tough Self-Healing Elastomers by Molecular Enforced Integration of Covalent and Reversible Networks. *Adv. Mater.* **2017**, *29* (38), 1702616–1702616. https://doi.org/10.1002/ADMA.201702616.

(22) Choi, C.; Self, J. L.; Okayama, Y.; Levi, A. E.; Gerst, M.; Speros, J. C.; Hawker, C. J.; Read De Alaniz, J.; Bates, C. M. Light-Mediated Synthesis and Reprocessing of Dynamic Bottlebrush Elastomers under Ambient Conditions. *J. Am. Chem. Soc.* **2021**, *143* (26), 9866–9871. https://doi.org/10.1021/jacs.1c03686.

(23) Zhang, Q.; Qu, D.-H.; Feringa, B. L.; Tian, H. Disulfide-Mediated Reversible Polymerization toward Intrinsically Dynamic Smart Materials. *J. Am. Chem. Soc.* **2022**, *144* (5), 2022–2033. https://doi.org/10.1021/jacs.1c10359.

(24) Wang, S.; Urban, M. W. Self-Healing Polymers. *Nat. Rev. Mater.* **2020**, *5* (8), 562–583. https://doi.org/10.1038/s41578-020-0202-4.

(25) Clarke, B. R.; Tew, G. N. Programming Mechanical Properties through Encoded Network Topologies. *J. Polym. Sci.* **2024**, pol.20230594. https://doi.org/10.1002/pol.20230594.

(26) Zhang, J.; Su, C. Y. Metal-Organic Gels: From Discrete Metallogelators to Coordination Polymers. *Coord. Chem. Rev.* **2013**, *257* (7–8), 1373–1408. https://doi.org/10.1016/J.CCR.2013.01.005.

(27) Lichtenegger, H. C.; Schöberl, T.; Ruokolainen, J. T.; Cross, J. O.; Heald, S. M.; Birkedal, H.; Waite, J. H.; Stucky, G. D. Zinc and Mechanical Prowess in the Jaws of Nereis, a Marine Worm. *Proc. Natl. Acad. Sci.* **2003**, *100* (16), 9144–9149. https://doi.org/10.1073/pnas.1632658100.

(28) Politi, Y.; Priewasser, M.; Pippel, E.; Zaslansky, P.; Hartmann, J.; Siegel, S.; Li, C.; Barth, F. G.; Fratzl, P. A Spider's Fang: How to Design an Injection Needle Using Chitin-Based Composite Material. *Adv. Funct. Mater.* **2012**, *22* (12), 2519–2528. https://doi.org/10.1002/adfm.201200063.

(29) Lee, S.; Kustin, K.; Robinson, W. E.; Frankel, R. B.; Spartalian, K. Magnetic Properties of Tunicate Blood Cells: I. Ascidia Nigra. *J. Inorg. Biochem.* **1988**, *33* (3), 183–192. https://doi.org/10.1016/0162-0134(88)80048-5.

(30) Simpson, C. L.; Pierpont, C. G. Complexes of Vanadium(III) and Vanadium(IV) Containing Bipyridine and Tetrachlorocatecholate Ligands. Insights into the Tunicate Vanadium(III) Coordination Environment. *Inorg. Chem.* **1992**, *31* (21), 4308–4313. https://doi.org/10.1021/ic00047a018.

(31) Martell, A. E.; Hancock, R. D. Stability Constants and Their Measurement. In *Metal Complexes in Aqueous Solutions*; Springer US: Boston, MA, 1996; pp 217–244. https://doi.org/10.1007/978-1-4899-1486-6_7.

(32) Martell, A. E.; Smith, R. M. *Critical Stability Constants: First Supplement*; Springer US: Boston, MA, 1982. https://doi.org/10.1007/978-1-4615-6761-5.

(33) Murphy, J. M.; Powell, B. A.; Brumaghim, J. L. Stability Constants of Bio-Relevant, Redox-Active Metals with Amino Acids: The Challenges of Weakly Binding Ligands. *Coord. Chem. Rev.* **2020**, *412*, 213253. https://doi.org/10.1016/j.ccr.2020.213253.

(34) Grindy, S. C.; Lenz, M.; Holten-Andersen, N. Engineering Elasticity and Relaxation Time in Metal-Coordinate Cross-Linked Hydrogels. *Macromolecules* **2016**, *49* (21), 8306–8312. https://doi.org/10.1021/acs.macromol.6b01523.

(35) Grindy, S. C.; Learsch, R.; Mozhdehi, D.; Cheng, J.; Barrett, D. G.; Guan, Z.; Messersmith, P. B.; Holten-Andersen, N. Control of Hierarchical Polymer Mechanics with

Bioinspired Metal-Coordination Dynamics. *Nat. Mater.* **2015**, *14* (12), 1210–1216. https://doi.org/10.1038/nmat4401.

(36) Meurer, J.; Bätz, T.; Hniopek, J.; Zechel, S.; Schmitt, M.; Popp, J.; Hager, M. D.; Schubert, U. S. Dual Crosslinked Metallopolymers Using Orthogonal Metal Complexes as Rewritable Shape-Memory Polymers. *J. Mater. Chem. A* **2021**, *9* (26), 15051–15058. https://doi.org/10.1039/D1TA03064G.

(37) Holten-Andersen, N.; Harrington, M. J.; Birkedal, H.; Lee, B. P.; Messersmith, P. B.; Lee, K. Y. C.; Waite, J. H. pH-Induced Metal-Ligand Cross-Links Inspired by Mussel Yield Self-Healing Polymer Networks with near-Covalent Elastic Moduli. *Proc. Natl. Acad. Sci. U. S. A.* **2011**, *108* (7), 2651–2655. https://doi.org/10.1073/pnas.1015862108.

(38) Kong, V. A.; Staunton, T. A.; Laaser, J. E. Effect of Cross-Link Homogeneity on the High-Strain Behavior of Elastic Polymer Networks. *Macromolecules* **2024**. https://doi.org/10.1021/acs.macromol.3c02565.

(39) Pan, T.; Dutta, S.; Kamble, Y.; Patel, B. B.; Wade, M. A.; Rogers, S. A.; Diao, Y.; Guironnet, D.; Sing, C. E. Materials Design of Highly Branched Bottlebrush Polymers at the Intersection of Modeling, Synthesis, Processing, and Characterization. *Chem. Mater.* **2022**, *34* (5), 1990–2024. https://doi.org/10.1021/acs.chemmater.1c04030.

(40) Bannister, I.; C. Billingham, N.; P. Armes, S. Monte Carlo Modelling of Living Branching Copolymerisation of Monovinyl and Divinyl Monomers: Comparison of Simulated and Experimental Data for ATRP Copolymerisation of Methacrylic Monomers. *Soft Matter* **2009**, *5* (18), 3495–3504. https://doi.org/10.1039/B901892A.

(41) O'Brien, N.; McKee, A.; Sherrington, D. C.; Slark, A. T.; Titterton, A. Facile, Versatile and Cost Effective Route to Branched Vinyl Polymers. *Polymer* **2000**, *41* (15), 6027–6031. https://doi.org/10.1016/S0032-3861(00)00016-1.

(42) De Molina, P. M.; Lad, S.; Helgeson, M. E. Heterogeneity and Its Influence on the Properties of Difunctional Poly(Ethylene Glycol) Hydrogels: Structure and Mechanics. *Macromolecules* **2015**, *48* (15), 5402–5411. https://doi.org/10.1021/acs.macromol.5b01115.

(43) Shannon, D. P.; Moon, J. D.; Barney, C. W.; Sinha, N. J.; Yang, K.-C.; Jones, S. D.; Garcia, R. V.; Helgeson, M. E.; Segalman, R. A.; Valentine, M. T.; Hawker, C. J. Modular Synthesis and Patterning of High-Stiffness Networks by Postpolymerization Functionalization with Iron–Catechol Complexes. *Macromolecules* **2023**, *56* (6), 2268–2276. https://doi.org/10.1021/acs.macromol.2c02561.

(44) Wu, B.; Chassé, W.; Peters, R.; Brooijmans, T.; Dias, A. A.; Heise, A.; Duxbury, C. J.; Kentgens, A. P. M.; Brougham, D. F.; Litvinov, V. M. Network Structure in Acrylate Systems: Effect of Junction Topology on Cross-Link Density and Macroscopic Gel Properties. *Macromolecules* **2016**, *49* (17), 6531–6540. https://doi.org/10.1021/acs.macromol.6b01070.

(45) Borges, F. T. P.; Papavasiliou, G.; Teymour, F. Characterizing the Molecular Architecture of Hydrogels and Crosslinked Polymer Networks beyond Flory–Rehner—I. Theory. *Biomacromolecules* **2020**, *21* (12), 5104–5118. https://doi.org/10.1021/acs.biomac.0c01256.

(46) Dolinski, N. D.; Page, Z. A.; Callaway, E. B.; Eisenreich, F.; Garcia, R. V.; Chavez, R.; Bothman, D. P.; Hecht, S.; Zok, F. W.; Hawker, C. J. Solution Mask Liquid Lithography (SMaLL) for One-Step, Multimaterial 3D Printing. *Adv. Mater.* **2018**, *30* (31), 1–6. https://doi.org/10.1002/adma.201800364.

(47) Moon, J. D.; Sujanani, R.; Geng, Z.; Freeman, B. D.; Segalman, R. A.; Hawker, C. J. Versatile Synthetic Platform for Polymer Membrane Libraries Using Functional Networks. *Macromolecules* **2021**, *54* (2), 866–873. https://doi.org/10.1021/acs.macromol.0c02414.

(48) Murphy, R. D.; Garcia, R. V.; Oh, S. J.; Wood, T. J.; Jo, K. D.; Read de Alaniz, J.; Perkins, E.; Hawker, C. J. Tailored Polypeptide Star Copolymers for 3D Printing of Bacterial Composites Via Direct Ink Writing. *Adv. Mater.* **2023**, *35* (3), 2207542. https://doi.org/10.1002/adma.202207542.

(49) Allen, M. J.; Sujanani, R.; Chamseddine, A.; Freeman, B. D.; Page, Z. A. Mechanically Robust Hydrophobized Double Network Hydrogels and Their Fundamental Salt Transport Properties. *J. Polym. Sci.* **2021**, *59* (21), 2581–2589. https://doi.org/10.1002/pol.20210260.

(50) Chen, Q.; Chen, H.; Zhu, L.; Zheng, J. Fundamentals of Double Network Hydrogels. *J. Mater. Chem. B* **2015**, *3* (18), 3654–3676. https://doi.org/10.1039/c5tb00123d.

(51) Hirsch, M.; Charlet, A.; Amstad, E. 3D Printing of Strong and Tough Double Network Granular Hydrogels. *Adv. Funct. Mater.* **2021**, *31* (5), 2005929. https://doi.org/10.1002/adfm.202005929.

(52) Lipkowitz, G.; Samuelsen, T.; Hsiao, K.; Lee, B.; Dulay, M. T.; Coates, I.; Lin, H.; Pan, W.; Toth, G.; Tate, L.; Shaqfeh, E. S. G.; DeSimone, J. M. Injection Continuous Liquid Interface Production of 3D Objects. *Sci. Adv.* **2022**, *8* (39), eabq3917. https://doi.org/10.1126/sciadv.abq3917.

(53) Wang, Z. J.; Jiang, J.; Mu, Q.; Maeda, S.; Nakajima, T.; Gong, J. P. Azo-Crosslinked Double-Network Hydrogels Enabling Highly Efficient Mechanoradical Generation. *J. Am. Chem. Soc.* **2022**, *144* (7), 3154–3161. https://doi.org/10.1021/jacs.1c12539.

(54) Das, A.; Theato, P. Activated Ester Containing Polymers: Opportunities and Challenges for the Design of Functional Macromolecules. *Chem. Rev.* **2016**, *116* (3), 1434–1495. https://doi.org/10.1021/acs.chemrev.5b00291.

(55) He, L.; Shang, J.; Theato, P. Preparation of Dual Stimuli-Responsive Block Copolymers Based on Different Activated Esters with Distinct Reactivities. *Eur. Polym. J.* **2015**, *69*, 523–531. https://doi.org/10.1016/J.EURPOLYMJ.2015.01.045.

(56) Li, Y.; Beija, M.; Laurent, S.; Elst, L. vander; Muller, R. N.; Duong, H. T. T.; Lowe, A. B.; Davis, T. P.; Boyer, C. Macromolecular Ligands for Gadolinium MRI Contrast Agents. *Macromolecules* **2012**, *45* (10), 4196–4204. https://doi.org/10.1021/ma300521c.

(57) Beija, M.; Li, Y.; Lowe, A. B.; Davis, T. P.; Boyer, C. Factors Influencing the Synthesis and the Post-Modification of PEGylated Pentafluorophenyl Acrylate Containing Copolymers. *Eur. Polym. J.* **2013**, *49* (10), 3060–3071. https://doi.org/10.1016/J.EURPOLYMJ.2013.05.003.

(58) Ulrich, S.; Sadeghpour, A.; Rossi, R. M.; Bruns, N.; Boesel, L. F. Wide Range of Functionalized Poly(N-Alkyl Acrylamide)-Based Amphiphilic Polymer Conetworks via Active Ester Precursors. *Macromolecules* **2018**, *51* (14), 5267–5277. https://doi.org/10.1021/acs.macromol.8b00841.

(59) Nilles, K.; Theato, P. Sequential Conversion of Orthogonally Functionalized Diblock Copolymers Based on Pentafluorophenyl Esters. *J. Polym. Sci. Part Polym. Chem.* **2010**, *48* (16), 3683–3692. https://doi.org/10.1002/pola.24152.

(60) Chua, G. B. H.; Roth, P. J.; Duong, H. T. T.; Davis, T. P.; Lowe, A. B. Synthesis and Thermoresponsive Solution Properties of Poly[Oligo(Ethylene Glycol) (Meth)Acrylamide]s: Biocompatible PEG Analogues. *Macromolecules* **2012**, *45* (3), 1362–1374. https://doi.org/10.1021/ma202700y.

(61) Lowe, A. B. Thiol-Ene "Click" Reactions and Recent Applications in Polymer and Materials Synthesis. *Polym. Chem.* **2010**, *1* (1), 17–36. https://doi.org/10.1039/B9PY00216B.

(62) Haldón, E.; Nicasio, M. C.; Pérez, P. J. Copper-Catalysed Azide–Alkyne Cycloadditions (CuAAC): An Update. *Org. Biomol. Chem.* **2015**, *13* (37), 9528–9550. https://doi.org/10.1039/C5OB01457C.

(63) Agard, N. J.; Prescher, J. A.; Bertozzi, C. R. A Strain-Promoted [3 + 2] Azide−Alkyne Cycloaddition for Covalent Modification of Biomolecules in Living Systems. *J. Am. Chem. Soc.* **2004**, *126* (46), 15046–15047. https://doi.org/10.1021/ja044996f.

(64) Jewett, J. C.; Sletten, E. M.; Bertozzi, C. R. Rapid Cu-Free Click Chemistry with Readily Synthesized Biarylazacyclooctynones. *J. Am. Chem. Soc.* **2010**, *132* (11), 3688–3690. https://doi.org/10.1021/ja100014q.

(65) Ferruti, P.; Bettelli, A.; Feré, A. High Polymers of Acrylic and Methacrylic Esters of N-Hydroxysuccinimide as Polyacrylamide and Polymethacrylamide Precursors. *Polymer* **1972**, *13* (10), 462–464. https://doi.org/10.1016/0032-3861(72)90084-5.

(66) Eberhardt, M.; Mruk, R.; Zentel, R.; Théato, P. Synthesis of Pentafluorophenyl(Meth)Acrylate Polymers: New Precursor Polymers for the Synthesis of Multifunctional Materials. *Eur. Polym. J.* **2005**, *41* (7), 1569–1575. https://doi.org/10.1016/j.eurpolymj.2005.01.025.

(67) Li, X. S.; Gan, L. H.; Gan, Y. Y. Controlled Polymerization of 2,3,5,6-Tetrafluorophenyl Methacrylate. *Polymer* **2008**, *49* (7), 1879–1884. https://doi.org/10.1016/j.polymer.2008.02.013.

(68) Kakuchi, R.; Theato, P. Changing the Reactivity of Polymeric Activated Esters by Temperature: On–Off Switching of the Reactivity of Poly(4-Acryloxyphenyldimethylsulfonium Triflate). *Macromolecules* **2012**, *45* (3), 1331–1338. https://doi.org/10.1021/ma202175z.

(69) Alex, J.; Ulbrich, J.; Rosales-Guzmán, M.; Weber, C.; Schubert, U. S.; Guerrero-Sanchez, C. Kinetic Investigations on Homo- and Co-Polymerizations of Pentafluorophenyl (Meth)Acrylates. *Eur. Polym. J.* **2021**, *143*, 110175. https://doi.org/10.1016/J.EURPOLYMJ.2020.110175.

(70) Bathfield, M.; D'Agosto, F.; Spitz, R.; Charreyre, M.-T.; Delair, T. Versatile Precursors of Functional RAFT Agents. Application to the Synthesis of Bio-Related End-Functionalized Polymers. *J. Am. Chem. Soc.* **2006**, *128* (8), 2546–2547. https://doi.org/10.1021/ja057481c.

(71) Lecolley, F.; Tao, L.; Mantovani, G.; Durkin, I.; Lautru, S.; Haddleton, D. M. A New Approach to Bioconjugates for Proteins and Peptides ("Pegylation") Utilising Living Radical Polymerisation. *Chem. Commun.* **2004**, No. 18, 2026–2027. https://doi.org/10.1039/B407712A.

(72) Cristiani, T. R.; Filippidi, E.; Behrens, R. L.; Valentine, M. T.; Eisenbach, C. D. Tailoring the Toughness of Elastomers by Incorporating Ionic Cross-Linking. *Macromolecules* **2020**, *53* (10), 4099–4109. https://doi.org/10.1021/acs.macromol.0c00500.

(73) Heo, J.; Kang, T.; Jang, S. G.; Hwang, D. S.; Spruell, J. M.; Killops, K. L.; Waite, J. H.; Hawker, C. J. Improved Performance of Protected Catecholic Polysiloxanes for Bioinspired Wet Adhesion to Surface Oxides. *J. Am. Chem. Soc.* **2012**, *134* (49), 20139–20145. https://doi.org/10.1021/ja309044z.

(74) Ulrich, S.; Osypova, A.; Panzarasa, G.; Rossi, R. M.; Bruns, N.; Boesel, L. F. Pyranine-Modified Amphiphilic Polymer Conetworks as Fluorescent Ratiometric pH Sensors. *Macromol. Rapid Commun.* **2019**, *40* (21), 1900360. https://doi.org/10.1002/marc.201900360.

(75) Li, W.; Zhang, L.; Ge, X.; Xu, B.; Zhang, W.; Qu, L.; Choi, C. H.; Xu, J.; Zhang, A.; Lee, H.; Weitz, D. A. Microfluidic Fabrication of Microparticles for Biomedical Applications. *Chem. Soc. Rev.* **2018**, *47* (15), 5646–5683. https://doi.org/10.1039/c7cs00263g.

(76) Daly, A. C.; Riley, L.; Segura, T.; Burdick, J. A. Hydrogel Microparticles for Biomedical Applications. *Nat. Rev. Mater.* **2020**, *5* (1), 20–43. https://doi.org/10.1038/s41578-019-0148-6.

(77) Plutschack, M. B.; Pieber, B.; Gilmore, K.; Seeberger, P. H. The Hitchhiker's Guide to Flow Chemistry Â¥. *Chem. Rev.* **2017**, *117* (18), 11796–11893. https://doi.org/10.1021/acs.chemrev.7b00183.

(78) Dario Cambié, Cambié; Bottecchia, C.; Straathof, N. J. W.; Hessel, V.; Noë, T. Applications of Continuous-Flow Photochemistry in Organic Synthesis, Material Science, and Water Treatment. **2016**. https://doi.org/10.1021/acs.chemrev.5b00707.

(79) Singh, R.; Veeramani, K.; Bajpai, R.; Kumar, A. High-Throughput Template-Free Continuous Flow Synthesis of Polyaniline Nanofibers. *Ind. Eng. Chem. Res.* **2019**, *58* (15), 5864–5872. https://doi.org/10.1021/acs.iecr.8b04507.

(80) Zaquen, N.; Kadir, A. M. N. B. P. H. A.; Iasa, A.; Corrigan, N.; Junkers, T.; Zetterlund, P. B.; Boyer, C. Rapid Oxygen Tolerant Aqueous RAFT Photopolymerization in Continuous Flow Reactors. *Macromolecules* **2019**, *52* (4), 1609–1619. https://doi.org/10.1021/acs.macromol.8b02628.

(81) Guidi, M.; Seeberger, P. H.; Gilmore, K. How to Approach Flow Chemistry. *Chem. Soc. Rev.* **2020**, *49* (24), 8910–8932. https://doi.org/10.1039/C9CS00832B.

(82) Reis, M. H.; Leibfarth, F. A.; Pitet, L. M. Polymerizations in Continuous Flow: Recent Advances in the Synthesis of Diverse Polymeric Materials. *ACS Macro Lett.* **2020**, *9* (1), 123–133. https://doi.org/10.1021/acsmacrolett.9b00933.

(83) Tonhauser, C.; Natalello, A.; Löwe, H.; Frey, H. Microflow Technology in Polymer Synthesis. *Macromolecules* **2012**, *45* (24), 9551–9570. https://doi.org/10.1021/ma301671x.

(84) Günther, A.; Jensen, K. F. Multiphase Microfluidics: From Flow Characteristics to Chemical and Materials Synthesis. *Lab. Chip* **2006**, *6* (12), 1487–1503. https://doi.org/10.1039/B609851G.

(85) Baret, J.-C. Surfactants in Droplet-Based Microfluidics. *Lab Chip* **2012**, *12* (3), 422–433. https://doi.org/10.1039/C1LC20582J.

(86) Song, H.; Chen, D. L.; Ismagilov, R. F. Reactions in Droplets in Microfluidic Channels. *Angew. Chem. Int. Ed.* **2006**, *45* (44), 7336–7356. https://doi.org/10.1002/ANIE.200601554@10.1002/(ISSN)1521-3773.MICROFLUIDICS.

(87) Reis, M. H.; Varner, T. P.; Leibfarth, F. A. The Influence of Residence Time Distribution on Continuous-Flow Polymerization. *Macromolecules* **2019**, *52* (9), 3551–3557. https://doi.org/10.1021/acs.macromol.9b00454.

(88) Reis, M.; Gusev, F.; Taylor, N. G.; Chung, S. H.; Verber, M. D.; Lee, Y. Z.; Isayev, O.; Leibfarth, F. A. Machine-Learning-Guided Discovery of 19F MRI Agents Enabled by Automated Copolymer Synthesis. *J. Am. Chem. Soc.* **2021**, *143* (42), 17677–17689. https://doi.org/10.1021/jacs.1c08181.

(89) Leibfarth, F. A.; Johnson, J. A.; Jamison, T. F. Scalable Synthesis of Sequence-Defined, Unimolecular Macromolecules by Flow-IEG. *Proc. Natl. Acad. Sci.* **2015**, *112* (34), 10617–10622. https://doi.org/10.1073/pnas.1508599112.

(90) Horn, A. G.; Johnston, T. C.; Guironnet, D. Biphasic Seeded Emulsion Polymerization in a Tubular Flow Reactor. *Ind. Eng. Chem. Res.* **2020**, *59* (22), 10389–10396. https://doi.org/10.1021/acs.iecr.0c00961.

(91) Walsh, D. J.; Guironnet, D. Macromolecules with Programmable Shape, Size, and Chemistry. *Proc. Natl. Acad. Sci. U. S. A.* **2019**, *116* (5), 1538–1542. https://doi.org/10.1073/pnas.1817745116.

(92) Walsh, D. J.; Dutta, S.; Sing, C. E.; Guironnet, D. Engineering of Molecular Geometry in Bottlebrush Polymers. *Macromolecules* **2019**, *52* (13), 4847–4857. https://doi.org/10.1021/acs.macromol.9b00845.

(93) Walsh, D. J.; Schinski, D. A.; Schneider, R. A.; Guironnet, D. General Route to Design Polymer Molecular Weight Distributions through Flow Chemistry. *Nat. Commun.* **2020**, *11* (1), 3094. https://doi.org/10.1038/s41467-020-16874-6.

(94) Destgeer, G.; Ouyang, M.; Wu, C.-Y.; Carlo, D. D. Fabrication of 3D Concentric Amphiphilic Microparticles to Form Uniform Nanoliter Reaction Volumes for Amplified Affinity Assays. *Lab. Chip* **2020**, *20* (19), 3503–3514. https://doi.org/10.1039/D0LC00698J.

(95) Liu, K.; Corrigan, N.; Postma, A.; Moad, G.; Boyer, C. A Comprehensive Platform for the Design and Synthesis of Polymer Molecular Weight Distributions. *Macromolecules* **2020**, *53* (20), 8867–8882. https://doi.org/10.1021/acs.macromol.0c01954.

(96) Corrigan, N.; Almasri, A.; Taillades, W.; Xu, J.; Boyer, C. Controlling Molecular Weight Distributions through Photoinduced Flow Polymerization. *Macromolecules* **2017**, *50* (21), 8438–8448. https://doi.org/10.1021/acs.macromol.7b01890.

(97) Ghanem, A.; Lemenand, T.; Della Valle, D.; Peerhossaini, H. Static Mixers: Mechanisms, Applications, and Characterization Methods – A Review. *Chem. Eng. Res. Des.* **2014**, *92* (2), 205–228. https://doi.org/10.1016/j.cherd.2013.07.013.

(98) Günther, A.; Jhunjhunwala, M.; Thalmann, M.; Schmidt, M. A.; Jensen, K. F. Micromixing of Miscible Liquids in Segmented Gas-Liquid Flow. *Langmuir* **2005**, *21* (4), 1547–1555. https://doi.org/10.1021/la0482406.

(99) Zhou, Y.; Gu, Y.; Jiang, K.; Chen, M. Droplet-Flow Photopolymerization Aided by Computer: Overcoming the Challenges of Viscosity and Facilitating the Generation of Copolymer Libraries. *Macromolecules* **2019**, *52* (15), 5611–5617. https://doi.org/10.1021/acs.macromol.9b00846.

(100) Song, J.; Zhang, S.; Wang, K.; Wang, Y. Synthesis of Million Molecular Weight Polyacrylamide with Droplet Flow Microreactors. *J. Taiwan Inst. Chem. Eng.* **2019**, *98*, 78–84. https://doi.org/10.1016/j.jtice.2018.05.008.

(101) Chen, D. L.; Li, L.; Reyes, S.; Adamson, D. N.; Ismagilov, R. F. Using Three-Phase Flow of Immiscible Liquids To Prevent Coalescence of Droplets in Microfluidic Channels: Criteria To Identify the Third Liquid and Validation with Protein Crystallization. *Langmuir* **2007**, *23* (4), 2255–2260. https://doi.org/10.1021/la062152z.

(102) Nightingale, A. M.; Phillips, T. W.; Bannock, J. H.; de Mello, J. C. Controlled Multistep Synthesis in a Three-Phase Droplet Reactor. *Nat. Commun.* **2014**, *5* (1), 3777. https://doi.org/10.1038/ncomms4777.

(103) Kashid, M. N.; Agar, D. W. Hydrodynamics of Liquid–Liquid Slug Flow Capillary Microreactor: Flow Regimes, Slug Size and Pressure Drop. *Chem. Eng. J.* **2007**, *131* (1–3), 1–13. https://doi.org/10.1016/J.CEJ.2006.11.020.

(104) Kashid, M. N.; Rivas, D. F.; Agar, D. W.; Turek, S. On the Hydrodynamics of Liquid–Liquid Slug Flow Capillary Microreactors. *Asia-Pac. J. Chem. Eng.* **2008**, *3* (2), 151–160. https://doi.org/10.1002/apj.127.

(105) Ahmadpour, A.; Amani, E.; Esmaili, M. Numerical Simulation of Shear Thinning Slug Flows: The Effect of Viscosity Variation on the Shape of Taylor Bubbles and Wall Shear Stress. *J. Braz. Soc. Mech. Sci. Eng.* **2019**, *41* (1), 48. https://doi.org/10.1007/s40430-018-1558-x.

(106) Garstecki, P.; J. Fuerstman, M.; A. Stone, H.; M. Whitesides, G. Formation of Droplets and Bubbles in a Microfluidic T-Junction—Scaling and Mechanism of Break-Up. *Lab. Chip* **2006**, *6* (3), 437–446. https://doi.org/10.1039/B510841A.

(107) Thulasidas, T. C.; Abraham, M. A.; Cerro, R. L. Flow Patterns in Liquid Slugs during Bubble-Train Flow inside Capillaries. *Chem. Eng. Sci.* **1997**, *52* (17), 2947–2962. https://doi.org/10.1016/S0009-2509(97)00114-0.

(108) Feng, Y.; White, A. K.; Hein, J. B.; Appel, E. A.; Fordyce, P. M. MRBLES 2.0: High-Throughput Generation of Chemically Functionalized Spectrally and Magnetically Encoded Hydrogel Beads Using a Simple Single-Layer Microfluidic Device. *Microsyst. Nanoeng.* **2020**, *6* (1), 1–13. https://doi.org/10.1038/s41378-020-00220-3.

(109) Krutkramelis, K.; Xia, B.; Oakey, J. Monodisperse Polyethylene Glycol Diacrylate Hydrogel Microsphere Formation by Oxygen-Controlled Photopolymerization in a Microfluidic Device. *Lab. Chip* **2016**, *16* (8), 1457–1465. https://doi.org/10.1039/C6LC00254D.

Chapter 2. Modular Synthesis and Patterning of High Stiffness Networks by Post Polymerization Functionalization with Iron-Catechol Complexes

This chapter was initially published in *Macromolecules*. Adapted with permission *Macromolecules*, **2023,** 56, 6, 2268–2276. Copyright 2023, American Chemical Society. CC BY 4.0 https://creativecommons.org/licenses/by/4.0/

2.1 Abstract

Bioinspired iron-catechol crosslinks have shown remarkable success in increasing the mechanical properties of polymer networks, in part due to clustering of Fe^{3+}-catechol domains which act as secondary network reinforcing sites. We report a versatile synthetic procedure to prepare modular PEG-acrylate networks with independently tunable covalent bis(acrylate) and supramolecular Fe^{3+}-catechol crosslinking. Initial control of network structure is achieved through radical polymerization and crosslinking, followed by post polymerization incorporation of catechol units via quantitative active ester chemistry and subsequent complexation with iron salts. By tuning the ratio of each building block, dual crosslinked networks reinforced by clustered iron-catechol do-mains are prepared and exhibit a wide range of properties (Young's moduli up to ~245 MPa), well beyond the values achieved through purely covalent crosslinking. This stepwise approach to mixed covalent and metal-ligand crosslinked networks also permits local patterning of PEG-based films through masking techniques forming distinct hard, soft, and gradient regions. -.

2.2 Introduction

Structural biopolymers are characterized by outstanding performance and physical properties yet are derived from simple building blocks and self-assembling network motifs[1–4]. In addition to covalent crosslinking, enhanced performance can arise from metal-ligand interactions and mineralization as in marine invertebrates[5–9], or through fiber reinforced systems in wood[10], cartilage[11], tendon[12], and adaptive soft tissues[13]. These structural biopolymers rely on hierarchical network control through both localization of self-assembling motifs and chemical control of covalent and noncovalent crosslinking[2–5,7]. This hierarchical control allows biological systems to achieve an extensive range of materials properties while also providing a set of design rules for the preparation of synthetic networks with enhanced performance[2].

Synthetic network design has sought to mimic the high stiffness and toughness of biological materials through classical strategies such as modulating crosslink density[14,15], incorporating rigid fillers into soft polymer matrices[16] or tuning network crystallinity[17] to alter network mechanical properties. More recent approaches have directly used bioinspired molecular motifs, allowing for the design of complex materials with hierarchical strengthening motifs. Examples include double networks[18,19], host-guest interactions[20,21], hydrogen bonding[22], and metal-ligand interactions[23,24], with metal-ligand systems having the added advantage of tunability via the strength and nature of the metal-ligand bond. This feature allows network stiffness and relaxation properties to be controlled through careful selection of metal-ligand dissociation times[23,25–30].

For accessing high stiffness networks, Fe^{3+}-catechol bonds are of interest due to their near covalent bond strength and pH dependent association number (mono *vs.* bis *vs.* tris) with

the latter having a significant influence over the resulting crosslink structure[5,26,31–35]. Recent work from the Valentine group has demonstrated the importance of the Fe^{3+}-catechol clustering and ionomeric domains for toughening epoxy-based networks leading to high stiffness materials in the dry state (E ~250 MPa)[36,37]. In this system, the catechol unit was introduced as a bis(triethylsilyl) protected epoxide during the epoxy/amine network formation reaction followed by deprotection. This combination of a covalent network with a percolating metal-ligand cluster network represents a promising approach to creating stiff, strong, and tough load-bearing polymer networks. Building on this success, there is significant opportunity for extending this design concept to a more modular synthetic strategy based on initial rapid and orthogonal free radical crosslinking followed by secondary functionalization with readily available catechol derivatives such as dopamine, alleviating the requirement for protection/deprotection of catechol moieties[38,39] (**Figure 2.1**). The versatility of radical crosslinking systems and the wide availability of starting materials would also enable the preparation of patterned materials for soft robotics[40,41], tissue engineering scaffolds[42], and high strength, functional 3D printed materials[43].

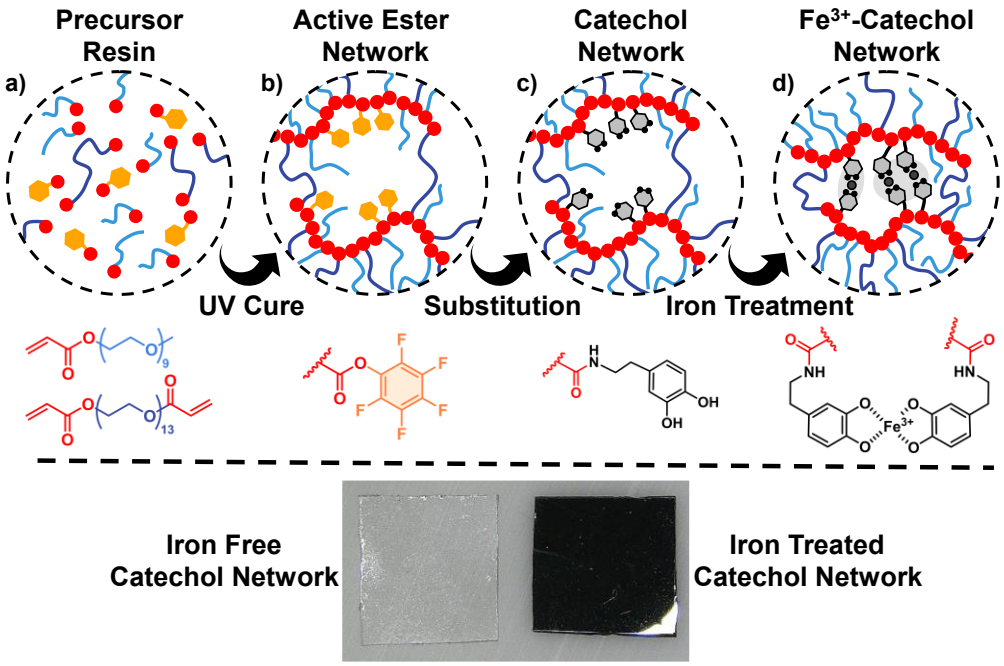


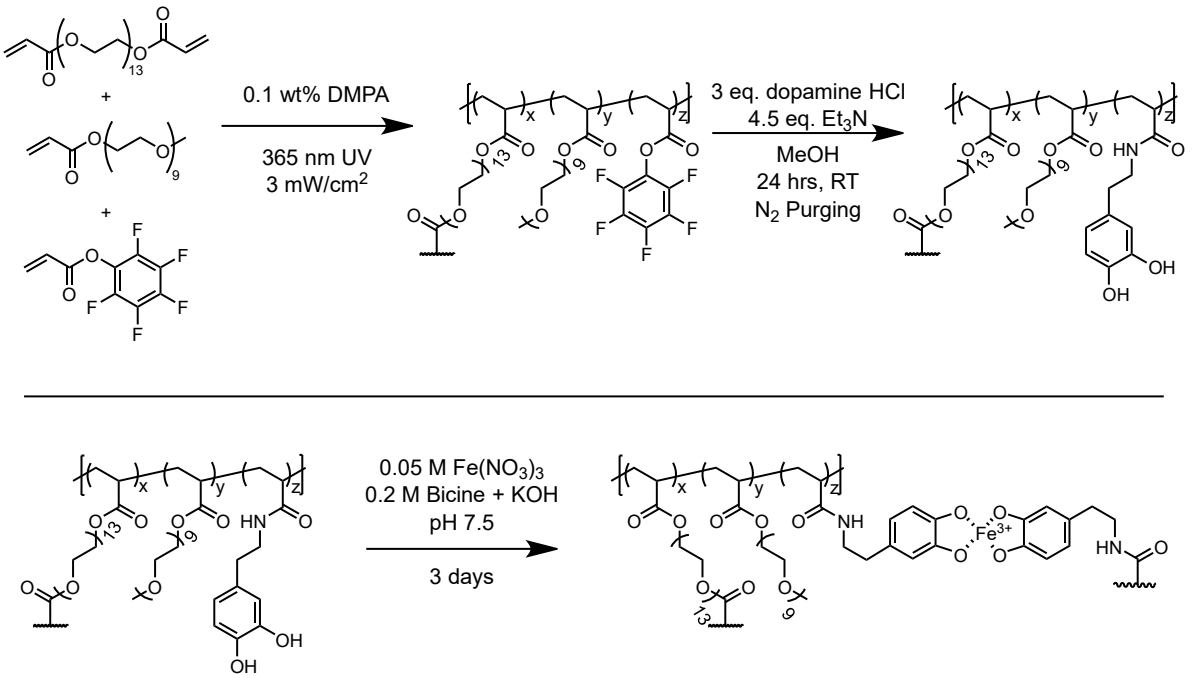
Figure 2.1. The modular processing of dual crosslinked networks leads to a highly tunable and patternable material following the steps from left to right of the (a) precursor resin, (b) active ester network, (c) catechol substitution, and (d) iron complexation with (bottom) images of catechol networks before and after Fe3+ complexation.

2.3 Results and Discussion

In this work, we develop a synthetic platform for preparing and patterning high-stiffness networks reinforced by non-covalent Fe^{3+}-catechol crosslinks in simple, modular network designs[44]. Previously, we have reported a two-step strategy for the general synthesis of catechol containing films that uses initial radical crosslinking followed by post polymerization modification of pentafluorophenyl esters with a variety of commercially available functional amines including dopamine[44]. Grignon et al.[45] recently described the use of the same two-step strategy for the modification of RAFT derived polymers which illustrates the utility of this approach[44,46]. Application of these techniques to the functionalization of PEG-acrylate crosslinked networks with dopamine-derived catechols and assembly with Fe^{3+}

salts leads to the formation of tough non-covalent crosslinks that reinforce the network structure (**Figure 2.1**). Importantly, the inherent tunability of this strategy allows a wide range of mechanical property changes and increased mechanical stiffness to be obtained. Additionally, through use of soft lithography approaches, we demonstrate the selective patterning of Fe^{3+} incorporation into the network which provides novel spatial control of metal-ligand crosslink formation and thin film strengthening.

Polymer networks were prepared according to **Scheme 2.1** from a solvent-free mixture comprised of three monomers: an active ester monomer, (pentafluorophenyl acrylate, PFPA), a diacrylate crosslinker (poly(ethylene glycol) diacrylate, PEGDA, M_n 700), and a monofunctional diluent monomer (poly(ethylene glycol) methyl ether acrylate, PEGMEA, M_n 480). Initiation under UV irradiation at 365 nm for 2 minutes using 2,2-dimethoxy-2-phenylacetophenone as the photo-initiator (0.1 wt.%, DMPA) led to effective polymerization and crosslinking. Networks were prepared between quartz plates to form robust films, with film thickness controlled by spacers placed between the plates. Key to the success of this strategy was the ability to engineer mechanically tough films that could be swollen in a variety of solvents and at different pH values and dried repeatedly without cracking or damage. To achieve this, the amount of PEGDA crosslinker was maintained at low levels (~3-4 mol%) in the active ester films to yield soft networks that avoided the observed brittleness with highly crosslinked films (>5 mol%). Through facile radical copolymerization of active ester and PEG-acrylate monomers, a diverse range of materials could therefore be prepared with varied crosslinker content and active ester side chain densities (**Tables 2.1, 2.2,** and **Table A.1**).



Scheme 2.1. Polymerization of networks, substitution of active ester groups with catechol moieties and subsequent complexation with Fe^{3+}.

Table 2.1. Library of iron-catechol reinforced network compositions (mixed crosslinkers). Theoretical maximum crosslink density is determined from the combined content of covalent (PEGDA) crosslinking units and metal ligand (Fe^{3+}-catechol linkages) divided by two, assuming only bis complexation of two catechol moieties.

Network Composition			**Theor. Max. Crosslink Density (mmol/cm^3)**			**Metal-Ligand to Covalent Crosslink Ratio**
mol% Catechol	mol% PEGDA	mol% PEGMEA	Total Crosslink Density	Covalent Crosslink Density	Metal-Ligand Crosslink Density	
4.4%	4.4%	91%	0.15	0.1	0.05	0.50
20%	3.9%	76%	0.35	0.1	0.25	2.5
35%	3.5%	61%	0.60	0.1	0.5	5.0
48%	3.2%	49%	0.85	0.1	0.75	7.5
58%	2.9%	39%	1.1	0.1	1.0	10

Table 2.2. Control samples based on covalent-only network crosslinking. Theoretical maximum crosslink density is determined from the mmol/cm^3 content of covalent (PEGDA) crosslinkers in the final network.

Network Composition		**Theoretical Maximum Crosslink Density (mmol/cm^3)**
mol% PEGDA	mol% PEGMEA	
4.5%	95.5%	0.1
12%	88%	0.25
24%	76%	0.50
54%	46%	1.0
100%	0%	1.6

As detailed previously[39], catechol units were incorporated into these networks via active ester substitution of pentafluorophenyl esters using commercially available dopamine (2-(3,4-dihydroxyphenyl)ethylamine). Films were soaked in a methanol solution of dopamine hydrochloride (excess) for 24 hours at room temperature, with triethylamine added to deprotonate the dopamine hydrochloride salt (1.5 equivalents of Et_3N per dopamine HCl). The reaction chamber was degassed with nitrogen, as catechols are known to oxidize in the presence of oxygen and under basic conditions to form quinones which can undergo dismutation and aryloxy crosslinking to form undesirable catechol-catechol covalent crosslinks, as well as Michael-type addition with amines to form more complex polydopamine structures[31,32,35,47]. Monitoring by FTIR (Fourier Transform Infra-red Spectroscopy) confirms complete substitution of the active esters with dopamine to form the corresponding amides with no detectable quinone formation. As shown in **Figure 2.2**, resonances at 1780, 1520, and

985 cm^{-1} from the pentafluorophenyl ester group disappear after substitution with dopamine, and a concomitant appearance of an amide stretching resonance is observed at ~1660 cm^{-1}.

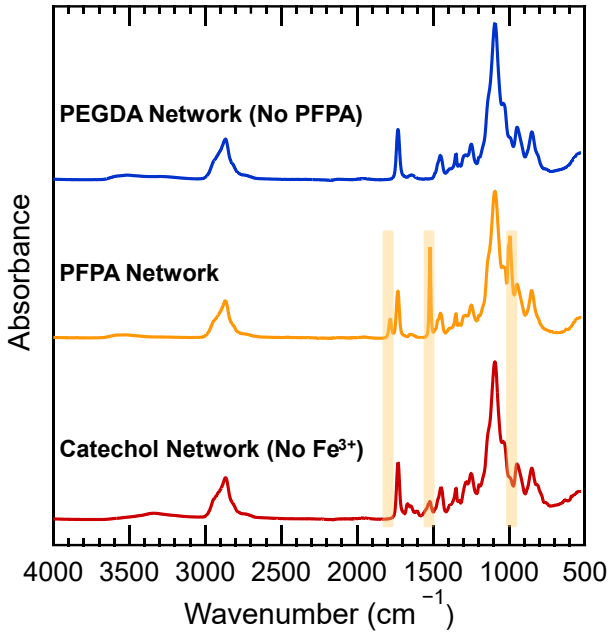


Figure 2.2. FTIR-attenuated total reflection (ATR) of random copolymer networks. From top to bottom: blue trace is a 4.5/95.5 mol% PEGDA/PEGMEA network without PFPA monomer incorporation, yellow trace is a 4/61/35 mol% PEGDA/PEGMEA/PFPA network before substitution, and red trace is PFPA-containing network after reaction with dopamine in MeOH. Key resonances from PFPA (yellow highlighted peaks) at 1780, 1520, and 985 cm^{-1} disappear after substitution with dopamine, with an amide stretching band appearing near 1660 cm^{-1}.

To illustrate the reproducibility of this process, a wide range of PFPA networks were prepared and after active ester substitution under an inert atmosphere, all samples were transparent and colorless, indicating little or no catechol oxidation. In contrast, reactions performed in the presence of air consistently yielded brown products, which is indicative of catechol oxidation and crosslinking[31,32,35,47]. To demonstrate oxidation under controlled conditions, control experiments were performed by intentionally oxidizing films in a solution

of $NaIO_4$ (0.05 M)[33,48], which immediately resulted in a change in physical appearance from colorless to orange/red[31,33,48–50] (see **Appendix A**, **Figure A.1**). After catechol substitution, films were dialyzed for 24 hours in 0.1 M HCl followed by an additional 24-hour dialysis in 1 mM HCl to remove residual, unreacted dopamine and triethylamine salts. The second dialysis step raises the pH of the crosslinked network to be closer to that of the Fe^{3+} complexation solution (pH 7.5), which favors formation of Fe^{3+}-catechol bis-complexes[31,32].

A wide range of conditions were examined for formation of Fe^{3+}-catechol complexes within the crosslinked films and exposure of the catechol-containing networks to an aqueous solution containing 0.05 M $Fe(NO_3)_3$ and 0.2 M bicine buffered with KOH at pH 7.5 was found to be mild and the most reproducible process[36,37]. This procedure allows soluble iron-bicine complexes to diffuse into the covalently crosslinked films and subsequently exchange with the catechol ligands to form a stable, secondary set of network crosslinks based on bis-catecholate iron complexes. Excess iron salts and bicine were removed from films by thoroughly dialyzing the swollen networks in DI water. To maintain mechanical integrity of the films during drying, it was important to employ solvent gradients after the iron treatment and washing steps. This involves slow addition of solvents with decreasing polarity to gradually dehydrate large surface area films prior to drying under vacuum. This gradual switch from aqueous to low polarity organic solvents mitigated cracking from film contraction during drying and rapid solvent switching (see **Appendix A** for details).

Raman spectroscopy confirmed the primary formation of bis-Fe^{3+}-catechol complexes in iron treated films (**Figure 2.3**). Raman signals at 630, 590, and 520 cm^{-1} were observed and are indicative of Fe^{3+}-catechol vibrations with signals at 1200-1500 cm^{-1} corresponding to catechol ring vibrations after complexation[31,37]. Significantly, Raman microscopy imaging of

the crosslinked films showed the homogeneous appearance of signals for bis-Fe^{3+}-catechol complexes throughout the thickness of the films and were observed to be absent in iron-free catechol films.

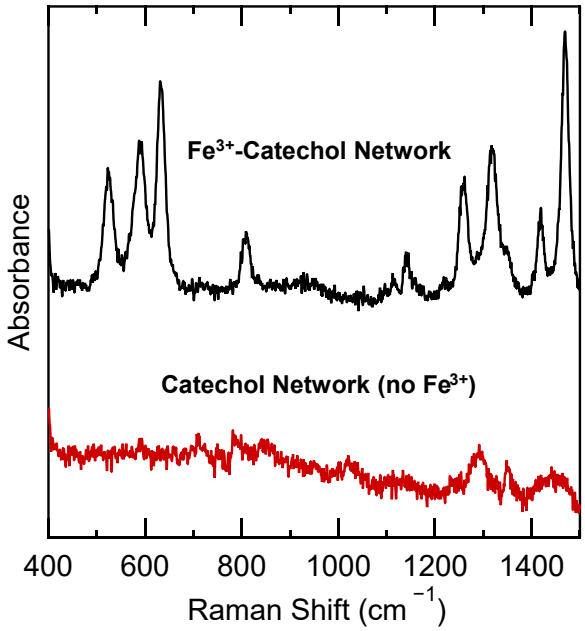


Figure 2.3. Raman spectra of 3/39/58 mol% PEGDA/PEGMEA/PFPA films after substitution with dopamine. From top to bottom: black trace is film after complexation with Fe^{3+}, and red trace is corresponding film without iron treatment. Resonances at 630, 590, and 520 cm^{-1} indicate presence of Fe^{3+}-catechol bis-complexes.[31,37]

Further analysis of the network morphology utilized small angle x-ray scattering (SAXS) to identify the clustered microstructure of Fe-catechol units within the bulk films[36,37]. Prior literature has highlighted the importance of Fe-catechol clustered domains on reinforcing network structure[36,37] as well as the impact of ionic structures on mechanical properties[51,52]. Initial SAXS measurements were therefore performed on control PEG

networks and precursor films to correlate microstructural changes with variations in crosslinker density, pentafluorophenyl ester incorporation, and Fe^{3+}-catechol complexation. Scattering was conducted on both water swollen and dry films, with swollen structures providing sufficient contrast for measurement (data from dry films is included in **Appendix A - Fig. A.11**). Film compositions were chosen to be homogeneous in iron content throughout the film cross section, as discussed below, by controlling thickness, Fe^{3+} treatment, and catechol grafting density.

In accord with previous work by Helgeson[53], pure PEGDA networks display heterogeneous, star-like microstructures which deviate from ideal network topologies. Key features are observed in the SAXS trace of the swollen, pure PEGDA sample (100 mol% PEGDA, **Fig. 2.4a**) such as the low q upturn from the network and minimal contrast between PEG sidechains and short acrylate backbones. Inclusion of PEGMEA as a comonomer results in a brush-like structure with increased acrylate backbone lengths between crosslinks and enhanced contrast between the network backbones and sidechains (4.5 mol% PEGDA, **Fig. 2.4b**). This results in the appearance of a shoulder peak at higher q in the SAXS trace. Here, scattering from PEG sidechain-rich regions is superimposed on the network scattering of the acrylate backbone with minimal other deviations from the pure PEGDA scattering patterns. Such results suggest qualitatively similar levels of heterogeneity across the control samples, and are comparable to expected literature morphologies[53].

Significantly, introduction of the PFPA comonomer leads to the appearance of a peak in SAXS traces, corresponding to a feature of approximately 5 nm in length scale for water-swollen samples (**Figure 2.4c**). This feature is attributed to the correlation length between PFPA rich domains resulting from the hydrophobic character of the pentafluorophenyl ester

coupled with the reactivity ratios for PFPA and PEG acrylates ($r_{PFPA}/r_{PEG\text{-}acrylate}$ of 1.4/0.22) leading to non-statistical incorporation of PFPA repeat units along the backbone[54]. These PFPA rich domains serve as a template for catechol installation with Fe^{3+}-treated films forming clustered domains of Fe^{3+}-catechol complexes at comparable length scale to initial PFPA templating (i.e., ~5 nm) as seen in the shoulder of the swollen, iron treated film (**Fig. 2.4d**). The formation of these domains is further reinforced by a decrease in feature size in SAXS when the samples are dried (**Fig. A.11**). For all samples, a lack of crystalline microstructural features in wide angle x-ray scattering was observed and indicates an amorphous structure (**Fig. A.12**).[36,37]

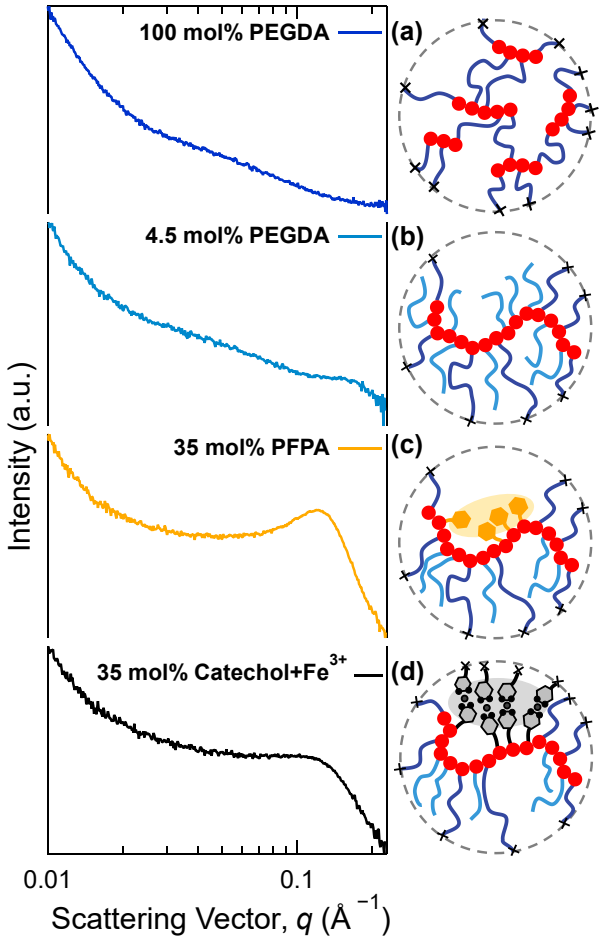


Figure 2.4. Small angle x-ray scattering of water swollen polymer networks and representative cartoons of polymer microstructure. (a) Scattering of 100 mol% PEGDA network, (b) scattering of 4.5/95.5 mol% PEGDA/PEGMEA network, (c) scattering of 4/61/35 mol% PEGDA/PEGMEA/PFPA network, (d) Scattering of 4/61/35 mol% PEGDA/PEGMEA/catechol network after substitution with dopamine and subsequent Fe^{3+} complexation.

The ability to control the level of covalent and non-covalent crosslinking permits characterization of homogeneous, bulk network mechanical properties via beam bending to reveal significant trends across both control networks and Fe^{3+}-catechol systems. For purely covalent networks, the Young's modulus increases from 1.7 MPa to 28.4 MPa as the PEGDA content increases from 4.5 mol% to 100 mol% with the concomitant PEGMEA content decreasing from 95.5% to 0%, This behavior is expected for networks with increasing crosslinking density[55]. Notably, the introduction of Fe^{3+}-catechol units correlated with significant increases in elastic moduli. For networks with constant PEGDA crosslinking (~3-4 mol%), increasing the Fe^{3+}-catechol from 4.4 mol% to 58 mol% resulted in an increase in modulus of ~2 orders of magnitude from 2.7 MPa to 245 MPa, approximately 10x that observed for the purely covalent system (**Fig. 2.5**). Prior studies have attributed this substantial increase in stiffness to the clustering of Fe^{3+}-catechol complexes, which reinforces the existing covalent network framework via formation of ionic domains[36,37].

The impact of the Fe^{3+}-catechol network was further investigated by rheological stress relaxation experiments which shows minimal relaxation, suggesting the Fe^{3+}-catechol bonds exhibit quasistatic crosslink behavior during the timescale of beam-bending testing (see **Appendix A**). Thus, the purely covalent networks can be directly compared with these dual crosslinked networks (covalent + Fe^{3+}-catechol) on the basis of their theoretical maximum crosslinking density (cf., **Tables 2.1** and **2.2**) which is calculated based on diacrylate

crosslinker content and the assumption that all grafted catechol units form bis-Fe^{3+}-catechol crosslinks (**Fig. 2.5**). We find that bis-Fe^{3+}-catechol networks are much stiffer than even the most highly crosslinked covalent PEGDA networks, despite similarities between their theoretical total crosslinking densities. To determine if the increased stiffness of networks incorporating Fe^{3+}-catechol bonds was in part due to oxidation and crosslinking of catechol units, elastic moduli were measured for iron-free samples with 35 mol% and 58 mol% catechol monomers after subjection to oxidative crosslinking by $NaIO_4$.[33,48] It is notable that oxidized films exhibited only modest increases in stiffness from 2.4 MPa to 3.7 MPa and 28 MPa, respectively, which are an order of magnitude lower than corresponding Fe^{3+}-catechol networks, and are comparable to purely covalently crosslinked films. These values further highlight the importance of metal-ligand complexes and associated ionic interactions for achieving high stiffnesses in these materials. While this data demonstrates the impact of bis-Fe^{3+}-catechol complexes, tris-Fe^{3+}-catechol complexes are possible *via* iron incorporation at elevated pH which may lead to interesting future work as modulation of crosslink functionality may change mechanical behavior, but is beyond the scope of this study[31].

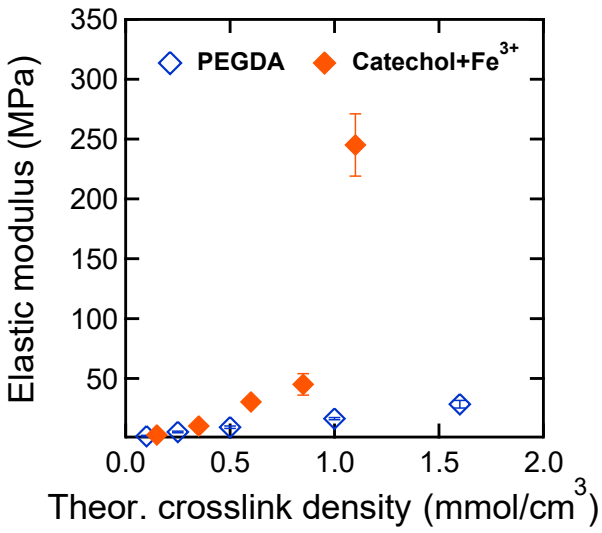


Figure 2.5. Young's moduli, E, from beam bending measurements of dry samples vs. theoretical maximum crosslinking density (mmol/cm^3) for catechol-free PEGDA networks (unfilled blue diamonds) and Fe^{3+}-catechol networks with constant PEGDA covalent crosslinker content of ~3-4 mol% (filled orange diamonds). Error bars represent standard deviations from replicate measurements. Note some error bars are within the bounds of the markers (See **Appendix A** for specific values).

An important advantage of this two-step approach to dual crosslinked materials is the ability to independently tune the level of catechol incorporation and crosslink density of the initial covalent network. To illustrate the potential of this step-wise strategy, gradients in iron content were programmed into the secondary catechol-network by controlling the diffusion rate of the external $Fe(NO_3)_3$ solution into the crosslinked thin films through both covalent crosslinking density and polymer-ion interactions which are both known to slow ion diffusion into water-swollen networks[56–61]. Significantly, the penetration depth of Fe^{3+} ions into the swollen catechol networks was shown to be modulated by changing covalent crosslinking density, catechol grafting density, film thickness, and time. For example, by fixing catechol grafting density and film thickness and varying covalent crosslinking density (i.e., increasing

PEGDA content), optical microscopy reveals that iron incorporation into highly crosslinked networks (7+ mol% PEGDA) is substantially slowed relative to more loosely crosslinked networks (~3-4 mol% PEGDA). As can be seen in **Figure 2.6**, tuning of the iron diffusion results in Fe^{3+}-catechol complex formation that is localized to thin "skin" layers at the external surfaces of the films, with essentially no iron reaching the center of the films. Additional sample specifications are located in **Table A.1**.

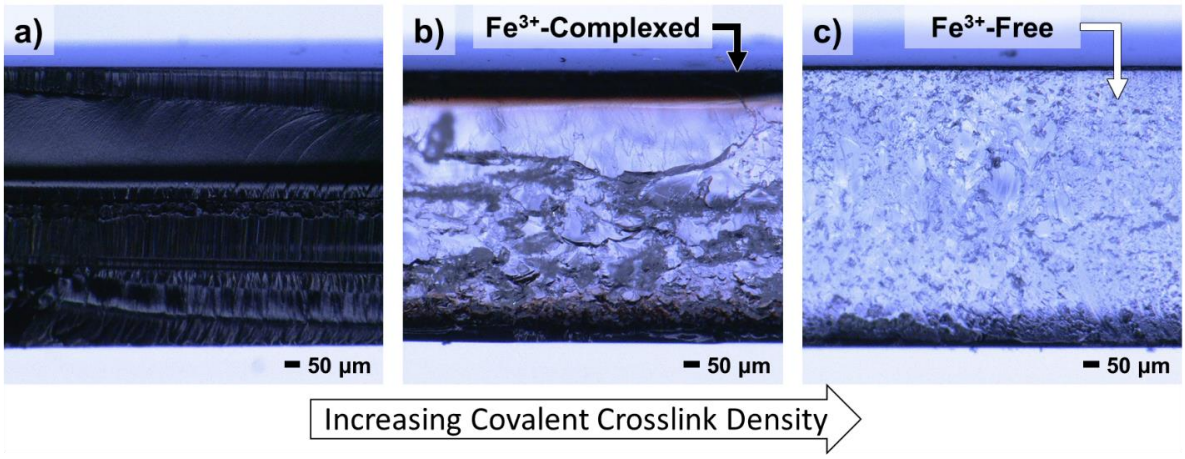


Figure 2.6. Optical microscopy images of cross-sections of films with varied covalent crosslinker content, illustrating differences in iron diffusion rates. (a) 3/39/58 mol% PEGDA/PEGMEA/catechol, (b) 7/33/59 mol% PEGDA/PEGMEA/catechol, (c) 15/24/61 mol% PEGDA/PEGMEA/catechol .

Alternatively, at low covalent crosslinking density (e.g., 3-4 mol% PEGDA), increasing the catechol grafting density from ~4 to 58 mol% results in an increase in the total amount of iron uptake while also hindering ion diffusion into the center of the networks, again forming a gradient in Fe concentration. This can be quantified by energy dispersive x-ray spectroscopy (EDS) line-scans of SEM cross-sections which illustrate more homogeneous Fe^{3+}-catechol complexation in low catechol content samples (≤ 20 mol% catechol-containing

monomers) and more surface-concentrated Fe-domains in networks with increased catechol groups (≥ 35 mol%) (constant film thickness of 1 mm and 72-hour iron treatment) (**Figure 2.7a**). Finally, film thickness is also important for controlling homogeneous formation of Fe^{3+}-catechol crosslinks. For samples with low PEGDA content (~3 mol%) and high catechol content (58 mol%), homogenous Fe^{3+} distributions could be achieved by reducing film thickness from 1 mm to 0.5 mm during the same 72-hour iron treatment (**Figure 2.7b**). The further impact of iron diffusion timescales and surface driven gradients can be seen in **Appendix A** (**Fig. A.7** and **A.8)** and clearly illustrates that Fe^{3+}-catechol formation can be controlled by structural parameters to give a wide variety of mixed crosslink and gradient systems.

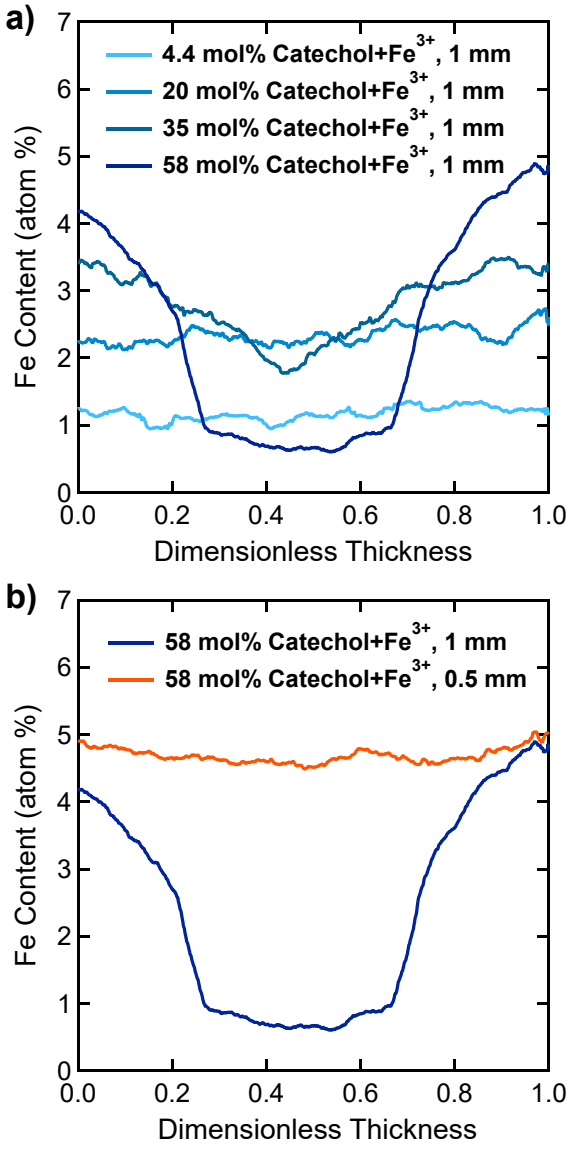


Figure 2.7. SEM EDS characterization of Fe^{3+} distributions across film thicknesses. (a) Fe^{3+} distribution vs. dimensionless thickness for 1 mm thick films with ~3-4 mol% PEGDA and varied catechol content after exposure to Fe^{3+}-solution for 72 hours. (b) Comparison of Fe^{3+} distribution vs. dimensionless thickness for 0.5 mm and 1 mm thick films of 3/39/58 mol% PEGDA/PEGMEA/catechol film after exposure to Fe^{3+}-solution for 72 hours.

This ability to prepare gradient Fe^{3+}-catechol network structures also opens up the possibility of controlling the patterning of Fe^{3+}-catechol domains in the X- and Y-directions.

Soft lithography solution masking techniques coupled with controlled Fe^{3+} diffusion allow 3D network films to be prepared with a diversity of hard (Fe^{3+}-catechol) and soft (catechol only) network patterns[40,62,63]. To illustrate the utility of this strategy, swollen networks were covered with a PDMS mask that preferentially exposed distinct regions of the network surface to Fe^{3+} via a reservoir of buffered $Fe(NO_3)_3$ solution (**Figure 2.8a**). As iron diffusion is relatively slow in networks with high catechol grafting densities, this approach allows for control of feature sizes at resolutions of ~700 □m (cf., QR code in **Figure 2.8b**). Representative patterned films can be seen in **Figure 2.8b-d**. Patterned sections of catechol containing films further display increased rigidity relative to untreated sections of material. For example, as observed in movie S1, the wings of the butterfly shown in **Figure 2.8c** are significantly stiffer than the Fe^{3+}-free matrix. To further demonstrate the dramatic change in mechanical properties, a simple bending demonstration was conducted comparing a patterned Fe^{3+}-containing film and a corresponding precursor film (Fe^{3+}-free) (**Fig. 2.9**). As can be seen in **Figure 2.9**, the catechol containing film is flexible and bends evenly along its length. In direct contrast, the film with a central section containing Fe^{3+}-complexed catechol groups bends asymmetrically with the Fe^{3+}-containing region being significantly stiffer than the precursor film. This approach for patterning stiff regions in a functional network may further provide a modular tool for generating composite-like soft materials[64], as well as a method for patterned adhesion from free catechol groups in iron free sections[65]. Additional details about the techniques used for soft lithography solution masking are provided in **Appendix A**.

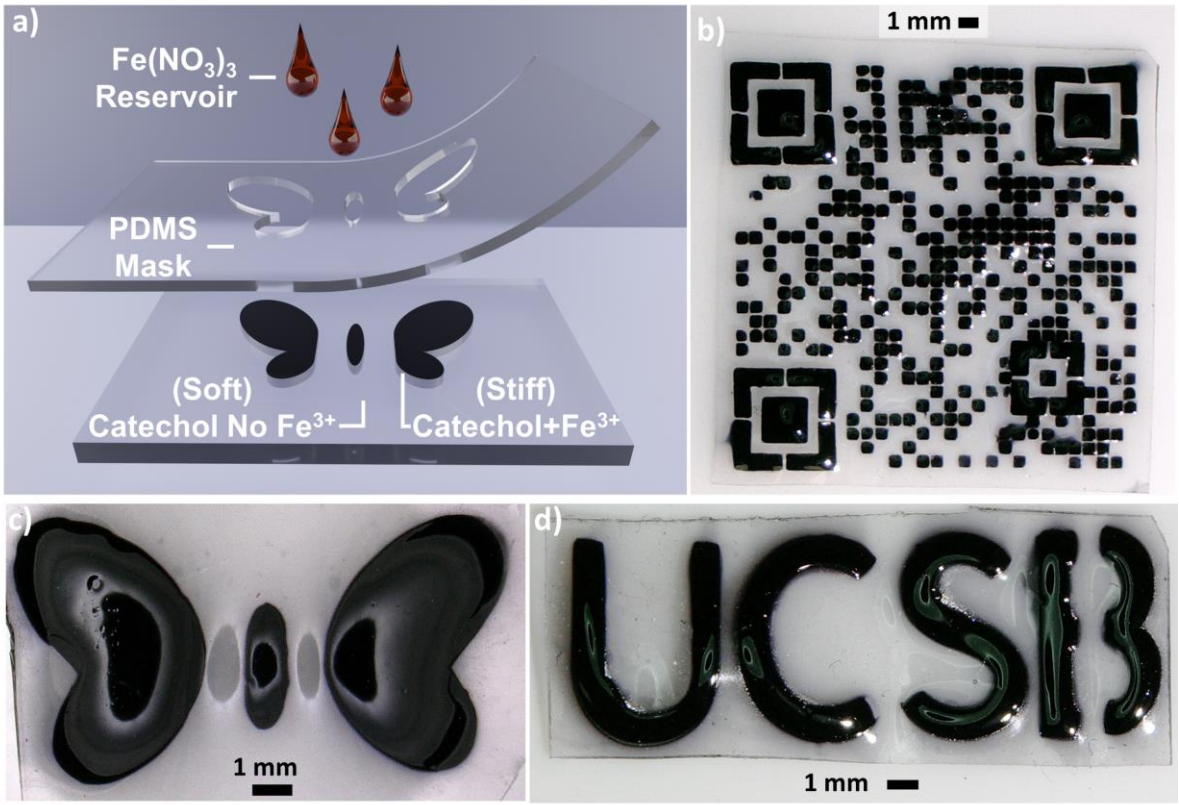


Figure 2.8. (a) 3D rendering of the generalized schematic of the Fe^{3+} patterning approach. (b-d) Images of catechol-containing films (3/39/58 mol% PEGDA/PEGMEA/catechol) after selective patterning with Fe^{3+} through soft lithography styled masking displaying (b) a QR code, (c) a butterfly, and (d) a demonstration of text.

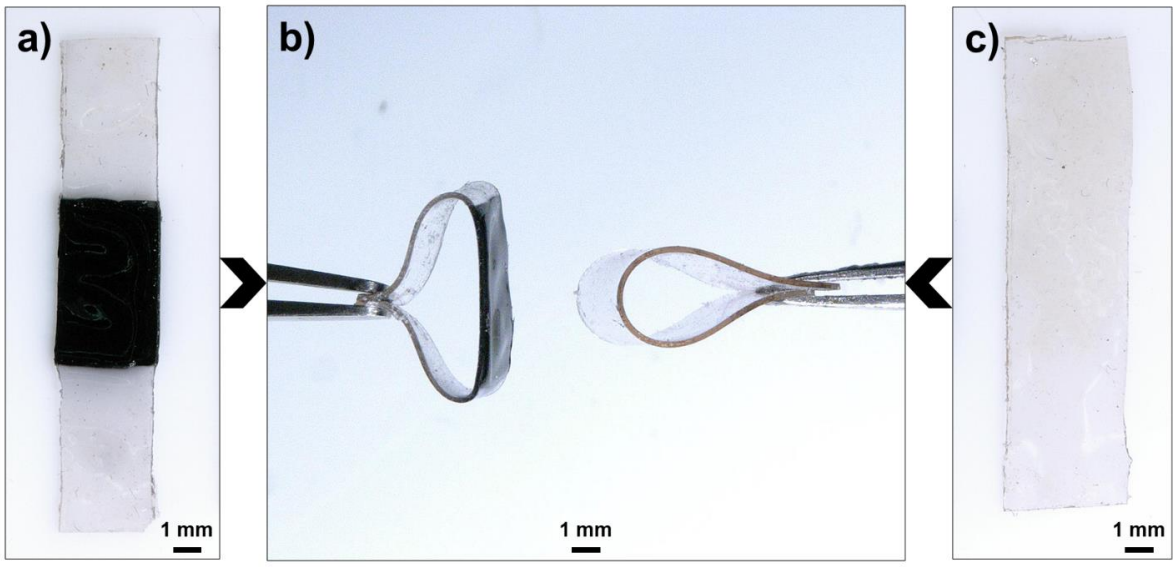


Figure 2.9. (a) Continuous film of 3/39/58 mol% PEGDA/PEGMEA/catechol with a central section functionalized with Fe^{3+}-catechol groups. (b) Comparison of folded film strips between iron-patterned and iron free-networks. (c) Continuous film of 3/39/58 mol% PEGDA/PEGMEA/catechol with no patterning or introduction of Fe^{3+}-catechol groups.

2.4 Conclusion

In this work, a modular approach for preparing mechanically tunable materials using robust stepwise synthesis of dual crosslinked networks is presented. The versatility of free radical crosslinking of vinyl monomers for preparation of an initial functionalized network is combined with the ease of post-modification using active ester substitution to form catechol-grafted networks without the need for protection/deprotection strategies. These catechol functionalized networks can then be mechanically reinforced with Fe^{3+}-catechol crosslinks through simple solution processing to yield tough materials with stiffnesses that exceed those of covalently crosslinked PEGDA networks by up to two orders of magnitude. Furthermore, soft lithography solution masking techniques can leverage controlled iron diffusion into catechol networks to spatially pattern 3D films with hard-soft regions with sub-millimeter feature sizes and to prepare novel gradient systems. The user-friendly nature of this two-step strategy for preparing mechanically tunable and patterned dual, covalent and metal-ligand crosslinked networks enables the development of materials with enhanced properties for soft robotic and bioinspired composite applications.

2.5 References

(1) Fratzl, P.; Weinkamer, R. Nature's Hierarchical Materials. *Prog. Mater. Sci.* **2007**, *52* (8), 1263–1334. https://doi.org/10.1016/j.pmatsci.2007.06.001.

(2) Zhao, X.; Chen, X.; Yuk, H.; Lin, S.; Liu, X.; Parada, G. Soft Materials by Design: Unconventional Polymer Networks Give Extreme Properties. *Chem. Rev.* **2021**, *121* (8), 4309–4372. https://doi.org/10.1021/acs.chemrev.0c01088.

(3) Ganewatta, M. S.; Wang, Z.; Tang, C. Chemical Syntheses of Bioinspired and Biomimetic Polymers toward Biobased Materials. *Nat. Rev. Chem.* **2021**, *5* (11), 753–772. https://doi.org/10.1038/s41570-021-00325-x.

(4) Huang, W.; Restrepo, D.; Jung, J.-Y.; Su, F. Y.; Liu, Z.; Ritchie, R. O.; McKittrick, J.; Zavattieri, P.; Kisailus, D. Multiscale Toughening Mechanisms in Biological Materials and Bioinspired Designs. *Adv. Mater.* **2019**, *31* (43), 1901561. https://doi.org/10.1002/adma.201901561.

(5) Harrington, M. J.; Masic, A.; Holten-Andersen, N.; Waite, J. H.; Fratzl, P. Iron-Clad Fibers: A Metal-Based Biological Strategy for Hard Flexible Coatings. *Science* **2010**, *328* (5975), 216–220. https://doi.org/10.1126/science.1181044.

(6) Lichtenegger, H. C.; Schöberl, T.; Ruokolainen, J. T.; Cross, J. O.; Heald, S. M.; Birkedal, H.; Waite, J. H.; Stucky, G. D. Zinc and Mechanical Prowess in the Jaws of Nereis, a Marine Worm. *Proc. Natl. Acad. Sci.* **2003**, *100* (16), 9144–9149. https://doi.org/10.1073/pnas.1632658100.

(7) Kim, H.; Lee, J.; Hong, Y.; Lim, C.; Lee, D. W.; Oh, D. X.; Waite, J. H.; Hwang, D. S. Essential Role of Thiols in Maintaining Stable Catecholato-Iron Complexes in Condensed Materials. *Chem. Mater.* **2022**, *34* (11), 5074–5083. https://doi.org/10.1021/acs.chemmater.2c00406.

(8) Joester, D.; Brooker, L. R. The Chiton Radula: A Model System for Versatile Use of Iron Oxides. In *Iron Oxides*; John Wiley & Sons, Ltd, 2016; pp 177–206. https://doi.org/10.1002/9783527691395.ch8.

(9) Stegbauer, L.; Smeets, P. J. M.; Free, R.; Wallace, S. G.; Hersam, M. C.; Alp, E. E.; Joester, D. Persistent Polyamorphism in the Chiton Tooth: From a New Biomineral to Inks for Additive Manufacturing. *Proc. Natl. Acad. Sci.* **2021**, *118* (23), e2020160118. https://doi.org/10.1073/pnas.2020160118.

(10) Keckes, J.; Burgert, I.; Frühmann, K.; Müller, M.; Kölln, K.; Hamilton, M.; Burghammer, M.; Roth, S. V.; Stanzl-Tschegg, S.; Fratzl, P. Cell-Wall Recovery after Irreversible Deformation of Wood. *Nat. Mater.* **2003**, *2* (12), 810–813. https://doi.org/10.1038/nmat1019.

(11) Sophia Fox, A. J.; Bedi, A.; Rodeo, S. A. The Basic Science of Articular Cartilage: Structure, Composition, and Function. *Sports Health* **2009**, *1* (6), 461–468. https://doi.org/10.1177/1941738109350438.

(12) Connizzo, B. K.; Yannascoli, S. M.; Soslowsky, L. J. Structure–Function Relationships of Postnatal Tendon Development: A Parallel to Healing. *Matrix Biol.* **2013**, *32* (2), 106–116. https://doi.org/10.1016/j.matbio.2013.01.007.

(13) Thurmond, F.; Trotter, J. Morphology and Biomechanics of the Microfibrillar Network of Sea Cucumber Dermis. *J. Exp. Biol.* **1996**, *199* (8), 1817–1828. https://doi.org/10.1242/jeb.199.8.1817.

(14) Gent, A. N.; Tobias, R. H. Threshold Tear Strength of Elastomers. *J. Polym. Sci. Polym. Phys. Ed.* **1982**, *20* (11), 2051–2058. https://doi.org/10.1002/pol.1982.180201107.

(15) Akagi, Y.; Sakurai, H.; Gong, J. P.; Chung, U.; Sakai, T. Fracture Energy of Polymer Gels with Controlled Network Structures. *J. Chem. Phys.* **2013**, *139* (14), 144905. https://doi.org/10.1063/1.4823834.

(16) Hamed, G. R. Reinforcement of Rubber. *Rubber Chem. Technol.* **2000**, *73* (3), 524–533. https://doi.org/10.5254/1.3547603.

(17) Saunders, J. H. The Relations between Polymer Structure and Properties in Urethans. *Rubber Chem. Technol.* **1960**, *33* (5), 1259–1292. https://doi.org/10.5254/1.3542246.

(18) Ducrot, E.; Chen, Y.; Bulters, M.; Sijbesma, R. P.; Creton, C. Toughening Elastomers with Sacrificial Bonds and Watching Them Break. *Science* **2014**, *344* (6180), 186–189. https://doi.org/10.1126/science.1248494.

(19) Nair, D. P.; Cramer, N. B.; McBride, M. K.; Gaipa, J. C.; Shandas, R.; Bowman, C. N. Enhanced Two-Stage Reactive Polymer Network Forming Systems. *Polymer* **2012**, *53* (12), 2429–2434. https://doi.org/10.1016/j.polymer.2012.04.007.

(20) Oku, T.; Furusho, Y.; Takata, T. A Concept for Recyclable Cross-Linked Polymers: Topologically Networked Polyrotaxane Capable of Undergoing Reversible Assembly and Disassembly. *Angew. Chem. Int. Ed.* **2004**, *43* (8), 966–969. https://doi.org/10.1002/anie.200353046.

(21) Liu, J.; Tan, C. S. Y.; Yu, Z.; Li, N.; Abell, C.; Scherman, O. A. Tough Supramolecular Polymer Networks with Extreme Stretchability and Fast Room-Temperature Self-Healing. *Adv. Mater.* **2017**, *29* (22), 1605325. https://doi.org/10.1002/adma.201605325.

(22) Wu, J.; Cai, L.-H.; Weitz, D. A. Tough Self-Healing Elastomers by Molecular Enforced Integration of Covalent and Reversible Networks. *Adv. Mater.* **2017**, *29* (38), 1702616. https://doi.org/10.1002/adma.201702616.

(23) Khare, E.; Holten-Andersen, N.; Buehler, M. J. Transition-Metal Coordinate Bonds for Bioinspired Macromolecules with Tunable Mechanical Properties. *Nat. Rev. Mater.* **2021**, *6* (5), 421–436. https://doi.org/10.1038/s41578-020-00270-z.

(24) Webber, M. J.; Tibbitt, M. W. Dynamic and Reconfigurable Materials from Reversible Network Interactions. *Nat. Rev. Mater.* **2022**, *7* (7), 541–556. https://doi.org/10.1038/s41578-021-00412-x.

(25) Jones, S. D.; Schauser, N. S.; Fredrickson, G. H.; Segalman, R. A. The Role of Polymer-Ion Interaction Strength on the Viscoelasticity and Conductivity of Solvent-Free Polymer Electrolytes. *Macromolecules* **2020**, *53* (23), 10574–10581. https://doi.org/10.1021/acs.macromol.0c02233.

(26) Shi, L.; Ding, P.; Wang, Y.; Zhang, Y.; Ossipov, D.; Hilborn, J. Self-Healing Polymeric Hydrogel Formed by Metal–Ligand Coordination Assembly: Design, Fabrication, and Biomedical Applications. *Macromol. Rapid Commun.* **2019**, *40* (7), 1800837. https://doi.org/10.1002/marc.201800837.

(27) Pollino, J. M.; Weck, M. Non-Covalent Side-Chain Polymers: Design Principles, Functionalization Strategies, and Perspectives. *Chem. Soc. Rev.* **2005**, *34* (3), 193–207. https://doi.org/10.1039/B311285N.

(28) Menyo, M. S.; Hawker, C. J.; Waite, J. H. Versatile Tuning of Supramolecular Hydrogels through Metal Complexation of Oxidation-Resistant Catechol-Inspired Ligands. *Soft Matter* **2013**, *9* (43), 10314–10323. https://doi.org/10.1039/c3sm51824h.

(29) Grindy, S. C.; Learsch, R.; Mozhdehi, D.; Cheng, J.; Barrett, D. G.; Guan, Z.; Messersmith, P. B.; Holten-Andersen, N. Control of Hierarchical Polymer Mechanics with Bioinspired Metal-Coordination Dynamics. *Nat. Mater.* **2015**, *14* (12), 1210–1216. https://doi.org/10.1038/nmat4401.

(30) Sacligil, I.; Barney, C. W.; Crosby, A. J.; Tew, G. N. Bond Strength Regime Dictates Stress Relaxation Behavior. *Soft Matter* **2022**, *18* (26), 4937–4943. https://doi.org/10.1039/D2SM00499B.

(31) Holten-Andersen, N.; Harrington, M. J.; Birkedal, H.; Lee, B. P.; Messersmith, P. B.; Lee, K. Y. C.; Waite, J. H. pH-Induced Metal-Ligand Cross-Links Inspired by Mussel Yield Self-Healing Polymer Networks with near-Covalent Elastic Moduli. *Proc. Natl. Acad. Sci. U. S. A.* **2011**, *108* (7), 2651–2655. https://doi.org/10.1073/pnas.1015862108.

(32) Barrett, D. G.; Fullenkamp, D. E.; He, L.; Holten-Andersen, N.; Lee, K. Y. C.; Messersmith, P. B. pH-Based Regulation of Hydrogel Mechanical Properties Through Mussel-Inspired Chemistry and Processing. *Adv. Funct. Mater.* **2013**, *23* (9), 1111–1119. https://doi.org/10.1002/adfm.201201922.

(33) Kim, S.; Peterson, A. M.; Holten-Andersen, N. Enhanced Water Retention Maintains Energy Dissipation in Dehydrated Metal-Coordinate Polymer Networks: Another Role for

Fe-Catechol Cross-Links? *Chem. Mater.* **2018**, *30* (11), 3648–3655. https://doi.org/10.1021/acs.chemmater.7b05246.

(34) Zhang, J.; Su, C.-Y. Metal-Organic Gels: From Discrete Metallogelators to Coordination Polymers. *Coord. Chem. Rev.* **2013**, *257* (7), 1373–1408. https://doi.org/10.1016/j.ccr.2013.01.005.

(35) Saiz-Poseu, J.; Mancebo-Aracil, J.; Nador, F.; Busqué, F.; Ruiz-Molina, D. The Chemistry behind Catechol-Based Adhesion. *Angew. Chem. Int. Ed.* **2019**, *58* (3), 696–714. https://doi.org/10.1002/anie.201801063.

(36) Cristiani, T. R.; Filippidi, E.; Behrens, R. L.; Valentine, M. T.; Eisenbach, C. D. Tailoring the Toughness of Elastomers by Incorporating Ionic Cross-Linking. *Macromolecules* **2020**, *53* (10), 4099–4109. https://doi.org/10.1021/acs.macromol.0c00500.

(37) Filippidi, E.; Cristiani, T. R.; Eisenbach, C. D.; Herbert Waite, J.; Israelachvili, J. N.; Kollbe Ahn, B.; Valentine, M. T. Toughening Elastomers Using Mussel-Inspired Iron-Catechol Complexes. *Science* **2017**, *358* (6362), 502–505. https://doi.org/10.1126/science.aao0350.

(38) Takeshima, H.; Satoh, K.; Kamigaito, M. Bio-Based Functional Styrene Monomers Derived from Naturally Occurring Ferulic Acid for Poly(Vinylcatechol) and Poly(Vinylguaiacol) via Controlled Radical Polymerization. *Macromolecules* **2017**, *50* (11), 4206–4216. https://doi.org/10.1021/acs.macromol.7b00970.

(39) Heo, J.; Kang, T.; Jang, S. G.; Hwang, D. S.; Spruell, J. M.; Killops, K. L.; Waite, J. H.; Hawker, C. J. Improved Performance of Protected Catecholic Polysiloxanes for Bioinspired Wet Adhesion to Surface Oxides. *J. Am. Chem. Soc.* **2012**, *134* (49), 20139–20145. https://doi.org/10.1021/ja309044z.

(39) Yin, Q.; Wang, L.; Jiang, J.; Dai, C.; Weng, G.; He, J. Three-Dimensional Shape Transformation of Eu3+-Containing Polymer Films through Modulating Dynamic Eu3+-Iminodiacetate Coordination. *Chem. Mater.* **2022**, *34* (5), 2176–2186. https://doi.org/10.1021/acs.chemmater.1c03722.

(41) Lee, B. P.; Konst, S. Novel Hydrogel Actuator Inspired by Reversible Mussel Adhesive Protein Chemistry. *Adv. Mater.* **2014**, *26* (21), 3415–3419. https://doi.org/10.1002/adma.201306137.

(42) Spaans, S.; Fransen, P.-P. K. H.; Schotman, M. J. G.; van der Wulp, R.; Lafleur, R. P. M.; Kluijtmans, S. G. J. M.; Dankers, P. Y. W. Supramolecular Modification of a Sequence-Controlled Collagen-Mimicking Polymer. *Biomacromolecules* **2019**, *20* (6), 2360–2371. https://doi.org/10.1021/acs.biomac.9b00353.

(43) Lee, K.; Shang, Y.; Bobrin, V. A.; Kuchel, R.; Kundu, D.; Corrigan, N.; Boyer, C. 3D Printing Nanostructured Solid Polymer Electrolytes with High Modulus and

Conductivity. *Adv. Mater.* **2022**, *34* (42), 2204816. https://doi.org/10.1002/adma.202204816.

(44) Moon, J. D.; Sujanani, R.; Geng, Z.; Freeman, B. D.; Segalman, R. A.; Hawker, C. J. Versatile Synthetic Platform for Polymer Membrane Libraries Using Functional Networks. *Macromolecules* **2021**, *54* (2), 866–873. https://doi.org/10.1021/acs.macromol.0c02414.

(44) Grignon, E.; An, S. Y.; Battaglia, A. M.; Seferos, D. S. Catechol Homopolymers and Networks through Postpolymerization Modification. *Macromolecules* **2022**, *55* (22), 10167–10175. https://doi.org/10.1021/acs.macromol.2c01513.

(46) Chan, J. M. W.; Tan, J. P. K.; Engler, A. C.; Ke, X.; Gao, S.; Yang, C.; Sardon, H.; Yang, Y. Y.; Hedrick, J. L. Organocatalytic Anticancer Drug Loading of Degradable Polymeric Mixed Micelles via a Biomimetic Mechanism. *Macromolecules* **2016**, *49* (6), 2013–2021. https://doi.org/10.1021/acs.macromol.5b02784.

(47) Yang, J.; Cohen Stuart, M. A.; Kamperman, M. Jack of All Trades: Versatile Catechol Crosslinking Mechanisms. *Chem. Soc. Rev.* **2014**, *43* (24), 8271–8298. https://doi.org/10.1039/c4cs00185k.

(48) Yu, M.; Deming, T. J. Synthetic Polypeptide Mimics of Marine Adhesives. *Macromolecules* **1998**, *31* (15), 4739–4745. https://doi.org/10.1021/ma980268z.

(49) Bijlsma, J.; de Bruijn, W. J. C.; Hageman, J. A.; Goos, P.; Velikov, K. P.; Vincken, J.-P. Revealing the Main Factors and Two-Way Interactions Contributing to Food Discolouration Caused by Iron-Catechol Complexation. *Sci. Rep.* **2020**, *10* (1), 8288. https://doi.org/10.1038/s41598-020-65171-1.

(50) Mellican, R. I.; Li, J.; Mehansho, H.; Nielsen, S. S. The Role of Iron and the Factors Affecting Off-Color Development of Polyphenols. *J. Agric. Food Chem.* **2003**, *51* (8), 2304–2316. https://doi.org/10.1021/jf020681c.

(51) Mora-Barrantes, I.; Malmierca, M. A.; Valentin, J. L.; Rodriguez, A.; Ibarra, L. Effect of Covalent Cross-Links on the Network Structure of Thermo-Reversible Ionic Elastomers. *Soft Matter* **2012**, *8* (19), 5201–5213. https://doi.org/10.1039/c2sm06975j.

(52) Eisenberg, A.; Hird, B.; Moore, R. B. A New Multiplet-Cluster Model for the Morphology of Random Ionomers. *Macromolecules* **1990**, *23* (18), 4098–4107. https://doi.org/10.1021/ma00220a012.

(53) De Molina, P. M.; Lad, S.; Helgeson, M. E. Heterogeneity and Its Influence on the Properties of Difunctional Poly(Ethylene Glycol) Hydrogels: Structure and Mechanics. *Macromolecules* **2015**, *48* (15), 5402–5411. https://doi.org/10.1021/acs.macromol.5b01115.

(54) Beija, M.; Li, Y.; Lowe, A. B.; Davis, T. P.; Boyer, C. Factors Influencing the Synthesis and the Post-Modification of PEGylated Pentafluorophenyl Acrylate Containing

Copolymers. *Eur. Polym. J.* **2013**, *49* (10), 3060–3071. https://doi.org/10.1016/j.eurpolymj.2013.05.003.

(55) Flory, P. J. Network Structure and the Elastic Properties of Vulcanized Rubber. *Chem. Rev.* **1944**, *35* (1), 51–75. https://doi.org/10.1021/cr60110a002.

(56) Geise, G. M.; Paul, D. R.; Freeman, B. D. Fundamental Water and Salt Transport Properties of Polymeric Materials. *Prog. Polym. Sci.* **2014**, *39* (1), 1–42. https://doi.org/10.1016/j.progpolymsci.2013.07.001.

(57) Jang, E.-S.; Kamcev, J.; Kobayashi, K.; Yan, N.; Sujanani, R.; Dilenschneider, T. J.; Park, H. B.; Paul, D. R.; Freeman, B. D. Influence of Water Content on Alkali Metal Chloride Transport in Cross-Linked Poly(Ethylene Glycol) Diacrylate.2. Ion Diffusion. *Polymer* **2020**, *192*, 122316. https://doi.org/10.1016/j.polymer.2020.122316.

(58) Savoie, B. M.; Webb, M. A.; Miller, T. F. Enhancing Cation Diffusion and Suppressing Anion Diffusion via Lewis-Acidic Polymer Electrolytes. *J. Phys. Chem. Lett.* **2017**, *8* (3), 641–646. https://doi.org/10.1021/acs.jpclett.6b02662.

(59) Krajewska, B. Diffusion of Metal Ions through Gel Chitosan Membranes. *React. Funct. Polym.* **2001**, *47* (1), 37–47. https://doi.org/10.1016/S1381-5148(00)00068-7.

(60) Schauser, N. S.; Sanoja, G. E.; Bartels, J. M.; Jain, S. K.; Hu, J. G.; Han, S.; Walker, L. M.; Helgeson, M. E.; Seshadri, R.; Segalman, R. A. Decoupling Bulk Mechanics and Mono- and Multivalent Ion Transport in Polymers Based on Metal–Ligand Coordination. *Chem. Mater.* **2018**, *30* (16), 5759–5769. https://doi.org/10.1021/acs.chemmater.8b02633.

(61) Sanoja, G. E.; Schauser, N. S.; Bartels, J. M.; Evans, C. M.; Helgeson, M. E.; Seshadri, R.; Segalman, R. A. Ion Transport in Dynamic Polymer Networks Based on Metal–Ligand Coordination: Effect of Cross-Linker Concentration. *Macromolecules* **2018**, *51* (5), 2017–2026. https://doi.org/10.1021/acs.macromol.7b02141.

(62) Bracher, P. J.; Gupta, M.; Mack, E. T.; Whitesides, G. M. Heterogeneous Films of Ionotropic Hydrogels Fabricated from Delivery Templates of Patterned Paper. *ACS Appl. Mater. Interfaces* **2009**, *1* (8), 1807–1812. https://doi.org/10.1021/am900340m.

(63) Bracher, P. J.; Gupta, M.; Whitesides, G. M. Shaped Films of Ionotropic Hydrogels Fabricated Using Templates of Patterned Paper. *Adv. Mater.* **2009**, *21* (4), 445–450. https://doi.org/10.1002/adma.200801186.

(64) Gockowski, L. F.; Dolinski, N. D.; Chavez, R.; Cohen, N.; Eisenreich, F.; Hecht, S.; McMeeking, R. M.; Hawker, C. J.; Valentine, M. T. Engineering Crack Tortuosity in Printed Polymer-Polymer Composites through Ordered Pores. *Mater. Horiz.* **2020**, *7* (7), 1854–1860. https://doi.org/10.1039/d0mh00331j.

(65) Shin, E.; Ju, S. W.; An, L.; Ahn, E.; Ahn, J.-S.; Kim, B.-S.; Ahn, B. K. Bioinspired Catecholic Primers for Rigid and Ductile Dental Resin Composites. *ACS Appl. Mater. Interfaces* **2018**, *10* (2), 1520–1527. https://doi.org/10.1021/acsami.7b14679.

Chapter 3. Bioinspired Metal-Ligand Networks: Facile Preparation of Hydroxypyridinone (HOPO) Functionalized Materials with Tunable and Patternable Properties

Text and Figures reprinted and adapted from Shannon, D., et al. (2024). Bioinspired Metal-Ligand Networks: Facile Preparation of Hydroxypyridinone (HOPO) Functionalized Materials with Tunable and Patternable Properties. doi.org/10.XXXX/XXXX *in preparation.*

3.1 Abstract

Bioinspired hydroxypyridinone (HOPO) functionalized materials have shown remarkable capabilities for chelating a wide array of metal ions, creating systems with diverse physical properties. In the present study we report a facile, one pot synthesis of a HOPO ligand and simple, scalable installation into active ester network materials. This modular network approach allows for preparation of HOPO containing networks amenable to chelating a range of metals ions, such as transition metals (Fe^{3+}) and lanthanides (Ho^{3+}, Tb^{3+}), to modulate mechanical, magnetic, and fluorescent properties. Moreover, networks with tailored, heterogeneous properties can be prepared through localization and patterning of metal center absorption via masking techniques, creating distinctly soft, hard, magnetic, and fluorescent domains.

3.2 Introduction

Biomimetic and bioinspired polymer network systems display a wide range of remarkable properties with tailored mechanical responses[1–3], chemical functionalities[4], and

stimuli responsive behavior[5]. Synthetic design of such materials has leveraged, mimicked, and expanded upon natural motifs, and represents an enticing area of research with a range of strategies for network formation and property modulation[1–3,5]. While various approaches have had demonstrated success in preparing bioinspired materials with controlled mechanical responses[6–10], there is great interest in developing resilient, biomimetic materials with added functionalities and stimuli responsive characteristics[5,11,12]. Particularly desirable are properties such as fluorescence and magnetic responsiveness, as they offer rapid responses with facile control of external stimuli[13]. While a myriad of strategies exists to target such properties, implementing modular design strategies at the chemical level to achieve these materials properties can prove challenging.

In pursuit of functional, mechanically resilient network materials, various synthetic strategies have been employed to create materials with desirable properties. A wide array of bioinspired approaches exist, with examples ranging from embedding of (nano)particulate fillers[12–14], to property installation *via* metal-ligand chelation[3,15–19]. Among these, metal-ligand networks present a facile pathway to access such desired, engineered network functionalities and have demonstrated remarkable tunability for a range of applications through selection of the metal-ligand pair[3,20]. Moreover, leveraging metal chelation enables the ability to install varied properties as a function of the metal ion into the same bioinspired polymer network scaffold, and selectively localize these properties via soft lithography techniques[16,18]. In particular, transition metal and lanthanide ions are of interest for their ability to form mechanically robust crosslinking sites, as well as for their unique magnetic and optical properties[3,16,21].

Many bioinspired, metal-ligand polymer networks take inspiration from the chemical structures of well-studied natural systems which leverage transition metal coordination[3], including marine muscles[22], invertebrate jaws[23–25], tunicates[26], and others[27–29]; and more recent developments which have highlighted the potential of lanthanide use in bacteria[30–32]. While many bioinspired motifs are available, mimosine mimetic functionalities leveraging the hydroxypyridinone (HOPO) motif have emerged as a useful series of chelating ligands[33–36], mimicking the underlying motif used in mimosoid plants for ion transport[37,38]. These ligands offer similarly attractive features to siderophore-mimetic catechol ligands, but with increased resistance to oxidation, lower pka, and wide chelation scope for capture of both transition metals and rare earth elements[33,36,39–42]. As such, HOPO containing small molecules have seen wide adoption in metal chelating drugs such as deferiprone and ligand scaffolds for medical and imaging applications[33,43–45]. Despite their utility, minimal literature[42,46,47] has explored these motifs for metal-ligand polymer networks, likely owing to the multi-step ligand synthesis[33], and comparable materials represent an understudied segment of the polymer network field with limited visibility.

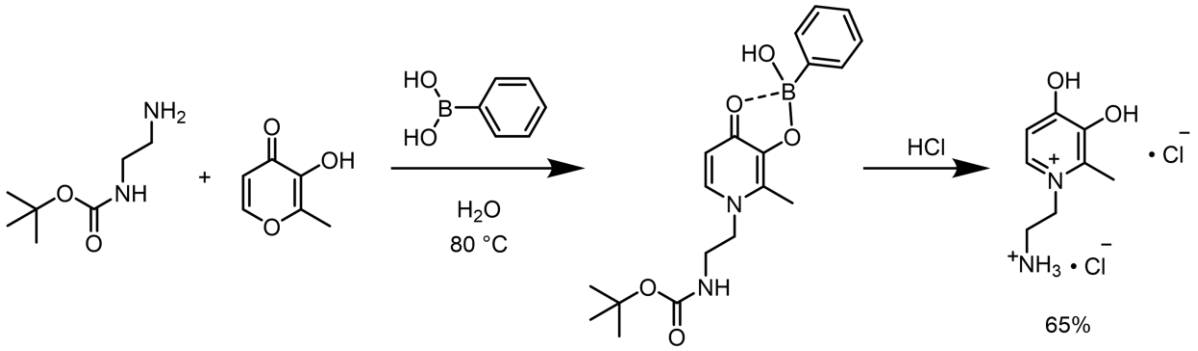
In the present study we demonstrate an effective, scalable synthetic method to prepare hydroxypyridinone functionalized, patternable network materials with an array of tunable mechanical, magnetic, and fluorescent properties through selection of metal center identity. Using recently developed boronic acid chemistry[48] from Ke, Zhang, and coworkers, we adopt their strategy to design a HOPO ligand compatible with well-studied active ester network materials and compare to comparable catechol functionalized systems[18,49]. Prepared HOPO networks enable chelation of classical transition metals such as iron for mechanical reinforcement[42], as well as chelation of lanthanides to prepare samples with inherent

paramagnetic and UV-induced fluorescence through holmium and terbium chelation[21,33,39,50,51]. Moreover, leveraging prior patterning methods[16,18], we demonstrate the ability to spatially control metal center incorporation, allowing for the preparation of heterogenous, composite like materials with localized mechanical, magnetic, and fluorescent behavior.

3.3 Results and Discussion

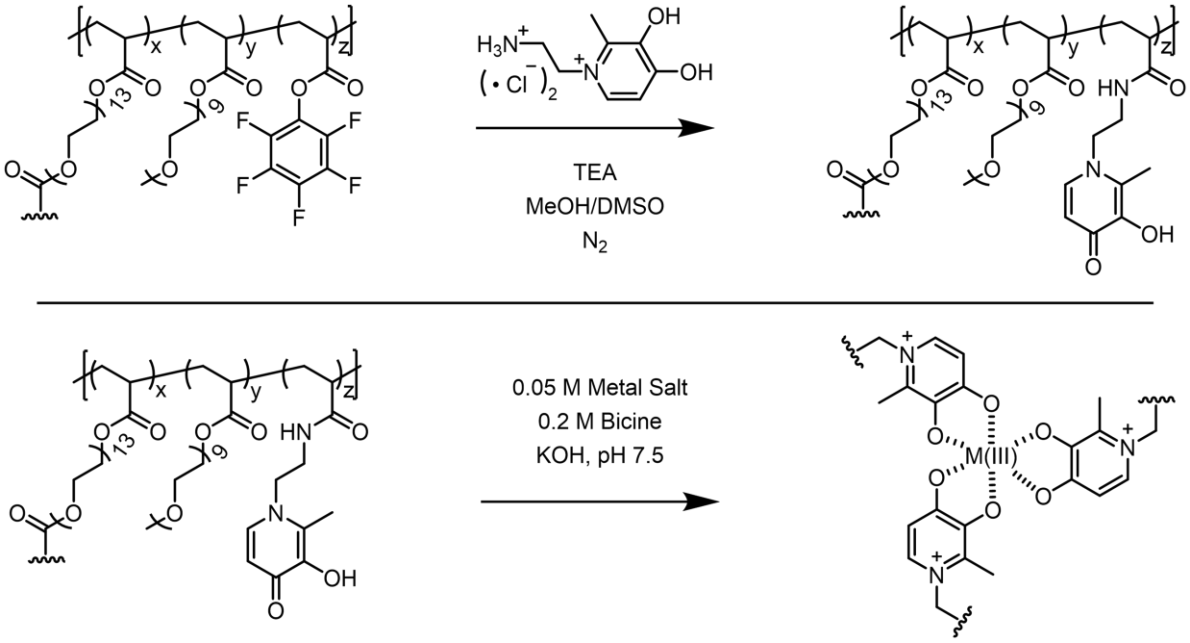
A recent method of hydroxypyridinone synthesis was leveraged to easily prepare an active ester compatible HOPO ligand on a multigram scale in a one pot approach. Classic preparation methods[33,42,46] for this and similar moieties require hazardous reagents and crucially require a multistep synthesis with protection and deprotection of the starting maltol, resulting in reduced yields of the final product. To circumvent these limitations in ligand preparation, we leveraged the method developed by Ke, Zhang, and coworkers[48] to prepare our HOPO ligand from simple starting materials with water as the solvent, as seen in **Scheme 3.1**. This facile approach allows for gram scale preparation of materials from cheap reagents and enabled large scale preparation of network materials. In brief, maltol was reacted with N-boc-ethylene diamine in the presence of phenylboronic acid to create the protected hydroxypyridinone intermediate. The product as a viscous oil was deprotected in-situ with concentrated hydrochloric acid and purified *via* facile recrystallization. Ligand final product was characterized by a range of spectroscopic techniques in good agreement with literature[52], and detailed synthetic methods and characterization for the HOPO ligand are included in **Appendix B**.

Scheme 3.1: Synthesis of amine terminated HOPO ligand.



Network synthesis was conducted following approaches detailed previously[18,49] to prepare materials containing an active ester site and additional details are listed in **Appendix B**. In brief, networks were prepared from a solvent free monomer mixture containing pentafluorophenyl acrylate (PFPA, active ester site), a PEG-diacrylate (PEGDA, M_n 700, crosslinker), a PEG-acrylate (PEGMEA, M_n 480, diluent monomer), and a small amount 2,2-dimethoxy-2-phenylacetophenone (DMPA, 0.1 wt.%) as a photoinitiator. The resin mixture was dispensed between quartz plates with film thickness controlled by spacer gauges and cured to form a free-standing network via UV irradiation for 2 minutes (365 nm, 3 mW/cm^2).

Scheme 3.2: (Top) Installation of HOPO ligand into PFPA networks and (Bottom) complexation with metal salts in aqueous media. Complexation was conducted with $Fe(NO_3)_3$, $Ho(NO_3)_3$, $TbCl_3$.



To better contextualize the properties of the final HOPO functionalized networks, PFPA networks were then substituted with either the synthesized HOPO ligand (**Scheme 3.2** and **Appendix B**) or commercially available dopamine (2-(3,4-dihydroxyphenyl)ethylamine hydrochloride salt) following prior procedures[18] (**Appendix B**). Moreover, for both catechol and HOPO functionalized networks, metal ions were incorporated according to **Scheme 3.2** *via* washing procedures developed previously[17,18,53] from bicine buffered solutions at pH 7.5. Iron was selected as a classical example for mechanical reinforcement of HOPO networks[42], and lanthanide ions were selected for their magnetic (Ho^{3+} and Tb^{3+}) and fluorescent (Tb^{3+}) properties in addition to mechanical reinforcement. Following metal center installation, samples were thoroughly dialyzed in deionized water to remove residual salts and buffer components, followed by gentle deswelling using a series of solvent gradients with decreasing

polarity. Metal ion solution preparations, detailed metal installation methods, and representative solvent gradients are described in **Appendix B**.

Effective preparation of active ester networks and installation of ligands into the network was validated *via* FTIR spectroscopy to confirm substitution of PFPA sites. Polyacrylate networks containing PFPA moieties were prepared, and diagnostic peaks were identified in accordance with prior literature[18,49]. Results in **Figure 3.1** demonstrate the presence of key diagnostic peaks from the pentafluorophenyl group at 985, 1520, and 1780 cm^{-1} in the precursor networks and disappearance of these peaks upon substitution with an amine terminated ligand. For both catechol and HOPO functionalized networks, an amide stretching band at ~1660 cm^{-1} is observed after ligand installation.

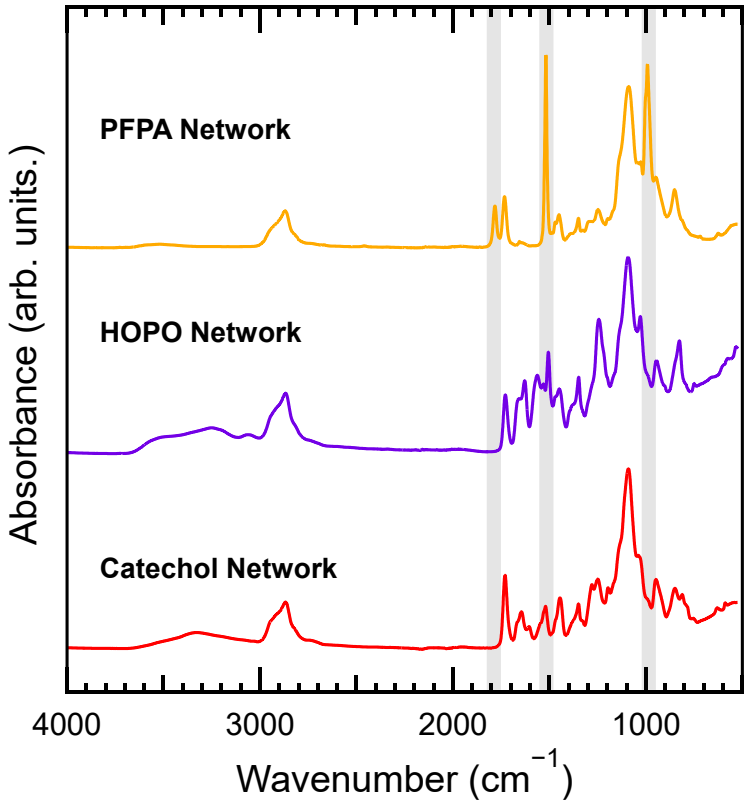


Figure 3.1: FTIR-attenuated total reflection (ATR) of random copolymer networks. From top to bottom: a 3/39/58 mol% PEGDA/PEGMEA/ PFPA network before substitution (yellow), a PFPA containing network after substitution with hydroxypyridinone ligand (purple), a PFPA containing network after substitution with dopamine (red). Diagnostic peaks from the PFPA moieties (gray highlighted peaks) at 985, 1520, and 1780 cm^{-1} disappear after ligand installation with amide stretching bands appearing at ~1660 cm^{-1}.

To highlight the stability of HOPO functionalized networks relative to their classical catechol counterparts, a set of pH mediated ageing experiments were conducted. Catechol containing materials demonstrate limited stability, particularly under basic, oxygenated conditions, with known pH-dependent oxidation and autoxidation leading to crosslinking between neighboring catechol moities[10,54,55]. Conversely, HOPO containing materials demonstrate improved stability under these conditions, in part due to their changes in electron density in the aromatic ring, in line with prior literature[33,42,46,56]. In the present experiment, as

visually demonstrated in **Figure 3.2,** punch samples of HOPO and catechol functionalized networks were transferred from acidic storage solutions (1 mM HCl) to basic, aqueous solutions buffered at pH 9 (KOH and 0.2M bicine) for 24 hours, imaged, and then returned to acidic solution. Catechol samples were noted to display characteristic color changes of quinone formation and oxidation[10,54,56], while no appreciable changes were observed for HOPO functionalized materials, in line with prior studies[42,56]. Visual changes in samples after base mediated oxidation were corroborated by additional FTIR measurement at 24 and 72 hours of base exposure, and FTIR traces were compared to those of control samples oxidized with sodium periodate ($NaIO_4$) (**Figure B.2, Appendix B**). Base treated catechol samples showed changes in FTIR trace morphology progressing towards and consistent with oxidation of catechols as observed in periodate controls[57–59], while negligible changes in FTIR traces were observed for HOPO samples. Moreover, FTIR measurements of untreated and base treated HOPO films are inconsistent with periodate oxidized HOPO samples, further indicating minimal oxidation of the HOPO moiety and improved stability of the motif. Results highlight the utility of the more resilient HOPO motif over traditional siderophore mimetic catechol moieties.

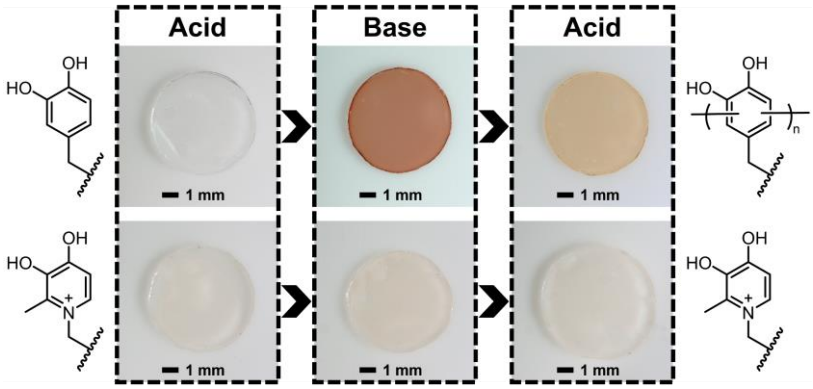


Figure 3.2: A visual demonstration of sample oxidative stability for catechol (top row) and HOPO (bottom row) functionalized networks. From left to right, samples before, during, and after 24 hours of aging in basic, aqueous media. Samples stored in 1 mM HCl solutions (left column) were transferred to KOH solutions buffered with bicine (0.2 M) at pH 9 for 24 hours (middle column), followed by dialysis and equilibration in 1 mM HCl storage solution (right column).

Networks were further characterized after metal center installation and demonstrated expected metal chelation *via* Raman spectroscopy (**Figure 3.3**). Prior literature[18,22] has demonstrated the utility of Raman spectroscopy for confirming the presence of metal-ligand chelation in polymer networks, and comparable approaches were leveraged to elucidate the nature of HOPO-metal center crosslinks. Crucially, as seen in **Figure 3.3**, diagnostic peaks are present for both the ligand's vibrations in the metal free samples (686 cm^{-1}) which are dwarfed by appearance of a diagnostic peak after iron chelation (~570 cm^{-1}) in agreement with literature reports for iron-hydroxypyridinone complexes and confirm the presence of Fe-HOPO crosslinks[60]. Similarly, Raman spectroscopy provides indication of metal chelation for HOPO-lanthanide complexes. While literature reports of Raman spectra for this metal-ligand complex are sparse, comparable vibrational spectroscopy studies have been conducted with tropolone-lanthanide and tropolone-transition metal complexes which demonstrate similar diagnostic peak shifts from the metal free to metal complexed systems[61–63]. Crucially, as

observed in literature for lanthanide complexes[61], we observe a diagnostic peak shift from the metal free ligand (686 cm^{-1}) to the metal complexed sample (approx. 705 cm^{-1}), attributed to changes in ring and M-O vibrational modes upon chelation as seen in the HOPO-Ho^{3+} sample (**Figure 3.3** and **Appendix B** for additional metal salts).

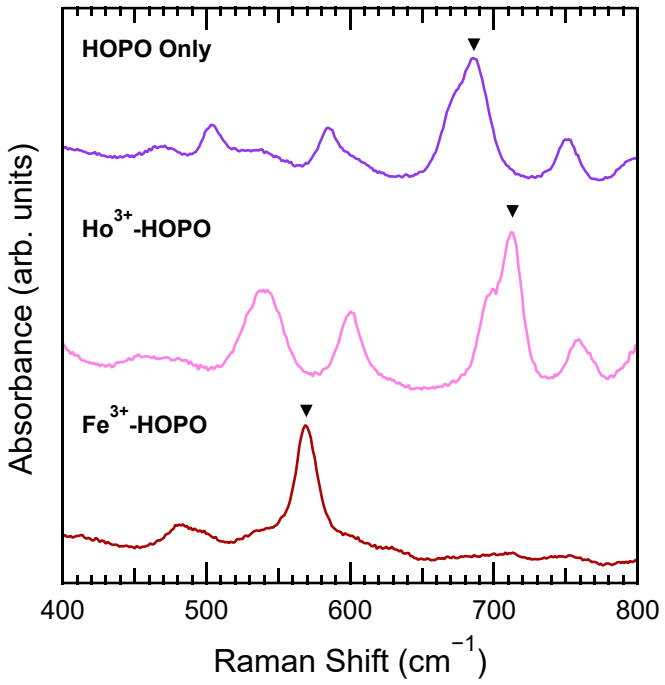


Figure 3.3: Raman spectra of HOPO functionalized networks with and without metal ions. From top to bottom: a 3/39/58 mol% PEGDA/PEGMEA/PFPA network after HOPO substitution (purple), a HOPO containing network of the same composition after complexation with Ho^{3+} (pink), and a HOPO network of equivalent composition after complexation with Fe^{3+} (red).

To build desired materials properties into these modular networks, an array of metal ions was selected to complex with mimosine inspired ligands for development of materials with tailored mechanical, magnetic, and fluorescent properties. Present results demonstrate an approach to modulate these properties as a function of metal center and ligand selection, and illustrate the potential of this synthetic approach for future systems such as magnetic

tweezers[64] and soft robotic applications[16,65–67]. Moreover, to further demonstrate the applications of this synthetic system, materials were developed with patterned metal center incorporation to localize mechanical, magnetic, and fluorescent response using methods previously delineated in the literature[16,18].

Mechanical behavior of polymer networks was examined in three-point bend testing, and results demonstrated high elastic moduli after metal center incorporation with noticeable property modulation based on selection of ligand and metal center. Iron-catechol data was adapted from our prior publication[18], and crucially, catecholate and HOPO functionalized materials both demonstrate high elastic moduli after complexation with iron ions, indicating formation of elastically effective metal-ligand crosslinks compared to their metal free base networks (elastic moduli of 3.1 MPa for catechol networks and 3.8 MPa for HOPO samples). However, the advantages of the HOPO network relative to classical catecholate materials are observed during complexation with lanthanide ions from aqueous media. Appreciable differences in elastic moduli were noted, with HOPO networks demonstrating high elastic moduli (~300 MPa) while catechol functionalized materials showed only moderate elastic moduli increases (~12 MPa) after attempted lanthanide complexation in aqueous media. At present these mechanical changes for catechol-lanthanide samples are predominantly attributed to oxidation of catechol residues[18,22] and some potentially weak capture of lanthanide ions by catechol moieties[68]. No diagnostic catechol-lanthanide peaks could be identified *via* Raman spectroscopy (**Appendix B**), but a paramagnetic moment was observed in magnetometry (*vide infra*) indicating the presence of trace paramagnetic Ho^{3+} ions. These mechanical differences fall in line with prior literature expectations, which elucidate the capabilities of HOPO ligands, and the limitations of catechol groups, for lanthanide capture

from aqueous media in mildly basic pH[33,68]. Present results in **Figure 3.4** demonstrate the mechanical reinforcement achieved with iron and holmium complexes in catechol and HOPO networks and additional mechanical testing data and methodology is included in **Appendix B.**

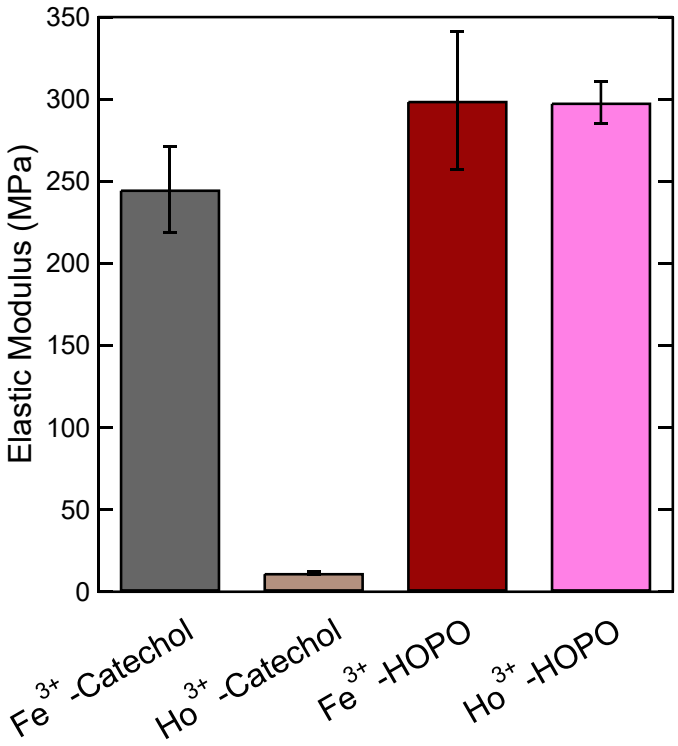


Figure 3.4: Elastic moduli, *E*, measured via 3-point beam bending of dry metal-ligand polymer networks. Error bars represent standard deviations from replicate measurements. Iron-catechol elastic moduli and standard deviation were taken from previous publication using the same preparation and network composition[18].

To further leverage the wide ion scope and potential properties of HOPO networks, magnetometry measurements were conducted to probe the strong paramagnetic response of the lanthanide-HOPO networks. Data for catechol and HOPO functionalized films after

complexation with holmium is presented in **Figure 3.5** and reveals clear differences in the magnetic response of each respective film. While both systems display a paramagnetic response, HOPO films show a nearly two-fold increase in magnetic moment per gram of material for the same applied field as catechol functionalized samples. These results are in line with expectations of improved stability of HOPO-lanthanide complexes relative to catecholate materials and correlate with present observations by Raman spectroscopy. This suggests and follows expectations of consequentially higher uptake of the metal center from the aqueous complexation solution by HOPO ligands than catechol ligands. While chelation of lanthanides by catechol functionalized networks was not observed *via* Raman spectroscopy, we anticipate small, trace amounts of lanthanide metal center may be retained within the network via interactions between catechol hydroxyls and lanthanide metal ions [68,69].

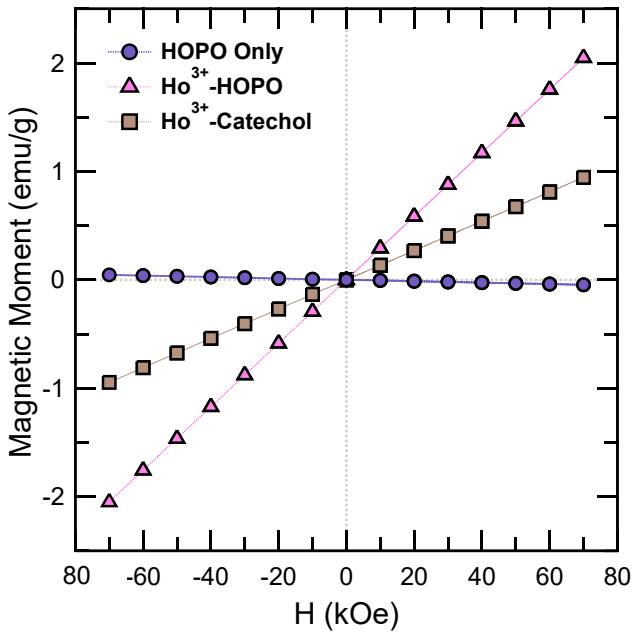


Figure 3.5: Magnetization curves (moment vs. applied field) of holmium complexed polymer networks substituted with either catechol (light brown squares) or HOPO (pink triangles) moieties. A metal free HOPO network (purple circles) is provided for comparison.

We further leverage these HOPO functionalized materials to prepare patterned samples with composite-like properties, allowing for spatial control of mechanical, magnetic, and fluorescent behaviors through selection of metal center identity. Leveraging prior approaches[18] and literature insight[16,70], we demonstrate the ability to incorporate various metal centers through selective surface exposure and soft lithography type techniques. Patterning approaches can be leveraged for incorporation of metal ions into neat, metal-free samples as well as for installation of metal ions into metal-containing samples *via* ion exchange. Approaches build on prior methods[18] for preparing samples with in single- or double-sided systems as seen in **Figure 3.6** to simultaneously incorporate more than one metal center. It should be noted that while a double-sided patterning *via* ion exchange is displayed, this approach is modular, and patterning can be done with single metal centers, directly into unfunctionalized HOPO networks as in **Figure 3.7**.

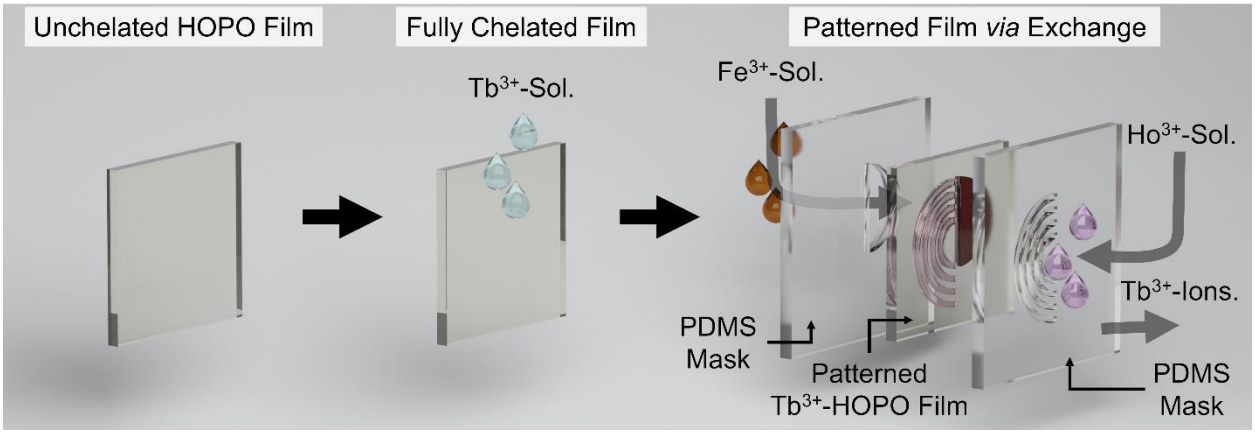


Figure 3.6: Selective patterning and installation of metal centers into HOPO functionalized networks *via* Tb^{3+} complexation and ion exchange using modular patterning approaches. (Left) An untreated HOPO network. (Middle) A fully complexed Tb^{3+}-HOPO network. (Right) Simultaneous surface patterning of Fe^{3+} and Ho^{3+} by exchange of Tb^{3+} metal centers.

To demonstrate these patterned properties, we can impart mechanical and magnetic heterogeneity through selective localization of metal centers such as iron (**Appendix B**) and holmium (**Figure 3.7**). Here in a simple demonstration, the metal-complexed region of the film (**Fig. 3.7a and 3.7b**) displays increased rigidity and resistance to bending in comparison to metal-free control samples (**Fig. 3.7c and 3.7b**). Furthermore, by selectively incorporating holmium into the network, we demonstrate the ability to locally control the films paramagnetic properties. As observed in **Figure 3.7d**, the metal-free control sample and metal-free regions of the patterned sample display negligible magnetic response to a benchtop magnet. Conversely, the holmium patterned region of the film displays a strong paramagnetic response and enables the entire patterned sample to be raised. Present results are encouraging and demonstrate an effective method to prepare materials with localized paramagnetic and mechanical responses. Moreover, synthetic approaches used in this study are compatible with a wide array of polyacrylate and related network chemistries and may enable development of novel materials for soft-robotics applications and magnetic tweezer systems[64–67].

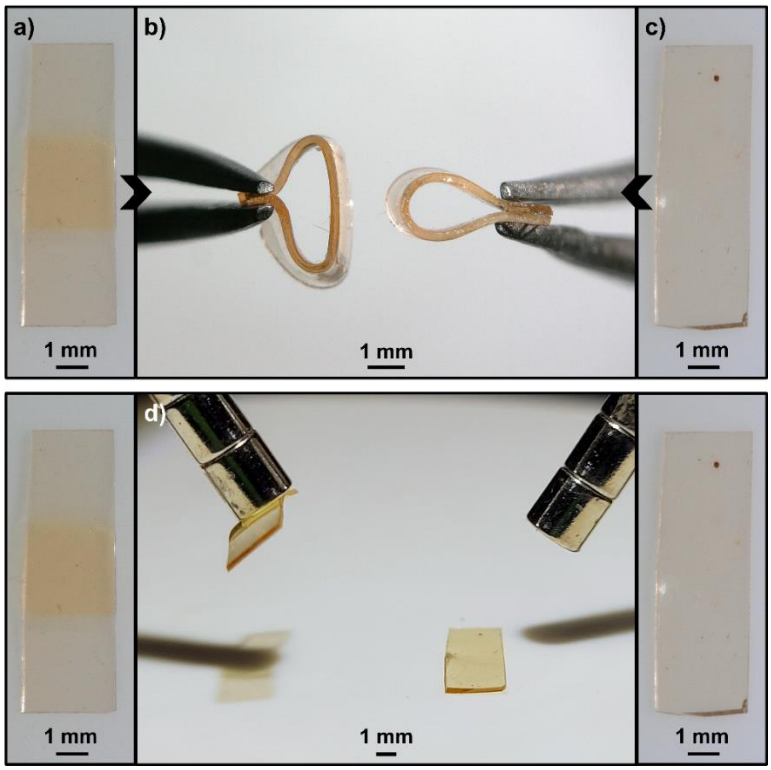


Figure 3.7: (a) Polymer film of 3/39/58 mol% PEGDA/PEGMEA/HOPO with a central section functionalized with Ho^{3+}-HOPO complexes. (b) Comparison of film mechanical behavior under bending between metal-patterned (left) and metal free (right). (c) Polymer film of 3/39/58 mol% PEGDA/PEGMEA/HOPO without any metal ions installed in the network. (d) Still image showing the HOPO-Ho^{3+} patterned film being lifted by a magnet with panels (a) and (c) pictured again for clarity.

We further develop this materials platform by designing patterned samples with localized fluorescence through chelation and exchange of terbium metal centers. Lanthanide metal ions offer many attractive properties even as chelated species including paramagnetism and UV induced fluorescence with large, diagnostic Stokes shifts[15,21,71]. By leveraging the similar chelation behavior of lanthanide ions[72,73] and strong binding affinities of hydroxypyridinone for iron ions[33], we demonstrate the ability to pattern the negative or "dark" image onto fluorescent Tb^{3+}-HOPO films via exchange and installation of non-fluorescent

metal centers. Here as seen in **Figure 3.8b** the base Tb^{3+}-HOPO film glows green under 254 nm light, but the negative "dark" pattern can be achieved through exchange of Tb centers with other non-fluorescent metal centers such as holmium and iron. Moreover, these approaches allow for potential applications in information storage and encryption[15,74] through careful selection of metal centers patterned into the terbium laden film. As seen in **Figure 3.8**, after patterning holmium centers into the material, the film is still optically transparent and clear in ambient light, and nature of the full pattern can be challenging to discern via the naked, unaided eye. However, under UV light (254 nm) the patterned holmium region of the film is visible, and the entire nature of the image is revealed. While future work is needed to extend the capabilities of this approach to encryption and soft robotics applications, present results provide an encouraging step towards preparing designer materials with readily controlled and localized mechanical, magnetic, and fluorescent responses.

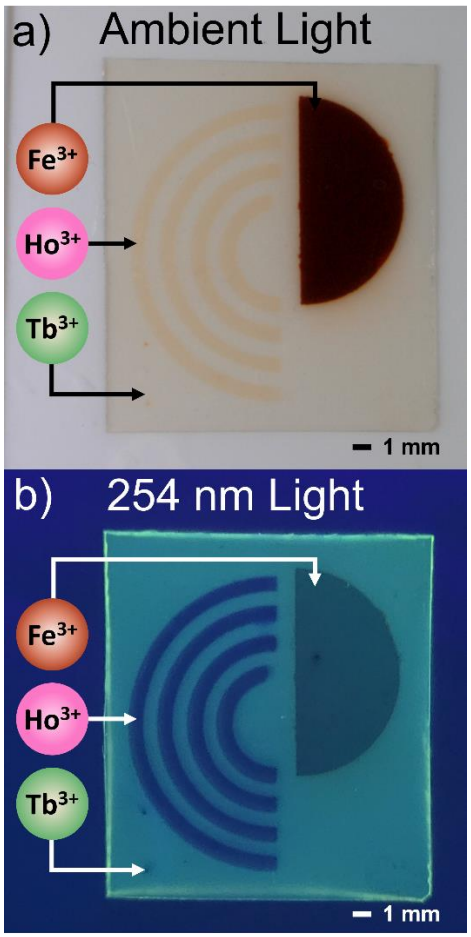


Figure 3.8: (a) Image of a polymer film of 3/39/58 mol% PEGDA/PEGMEA/HOPO under ambient light after complexation with Tb^{3+}, and patterning of Ho^{3+} and Fe^{3+} ions via metal center exchange, with representative metal-ion containing areas denoted via the guide at left. (b) Image of a polymer film of 3/39/58 mol% PEGDA/PEGMEA/HOPO under UV light (254 nm). Here Tb^{3+}-complexed regions of the film glow green while Ho^{3+} and Fe^{3+} patterned surfaces do not fluoresce.

3.4 Conclusions & Future Work

Present results demonstrate a facile and scalable synthesis of HOPO ligands and use in active ester polymer networks for tailored mechanical, magnetic, and luminescent properties. Through utilization of readily available feedstocks, target motifs can be

synthesized easily on gram scales and incorporated through simple wash procedures. Installation of 3,4-HOPO moieties enables preparation of mechanically robust networks which retain many advantages of their catecholate analogues without limitations or challenges in ligand oxidation during long term air exposure. Moreover, this ligand scaffold enables the capture and use of lanthanide ions which retain magnetic and fluorescent properties of interest providing an easy route to locally embed desired functionalities into polymer network materials. Future work on these material systems may enable the development of novel materials for magnetic tweezers, soft robotic materials, and membrane materials for lanthanide capture and recovery.

3.5 References

(1) Zhao, X.; Chen, X.; Yuk, H.; Lin, S.; Liu, X.; Parada, G. Soft Materials by Design: Unconventional Polymer Networks Give Extreme Properties. *Chem. Rev.* **2021**, *121* (8), 4309–4372. https://doi.org/10.1021/acs.chemrev.0c01088.

(2) Ganewatta, M. S.; Wang, Z.; Tang, C. Chemical Syntheses of Bioinspired and Biomimetic Polymers toward Biobased Materials. *Nature Reviews Chemistry 2021 5:11* **2021**, *5* (11), 753–772. https://doi.org/10.1038/s41570-021-00325-x.

(3) Khare, E.; Holten-Andersen, N.; Buehler, M. J. Transition-Metal Coordinate Bonds for Bioinspired Macromolecules with Tunable Mechanical Properties. *Nature Reviews Materials* **2021**, *0123456789*. https://doi.org/10.1038/s41578-020-00270-z.

(4) Bailey, S. J.; Hopkins, E.; Baxter, N. J.; Whitehead, I.; de Alaniz, J. R.; Wilson, M. Z. Diels–Alder Photoclick Patterning of Extracellular Matrix for Spatially Controlled Cell Behaviors. *Advanced Materials* **2023**, *35* (46), 2303453. https://doi.org/10.1002/adma.202303453.

(5) Lin, X.; Wang, X.; Zeng, L.; Wu, Z. L.; Guo, H.; Hourdet, D. Stimuli-Responsive Toughening of Hydrogels. *Chemistry of Materials* **2021**, *33* (19), 7633–7656. https://doi.org/10.1021/ACS.CHEMMATER.1C01019.

(6) Garcia, R. V.; Murphy, E. A.; Sinha, N. J.; Okayama, Y.; Urueña, J. M.; Helgeson, M. E.; Bates, C. M.; Hawker, C. J.; Murphy, R. D.; Read de Alaniz, J. Tailoring Writability and Performance of Star Block Copolypeptides Hydrogels through Side-Chain Design. *Small* **2023**, *19* (50), 2302794. https://doi.org/10.1002/smll.202302794.

(7) Ducrot, E.; Chen, Y.; Bulters, M.; Sijbesma, R. P.; Creton, C. Toughening Elastomers with Sacrificial Bonds and Watching Them Break. *Science* **2014**, *344* (6180), 186–189. https://doi.org/10.1126/SCIENCE.1248494/SUPPL_FILE/DUCROT-SM.PDF.

(8) Liu, J.; Tan, C. S. Y.; Yu, Z.; Li, N.; Abell, C.; Scherman, O. A. Tough Supramolecular Polymer Networks with Extreme Stretchability and Fast Room-Temperature Self-Healing. *Advanced Materials* **2017**, *29* (22), 1605325. https://doi.org/10.1002/adma.201605325.

(9) Vashahi, F.; Martinez, M. R.; Dashtimoghadam, E.; Fahimipour, F.; Keith, A. N.; Bersenev, E. A.; Ivanov, D. A.; Zhulina, E. B.; Popryadukhin, P.; Matyjaszewski, K.; Vatankhah-Varnosfaderani, M.; Sheiko, S. S. Injectable Bottlebrush Hydrogels with Tissue-Mimetic Mechanical Properties. *Science Advances* **2022**, *8* (3), eabm2469. https://doi.org/10.1126/sciadv.abm2469.

(10) Holten-Andersen, N.; Harrington, M. J.; Birkedal, H.; Lee, B. P.; Messersmith, P. B.; Lee, K. Y. C.; Waite, J. H. pH-Induced Metal-Ligand Cross-Links Inspired by Mussel Yield Self-Healing Polymer Networks with near-Covalent Elastic Moduli. *Proceedings of the National Academy of Sciences of the United States of America* **2011**, *108* (7), 2651–2655. https://doi.org/10.1073/pnas.1015862108.

(11) Capadona, J. R.; Shanmuganathan, K.; Tyler, D. J.; Rowan, S. J.; Weder, C. Stimuli-Responsive Polymer Nanocomposites Inspired by the Sea Cucumber Dermis. *Science* **2008**, *319* (5868), 1370–1374. https://doi.org/10.1126/SCIENCE.1153307.

(12) Kim, S.; Regitsky, A. U.; Song, J.; Ilavsky, J.; McKinley, G. H.; Holten-Andersen, N. In Situ Mechanical Reinforcement of Polymer Hydrogels via Metal-Coordinated Crosslink Mineralization. *Nature Communications* **2021**, *12* (1). https://doi.org/10.1038/s41467-021-20953-7.

(13) Li, Z.; Li, Y.; Chen, C.; Cheng, Y. Magnetic-Responsive Hydrogels: From Strategic Design to Biomedical Applications. *Journal of Controlled Release* **2021**, *335*, 541–556. https://doi.org/10.1016/j.jconrel.2021.06.003.

(14) Li, C.; Lau, G. C.; Yuan, H.; Aggarwal, A.; Dominguez, V. L.; Liu, S.; Sai, H.; Palmer, L. C.; Sather, N. A.; Pearson, T. J.; Freedman, D. E.; Amiri, P. K.; de la Cruz, M. O.; Stupp, S. I. Fast and Programmable Locomotion of Hydrogel-Metal Hybrids under Light and Magnetic Fields. *Science Robotics* **2020**, *5* (49), eabb9822. https://doi.org/10.1126/scirobotics.abb9822.

(15) Feng, Y.; White, A. K.; Hein, J. B.; Appel, E. A.; Fordyce, P. M. MRBLES 2.0: High-Throughput Generation of Chemically Functionalized Spectrally and Magnetically Encoded Hydrogel Beads Using a Simple Single-Layer Microfluidic Device. *Microsyst Nanoeng* **2020**, *6* (1), 1–13. https://doi.org/10.1038/s41378-020-00220-3.

(16) Yin, Q.; Wang, L.; Jiang, J.; Dai, C.; Weng, G.; He, J. Three-Dimensional Shape Transformation of Eu3+-Containing Polymer Films through Modulating Dynamic Eu3+-Iminodiacetate Coordination. *Chem. Mater.* **2022**, *34* (5), 2176–2186. https://doi.org/10.1021/acs.chemmater.1c03722.

(17) Filippidi, E.; Cristiani, T. R.; Eisenbach, C. D.; Herbert Waite, J.; Israelachvili, J. N.; Kollbe Ahn, B.; Valentine, M. T. Toughening Elastomers Using Mussel-Inspired Iron-Catechol Complexes. *Science* **2017**, *358* (6362), 502–505. https://doi.org/10.1126/science.aao0350.

(18) Shannon, D. P.; Moon, J. D.; Barney, C. W.; Sinha, N. J.; Yang, K.-C.; Jones, S. D.; Garcia, R. V.; Helgeson, M. E.; Segalman, R. A.; Valentine, M. T.; Hawker, C. J. Modular Synthesis and Patterning of High-Stiffness Networks by Postpolymerization Functionalization with Iron–Catechol Complexes. *Macromolecules* **2023**, *56* (6), 2268–2276. https://doi.org/10.1021/acs.macromol.2c02561.

(19) Weng, G.; Thanneeru, S.; He, J. Dynamic Coordination of Eu–Iminodiacetate to Control Fluorochromic Response of Polymer Hydrogels to Multistimuli. *Advanced Materials* **2018**, *30* (11), 1706526. https://doi.org/10.1002/adma.201706526.

(20) Shi, L.; Ding, P.; Wang, Y.; Zhang, Y.; Ossipov, D.; Hilborn, J. Self-Healing Polymeric Hydrogel Formed by Metal–Ligand Coordination Assembly: Design, Fabrication,

and Biomedical Applications. *Macromolecular Rapid Communications* **2019**, *40* (7), 1800837. https://doi.org/10.1002/marc.201800837.

(21) Yamamoto, M.; Ando, K.; Inoue, M.; Kanoh, H.; Yamagami, M.; Wakiya, T.; Iida, E.; Taniguchi, T.; Kishikawa, K.; Kohri, M. Poly-β-Ketoester Particles as a Versatile Scaffold for Lanthanide-Doped Colorless Magnetic Materials. *ACS Applied Polymer Materials* **2020**, *2* (6), 2170–2178. https://doi.org/10.1021/acsapm.0c00149.

(22) Harrington, M. J.; Masic, A.; Holten-Andersen, N.; Waite, J. H.; Fratzl, P. Iron-Clad Fibers: A Metal-Based Biological Strategy for Hard Flexible Coatings. *Science* **2010**, *328* (5975), 216–220. https://doi.org/10.1126/SCIENCE.1181044.

(23) Joester, D.; Brooker, L. R. The Chiton Radula: A Model System for Versatile Use of Iron Oxides. *Iron Oxides: From Nature to Applications* **2016**, 177–205. https://doi.org/10.1002/9783527691395.CH8/FORMAT/CHAPTER-EPUB.

(24) Lichtenegger, H. C.; Schöberl, T.; Ruokolainen, J. T.; Cross, J. O.; Heald, S. M.; Birkedal, H.; Waite, J. H.; Stucky, G. D. Zinc and Mechanical Prowess in the Jaws of Nereis, a Marine Worm. *Proceedings of the National Academy of Sciences* **2003**, *100* (16), 9144–9149. https://doi.org/10.1073/pnas.1632658100.

(25) Politi, Y.; Priewasser, M.; Pippel, E.; Zaslansky, P.; Hartmann, J.; Siegel, S.; Li, C.; Barth, F. G.; Fratzl, P. A Spider's Fang: How to Design an Injection Needle Using Chitin-Based Composite Material. *Advanced Functional Materials* **2012**, *22* (12), 2519–2528. https://doi.org/10.1002/adfm.201200063.

(26) Lee, S.; Kustin, K.; Robinson, W. E.; Frankel, R. B.; Spartalian, K. Magnetic Properties of Tunicate Blood Cells. I. Ascidia Nigra. *J Inorg Biochem* **1988**, *33* (3), 183–192. https://doi.org/10.1016/0162-0134(88)80048-5.

(27) Fung, T.-M.; Gallego Lazo, C.; Smith, A. M. Elasticity and Energy Dissipation in the Double Network Hydrogel Adhesive of the Slug Arion Subfuscus. *Philosophical Transactions of the Royal Society B: Biological Sciences* **2019**, *374* (1784), 20190201. https://doi.org/10.1098/rstb.2019.0201.

(28) Raymond, K. N.; Allred, B. E.; Sia, A. K. Coordination Chemistry of Microbial Iron Transport. *Acc. Chem. Res.* **2015**, *48* (9), 2496–2505. https://doi.org/10.1021/acs.accounts.5b00301.

(29) Sandy, M.; Butler, A. Microbial Iron Acquisition: Marine and Terrestrial Siderophores. *Chem. Rev.* **2009**, *109* (10), 4580–4595. https://doi.org/10.1021/cr9002787.

(30) Cook, E. C.; Featherston, E. R.; Showalter, S. A.; Cotruvo, J. A. Jr. Structural Basis for Rare Earth Element Recognition by Methylobacterium Extorquens Lanmodulin. *Biochemistry* **2019**, *58* (2), 120–125. https://doi.org/10.1021/acs.biochem.8b01019.

(31) Cotruvo, J. A. Jr.; Featherston, E. R.; Mattocks, J. A.; Ho, J. V.; Laremore, T. N. Lanmodulin: A Highly Selective Lanthanide-Binding Protein from a Lanthanide-Utilizing Bacterium. *J. Am. Chem. Soc.* **2018**, *140* (44), 15056–15061. https://doi.org/10.1021/jacs.8b09842.

(32) Cotruvo, J. A. Jr. The Chemistry of Lanthanides in Biology: Recent Discoveries, Emerging Principles, and Technological Applications. *ACS Cent. Sci.* **2019**, *5* (9), 1496–1506. https://doi.org/10.1021/acscentsci.9b00642.

(33) Cilibrizzi, A.; Abbate, V.; Chen, Y.-L.; Ma, Y.; Zhou, T.; Hider, R. C. Hydroxypyridinone Journey into Metal Chelation. *Chem. Rev.* **2018**, *118* (16), 7657–7701. https://doi.org/10.1021/acs.chemrev.8b00254.

(34) Raymond, K. N. Biomimetic Metal Encapsulation. *Coordination Chemistry Reviews* **1990**, *105*, 135–153. https://doi.org/10.1016/0010-8545(90)80020-T.

(35) Tanaka, K.; Tengeiji, A.; Kato, T.; Toyama, N.; Shiro, M.; Shionoya, M. Efficient Incorporation of a Copper Hydroxypyridone Base Pair in DNA. *J. Am. Chem. Soc.* **2002**, *124* (42), 12494–12498. https://doi.org/10.1021/ja027175o.

(36) Datta, A.; Raymond, K. N. Gd−Hydroxypyridinone (HOPO)-Based High-Relaxivity Magnetic Resonance Imaging (MRI) Contrast Agents. *Acc. Chem. Res.* **2009**, *42* (7), 938–947. https://doi.org/10.1021/ar800250h.

(37) Honda, M. D. H.; Borthakur, D. Mimosine Facilitates Metallic Cation Uptake by Plants through Formation of Mimosine–Cation Complexes. *Plant Mol Biol* **2020**, *102* (4), 431–445. https://doi.org/10.1007/s11103-019-00956-1.

(38) Honda, M. D. H.; Borthakur, D. Mimosine Facilitates Fe Uptake by Leucaena Leucocephala Subsp. Glabrata in Alkaline Soils by Solubilizing Fe-Oxides. *Plant Soil* **2023**, *484* (1), 279–292. https://doi.org/10.1007/s11104-022-05789-4.

(39) Mendonça, A. C.; Martins, A. F.; Melchior, A.; Marques, S. M.; Chaves, S.; Villette, S.; Petoud, S.; Zanonato, P. L.; Tolazzi, M.; Bonnet, C. S.; Tóth, É.; Bernardo, P. D.; Geraldes, C. F. G. C.; Santos, M. A. New Tris-3,4-HOPO Lanthanide Complexes as Potential Imaging Probes: Complex Stability and Magnetic Properties. *Dalton Trans.* **2013**, *42* (17), 6046–6057. https://doi.org/10.1039/C2DT32237D.

(40) Wang, Y.; Deblonde, G. J.-P.; Abergel, R. J. Hydroxypyridinone Derivatives: A Low-pH Alternative to Polyaminocarboxylates for TALSPEAK-like Separation of Trivalent Actinides from Lanthanides. *ACS Omega* **2020**, *5* (22), 12996–13005. https://doi.org/10.1021/acsomega.0c00873.

(41) Puerta, D. T.; Lewis, J. A.; Cohen, S. M. New Beginnings for Matrix Metalloproteinase Inhibitors: Identification of High-Affinity Zinc-Binding Groups. *J. Am. Chem. Soc.* **2004**, *126* (27), 8388–8389. https://doi.org/10.1021/ja0485513.

(42) Menyo, M. S.; Hawker, C. J.; Waite, J. H. Versatile Tuning of Supramolecular Hydrogels through Metal Complexation of Oxidation-Resistant Catechol-Inspired Ligands. *Soft Matter* **2013**, *9* (43), 10314–10323. https://doi.org/10.1039/C3SM51824H.

(43) Chaves, S.; Gwizdała, K.; Chand, K.; Gano, L.; Pallier, A.; Tóth, É.; Amélia Santos, M. Gd III and Ga III Complexes with a New Tris-3,4-HOPO Ligand as New Imaging Probes: Complex Stability, Magnetic Properties and Biodistribution. *Dalton Transactions* **2022**, *51* (16), 6436–6447. https://doi.org/10.1039/D2DT00066K.

(44) Cen, J.; Zhu, H.; Hong, C.; Zhang, X.; Liu, S.; Yang, B.; Yu, Y.; Wen, Y.; Cao, J.; Chen, W. Synthesis and Structure-Activity Optimization of Hydroxypyridinones against Rhabdomyolysis-Induced Acute Kidney Injury. *European Journal of Medicinal Chemistry* **2024**, *263*, 115933. https://doi.org/10.1016/j.ejmech.2023.115933.

(45) Santos, M. A.; Marques, S. M.; Chaves, S. Hydroxypyridinones as "Privileged" Chelating Structures for the Design of Medicinal Drugs. *Coordination Chemistry Reviews* **2012**, *256* (1), 240–259. https://doi.org/10.1016/j.ccr.2011.08.008.

(46) Menyo, M. S.; Hawker, C. J.; Waite, J. H. Rate-Dependent Stiffness and Recovery in Interpenetrating Network Hydrogels through Sacrificial Metal Coordination Bonds. *ACS Macro Lett.* **2015**, *4* (11), 1200–1204. https://doi.org/10.1021/acsmacrolett.5b00664.

(47) Andersen, A.; Krogsgaard, M.; Birkedal, H. Mussel-Inspired Self-Healing Double-Cross-Linked Hydrogels by Controlled Combination of Metal Coordination and Covalent Cross-Linking. *Biomacromolecules* **2017**. https://doi.org/10.1021/acs.biomac.7b01249.

(48) Ke, D.; Zhang, L.; Zhong, X.; Shao, J.; Yu, Y.; Chen, W. Boronic-Acid-Accelerated Electrophilic Activation of Unprotected Maltols to N-Substituted Hydroxypyridinones in Water. *Org. Lett.* **2022**, *24* (6), 1263–1267. https://doi.org/10.1021/acs.orglett.1c03833.

(49) Moon, J. D.; Sujanani, R.; Geng, Z.; Freeman, B. D.; Segalman, R. A.; Hawker, C. J. Versatile Synthetic Platform for Polymer Membrane Libraries Using Functional Networks. *Macromolecules* **2021**, *54* (2), 866–873. https://doi.org/10.1021/acs.macromol.0c02414.

(50) Kohaku, K.; Inoue, M.; Kanoh, H.; Taniguchi, T.; Kishikawa, K.; Kohri, M. Full-Color Magnetic Nanoparticles Based on Holmium-Doped Polymers. *ACS Applied Polymer Materials* **2020**, *2* (5), 1800–1806. https://doi.org/10.1021/ACSAPM.0C00038.

(51) Jiang, F.; Wang, Z.; Zhang, X.; Henderson, D.; Hwang, W.; Briber, R. M.; Wang, H. Synergistically Tailoring Mechanical and Optical Properties of Diblock Copolymer Thermoplastic Elastomers via Lanthanide Coordination. *Chem. Mater.* **2022**, *34* (4), 1578–1589. https://doi.org/10.1021/acs.chemmater.1c03264.

(52) Gomes, M. C.; Costa, D. C. S.; Oliveira, C. S.; Mano, J. F. Design of Protein-Based Liquefied Cell-Laden Capsules with Bioinspired Adhesion for Tissue Engineering. *Advanced Healthcare Materials* **2021**, *10* (19), 2100782. https://doi.org/10.1002/adhm.202100782.

(53) Cristiani, T. R.; Filippidi, E.; Behrens, R. L.; Valentine, M. T.; Eisenbach, C. D. Tailoring the Toughness of Elastomers by Incorporating Ionic Cross-Linking. *Macromolecules* **2020**, *53* (10), 4099–4109. https://doi.org/10.1021/acs.macromol.0c00500.

(54) Barrett, D. G.; Fullenkamp, D. E.; He, L.; Holten-Andersen, N.; Lee, K. Y. C.; Messersmith, P. B. pH-Based Regulation of Hydrogel Mechanical Properties Through Mussel-Inspired Chemistry and Processing. *Advanced Functional Materials* **2013**, *23* (9), 1111–1119. https://doi.org/10.1002/adfm.201201922.

(55) Yang, J.; Cohen Stuart, M. A.; Kamperman, M. Jack of All Trades: Versatile Catechol Crosslinking Mechanisms. *Chemical Society Reviews* **2014**, *43* (24), 8271–8298. https://doi.org/10.1039/c4cs00185k.

(56) Andersen, A.; Krogsgaard, M.; Birkedal, H. Mussel-Inspired Self-Healing Double-Cross-Linked Hydrogels by Controlled Combination of Metal Coordination and Covalent Cross-Linking. *Biomacromolecules* **2018**, *19* (5), 1402–1409. https://doi.org/10.1021/acs.biomac.7b01249.

(57) Pillar-Little, E. A.; Zhou, R.; Guzman, M. I. Heterogeneous Oxidation of Catechol. *J. Phys. Chem. A* **2015**, *119* (41), 10349–10359. https://doi.org/10.1021/acs.jpca.5b07914.

(58) Lagutschenkov, A.; Langer, J.; Berden, G.; Oomens, J.; Dopfer, O. Infrared Spectra of Protonated Neurotransmitters : Dopamine. *Physical Chemistry Chemical Physics* **2011**, *13* (7), 2815–2823. https://doi.org/10.1039/C0CP02133D.

(59) Zangmeister, R. A.; Morris, T. A.; Tarlov, M. J. Characterization of Polydopamine Thin Films Deposited at Short Times by Autoxidation of Dopamine. *Langmuir* **2013**, *29* (27), 8619–8628. https://doi.org/10.1021/la400587j.

(60) Šebestík, J.; Šafařík, M.; Bouř, P. Ferric Complexes of 3-Hydroxy-4-Pyridinones Characterized by Density Functional Theory and Raman and UV–Vis Spectroscopies. *Inorg. Chem.* **2012**, *51* (8), 4473–4481. https://doi.org/10.1021/ic202004d.

(61) Jianlin, Y.; Yaxian, Y.; Renao, G. Raman Spectroscopic Studies on Tropolone Complexes with La, Nd, Sm, Yb. *Spectrochimica Acta Part A: Molecular and Biomolecular Spectroscopy* **2006**, *64* (4), 1072–1076. https://doi.org/10.1016/j.saa.2005.09.017.

(62) Burden, K. J.; Thornton, D. A.; Watkins, G. M. A Re-Examination of the Infrared Spectra of First Transition Series Metal(II) and Metal(III) Tropolonates. *Spectrochimica Acta Part A: Molecular Spectroscopy* **1989**, *45* (11), 1179–1186. https://doi.org/10.1016/0584-8539(89)80198-9.

(63) Parajón-Costa, B. S.; Baran, E. J.; Romero, J.; Sáez-Puche, R.; Arrambide, G.; Gambino, D. Synthesis and Characterization of Bistropolonato Oxovanadium(IV and V) Complexes. *Journal of Coordination Chemistry* **2011**, *64* (1), 57–70. https://doi.org/10.1080/00958972.2010.531131.

(64) Xin, Q.; Li, P.; He, Y.; Shi, C.; Qiao, Y.; Bian, X.; Su, J.; Qiao, R.; Zhou, X.; Zhong, J. Magnetic Tweezers for the Mechanical Research of DNA at the Single Molecule Level. *Analytical Methods* **2017**, *9* (39), 5720–5730. https://doi.org/10.1039/C7AY01495C.

(65) Pena-Francesch, A.; Zhang, Z.; Marks, L.; Cabanach, P.; Richardson, K.; Sheehan, D.; McCracken, J.; Shahsavan, H.; Sitti, M. Macromolecular Radical Networks for Organic Soft Magnets. *Matter* **2024**, *0* (0). https://doi.org/10.1016/j.matt.2023.12.015.

(66) Kim, Y.; Zhao, X. Magnetic Soft Materials and Robots. *Chem. Rev.* **2022**, *122* (5), 5317–5364. https://doi.org/10.1021/acs.chemrev.1c00481.

(67) Ebrahimi, N.; Bi, C.; Cappelleri, D. J.; Ciuti, G.; Conn, A. T.; Faivre, D.; Habibi, N.; Hošovský, A.; Iacovacci, V.; Khalil, I. S. M.; Magdanz, V.; Misra, S.; Pawashe, C.; Rashidifar, R.; Soto-Rodriguez, P. E. D.; Fekete, Z.; Jafari, A. Magnetic Actuation Methods in Bio/Soft Robotics. *Advanced Functional Materials* **2021**, *31* (11), 2005137. https://doi.org/10.1002/adfm.202005137.

(68) Zhu, D.-H.; Kappel, M. J.; Raymond, K. N. Coordination Chemistry of Lanthanide Catecholates. *Inorganica Chimica Acta* **1988**, *147* (1), 115–121. https://doi.org/10.1016/S0020-1693(00)80639-8.

(69) Menyo, M. S. Fine-Tuning Catechol Reactivity in Synthetic Polymeric Materials.

(70) Bracher, P. J.; Gupta, M.; Whitesides, G. M. Shaped Films of Ionotropic Hydrogels Fabricated Using Templates of Patterned Paper. *Advanced Materials* **2009**, *21* (4), 445–450. https://doi.org/10.1002/adma.200801186.

(71) Bünzli, J.-C. G. Lanthanide Luminescence for Biomedical Analyses and Imaging. *Chem. Rev.* **2010**, *110* (5), 2729–2755. https://doi.org/10.1021/cr900362e.

(72) Cheisson, T.; Schelter, E. J. Rare Earth Elements: Mendeleev's Bane, Modern Marvels. *Science* **2019**, *363* (6426), 489–493. https://doi.org/10.1126/science.aau7628.

(73) Martell, A. E.; Smith, R. M. *Critical Stability Constants: First Supplement*; Springer US: Boston, MA, 1982. https://doi.org/10.1007/978-1-4615-6761-5.

(74) Zhou, Y.; Hao, K.; Liu, C.; Yu, R.; Huang, A.; Wu, C.; Yang, Y.; Zuo, X. 3D Printed Hydrogels with Time/Temperature-Dependent Photoluminescence for Multi-Information Dynamic Display. *ACS Appl. Polym. Mater.* **2024**. https://doi.org/10.1021/acsapm.3c02863.

Chapter 4. Solution-like Water Transport Across Molecular to Macroscopic Length Scales in Crosslinked Poly(ethylene glycol diacrylate) Networks with Tailored Sidechains

Text and Figures reprinted and adapted from Webber, T. R.*, Shannon, D.*, et al. (2024). Solution-like Water Transport Across Molecular to Macroscopic Length Scales in Crosslinked Poly(ethylene glycol diacrylate) Networks with Tailored Sidechains. doi.org/10.XXXX/XXXX *in preparation.*

*denotes equal contribution

4.1 Abstract

Poly(ethylene glycol) (PEG)-based materials, like PEG-diacrylate (PEGDA), are prized for their hydrophilic, inert properties, and leveraged in hydrogels and as membrane mimics. While network chemistry is often tuned for selective transport and antifouling, fundamental understanding of water dynamics at the network surface and impact on bulk transport is limited. We utilize Overhauser dynamic nuclear polarization (ODNP) to measure nanoscale water diffusivity near a tethered spin label at the water-polymer surface and compare to bulk water diffusivity from pulsed field gradient (PFG) NMR. *Via* active ester chemistry, spin labels and varied sidechain chemistries are introduced, modulating network hydrophilicity. Tuning network hydration through crosslinker content and functional groups further impacts water diffusivity. Results show rapid nanoscale water transport at the polymer surface, reflecting network volumetric water content, with further modulation by sidechain

functionality. These findings demonstrate PEGDA's utility as a membrane mimic and the critical impact of network chemistry on water transport.

4.2 Introduction

Polymer membrane technologies play a central role in water treatment and desalination due to their energy and cost efficiency. Designing the next generation of high-performance membrane materials requires a number of enhancements including high permeability, selective separation of solutes, and improved antifouling behavior. To imbue model membrane materials with tailored properties for ion selectivity and fouling resistance, chemical modifications of the network structure should be leveraged, given that ion selection and membrane fouling are molecular events that occur within sub-nanometer length scales from the polymer surface.[1,2] However, current membrane design relies on empirical approaches and lacks a fundamental understanding of the relationship between the network structure, chemistry, and surface activity for the transport of water and solutes across model membrane materials.[1,3] Furthermore, even when tailored surface modifications are engineered into membrane models, the majority of studies on membrane transport characterize macroscopic diffusion effects.[4] These multiplexed problems, combined with synthetic challenges and a vast design space, make it difficult to identify molecularly-informed design rules and privileged building blocks on transport at multiple length scales.[5]

One of the most widely used polymers to impart hydrophilicity and antifouling behavior to membrane materials is poly(ethylene glycol) (PEG).[6–16] PEG-based cross-linked networks further improve mechanical stability[13–15,17] while maintaining many of the desired properties, such as high permeability and resistance to fouling, critical for applications as

coatings for water treatment membranes.[4,18–24] In particular, cross-linked poly(ethylene glycol diacrylate) (PEGDA) networks are a common material which exhibits high hydrophilicity and facile control over water swelling behavior and transport properties through network design.[4,19,20,24,25] Furthermore, they can be readily synthesized from low-cost materials in mild (photoinitiated) radical polymerization conditions.[5,26] Still, the majority of studies on cross-linked PEGDA hydrogels in membranes have focused on studying macroscopic bulk properties, such as swelling, permeation, salt sorption, and fouling, driven by applications in membrane coatings. However the desirable properties and utility of PEGDA-based materials has been noted in other areas of research, leading to wide adoption in diverse settings from biomaterials to microparticle systems, where molecular scale effects of network structure and chemistry are also of interest.[16,27,28] In particular, the degree of crosslinking and corresponding water uptake of the network is critical across these applications, and it is well established that varying the ratio of PEGDA monomers to pre-polymerization water, as well as the ratio of PEGDA (cross-linking monomer) to a mono PEG-acrylate (diluent monomer) provides facile control of network water contetnt.[24,26,29] Hydrogels with higher water contents show increased water permeability and diffusivity as measured by membrane permeation, with solute or ion diffusion closely coupled to water diffusion.[24,26,29–33] However, what is not known is whether it is strictly the network structuring of the cross-linked PEGDA that dictates transport or whether polymer surface chemistry impacts water or solute dynamics, either near the surface or across length scales.

Even though PEGDA networks have been widely used, the mesoscale, network structural features of cross-linked PEGDA hydrogels and the associated impact of network chemistry on transport are still active, developing areas of research[34–37]. Cross-linked PEGDA

is in many ways a non-ideal and structurally complex material. Work from Malo de Molina et al. have demonstrated the heterogeneous nature of PEGDA networks, which arrange into star-like structures with polymer-rich and water-rich domains, with characteristic length scales controlled by the molecular weight of the cross-linking diacrylate.[34] Previous transport work in PEGDA hydrogels has focused largely on macroscopic permeation measurements to extract water or ion diffusion coefficients using the solution-diffusion model.[24,30–32] More recently, efforts by Nordness et al. have demonstrated successful characterization of PEGDA hydrogels using PFG-NMR to obtain water and ion diffusion at micrometer length scales and millisecond time scales to show that water content in the hydrogel is the primary driver for diffusivity and is closely coupled to ion transport[38]. Conversely, even for simple mixtures of low molecular weight PEG and water, fundamental insights of nanoscopic water diffusion and structuring at the polymer surface are new, as discussed in a recent study from Moon et al. Their work combined experimental pulsed field gradient (PFG)-NMR measurements with Overhauser dynamic nuclear polarization (ODNP) spectroscopy, in conjunction with molecular dynamics (MD) simulations, to find that the molecular structuring of water around the ethylene oxide repeat units directly impacted the dynamics of water local to and at a distance from the polymer chain.[39] Diffusion properties at the macroscale are modulated by molecular scale water-polymer interactions, which have significant implications for tailoring structure-property relationships in cross-linked polymer hydrogels. Moreover, recent work from Jiao et al. applied MD simulation and ODNP spectroscopy to explore the effect of local chemical modifications on surface water structure and dynamics[40]. Crucially, they demonstrate that the sequence of nonpolar and polar sidechains on model polypeptoids influences collective water properties, and that hydrophobic, nonpolar species give rise to

slower, more tetrahedrally-oriented water structures.[40] Such results in model systems on the nanoscale demonstrate the appreciable impact of chemical identity on local water structure and dynamics. Moreover, these studies highlight the potential of leveraging ODNP in tandem with PFG-NMR to build a multi-length scale, molecularly-informed understanding of how local chemical interactions and mesoscale polymer structuring impact water diffusion within PEGDA and other membrane materials.

The use of ODNP to study water dynamics in complex polymer environments provides critical molecular-level insight owing to the inherent sub-nanometer length scale of observation. ODNP is a magnetic resonance technique that relies on the excitation of the electron paramagnetic resonance (EPR) of a nitroxide radical-based spin label which induces amplification of the ^{1}H nuclear magnetic resonance (NMR) signal. This dipolar interaction between the electron spin label and nuclear spin of water leads to cross relaxation.[41,42] The interaction strength between the free electron and ^{1}H nucleus depends on their distance of closest approach and the relative speed of the water molecule within the dipolar field of the spin label. Given that the EPR frequency is on the order of 10 GHz, the dipolar correlation time of water near the spin label is on the order of sub-nanosecond timescales. In this way, ODNP uniquely captures translational, diffusive water transport with nanometer scale spatial resolution in complex, or even crowded, molecular surface environments. ODNP has been successfully applied to study the hydration dynamics of DNA surfaces[43], CheY protein[44], lipid bilayers[45], silica nanoparticles[46,47], and micellar polymer structures[48]. ODNP provides new insight into the dynamic nature of polymer or hydrogel environments not afforded by other techniques.

In this work, we leverage flow synthesis to form cross-linked PEGDA network microparticles with tethered spin labels incorporated into the network to investigate the effect of water content on nanoscale water transport measured by ODNP spectroscopy for the first time. We compare ODNP water diffusivities to those derived from PFG-NMR to ask the question: does diffusion measured at multiple length scales agree and does the irregular microstructure of the PEG acrylate network hinder water motion at the molecular level? Present results indicate that local polymer-water interactions underpin molecular scale transport, which behaves in an unhindered, solution-like fashion. We further explore the interplay between chemical functionalization of the polymer network and water dynamics by the addition of secondary sidechain moieties with tunable hydrophilicity. We find at the nanoscale, hydrophobic groups can slow local water diffusivity, while hydrophilic groups further accelerate local water diffusivity, but broadly such effects are not observed using PFG-NMR. These results are significant in demonstrating the importance of molecular-scale techniques such as ODNP for probing local chemical interactions. The connection between local chemical functionality and water dynamics suggests design rules for independently modulating water and solute behavior near tailored surfaces while keeping macroscopic transport unaltered. These findings establish important molecular insights to design rules governing water dynamics in PEG-based hydrogels which inspire next-generation engineering of advanced water treatment membranes.

4.3 Results and Discussion

In this study, cross-linked PEGDA serves as a model material to understand nanoscale water diffusion in a dense polymer membrane, and biphasic flow synthesis was leveraged to

prepare network microparticles amenable to the constraints of the capillaries needed for ODNP. Our study relies on nitroxide radical-based spin labels, applying ODNP as a molecular scale technique to measure inherently sub-nanosecond water diffusion local to the spin label with nanometer scale spatial resolution. However, there are considerable practical challenges we needed to overcome in order to perform ODNP experiments on water inside a swollen hydrogel network. Since ODNP measurements are conventionally performed on aqueous solution samples loaded into a capillary (0.6 mm ID) with small internal volume (~5 µL) placed within a modified NMR probe and EPR magnet, it is critical that a strictly controlled sample quantity be loaded into the capillary for sample-to-sample reproducibility. To achieve this, one must consistently synthesize, functionalize, and load a hydrogel into a narrow-bore capillary without impacting the equilibrium water volume fraction of the network *via* compression or wall constraints, and this is a non-trivial challenge.

Synthesis of active ester polymer networks as microparticles allows for the preparation of EPR-active, functionalized materials which can be loaded into narrow bore capillaries reproducibly at equilibrium water content. Recent work from Moon et al.[5] and others[36,49–53] have demonstrated amidation of pentafluorophenyl acrylate (PFPA) active ester repeat units as a simple and versatile method to install a wide array of functional groups into PEGDA networks.[5] This method enables the direct installation of nitroxide-radical spin labels (*e.g.*, 4-amino-2,2,6,6-tetramethylpiperidine-1-oxyl (4-amino-TEMPO)) at active ester sites through simple synthetic protocols. This post-polymerization approach is compatible with conventional radical polymerization techniques used to prepare PEGDA hydrogels and avoids limitations of traditional approaches which would require protection-deprotection chemistries to prevent loss of spin label radical electrons during the polymerization. This approach can be

conducted on polymer gels of various geometries, enabling preparation of microparticle networks which can be easily functionalized and loaded into narrow bore EPR capillaries at equilibrium water content. This allows the synthesis of functional materials without limitations of spin label protection, obstructed water content control, or constraints imposed by capillary geometry.

A versatile approach to prepare polymer network microparticles was then developed based on liquid-liquid plug flow, which allows a wide range of crosslinker compositions and resulting network water contents to be screened (**Figure 4.1** and **Scheme 4.1)**. From a neat mixture of monomers: diacrylate crosslinker (poly(ethylene glycol) diacrylate, PEGDA, Mn 700), monofunctional diluent monomer (poly(ethylene glycol) methyl ether acrylate, PEGMEA, Mn 480), and active ester monomer, (pentafluorophenyl acrylate, PFPA), crosslinker content was varied from 1.7 mol% to 92 mol%, allowing for a library of network structures and water content values to be prepared. Mild initiation by UV irradiation (3 mW/cm^2) at 365 nm using 2,2-dimethoxy-2-phenylacetophenone as the photo-initiator (1 wt.%, DMPA) led to efficient polymerization and crosslinking of microparticle networks during flow synthesis with short residence times (ca. ~30 seconds). Microparticle size could be controlled by concomitant flow of the monomer mixture and a fluorous oil through narrow bore, 100-micron internal diameter PFA tubing, with flow being driven by separate syringe pumps. Specific resin compositions, procedures, and additional parameters are provided in **Appendix C**. Key to the success of this strategy was the selection of a highly inert fluorous phase which preferentially wets the fluoropolymer tubing walls, encapsulating the monomers into well-defined plugs, with minimal sidewall sticking. Moreover, the immiscibility of the fluorous carrier with acrylate monomers allows for incorporation of both PEG-acrylate and

active ester monomers into the microparticles followed by simple workup, *via* separation and washing to remove any residual, unreacted monomers and carrier solvent. The resultant PFPA (pentafluorophenyl acrylate) containing microparticle network polymers could then be characterized by Fourier-transform infrared (FTIR) spectroscopy to determine relative active ester content, followed by quantitative functionalization with 4-amino-TEMPO following established techniques[5] (**Scheme 4.1** and **Appendix C)**.

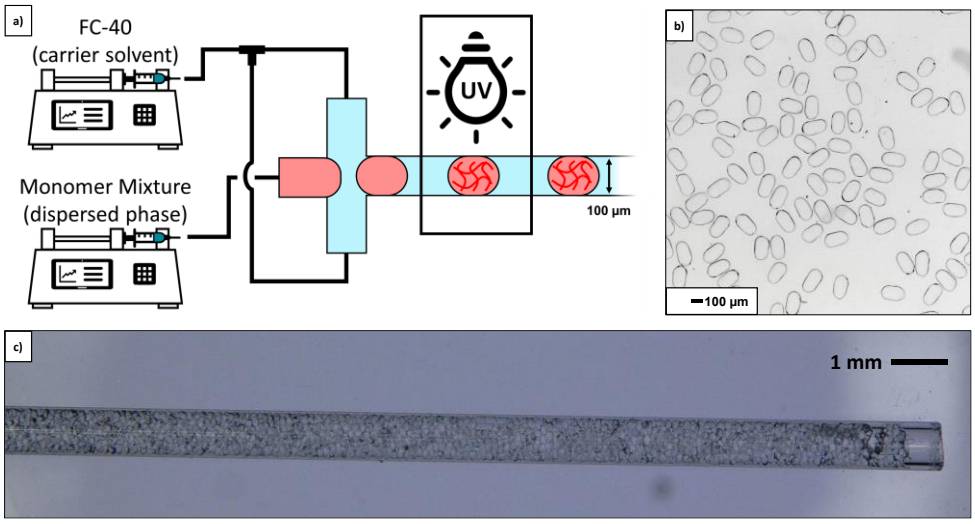
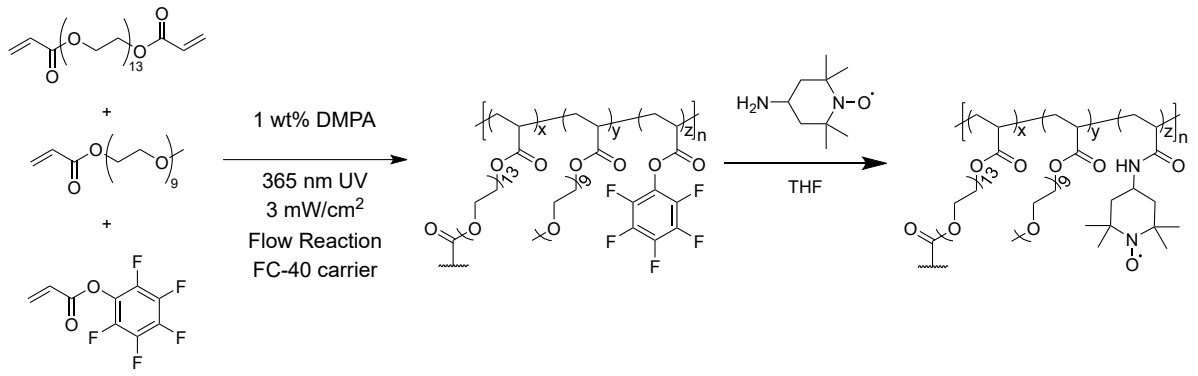


Figure 4.1. (a) Schematic of the microfluidic flow reactor to synthesize PEGDA microparticles of varying cross-linking densities. (b) Optical microscopy image of water swollen PEGDA microparticles (16 mol% PEGDA). (c) Optical microscope image of a capillary filled with PEGDA microparticles



Scheme 4.1. Polymerization of active ester microparticles and substitution of PFPA sites with 4-amino-TEMPO to prepare EPR-active particles for water diffusivity measurements.

Volumetric water content of swollen polymer networks was determined by measuring dilatory changes in the wet and dry state with close agreement between values determined for the microparticles and bulk sample networks of equivalent crosslinker content. Microparticle dimensions and area were analyzed with optical microscopy using a Keyence VHX 5000 microscope, and image analysis was conducted with the associated software package. Particles of varying water content and functionality could be measured in the native hydrated state and again after overnight vacuum drying at ambient temperature (**Figure 4.2a**). Average particle dimensions and area in each state were tabulated across large samples of microparticles (*e.g.*, > 200 individual particles per network composition) and used to determine the average water volume fraction of the network, assuming isotropic swelling, as per **Equation 4.1.**[54] Equivalent methods to determine water volume fraction in bulk films could be conducted by measuring punch sample diameters and areas in the wet and dry states. Results of water volume fraction calculations by these methods are shown in **Figure 4.2b**. As expected, networks with lower diacrylate (crosslinker) content have greater water volume

fractions in both bulk films and microparticles. These results indicate good agreement between the water content of bulk materials and microparticle networks substituted with 4-amino-TEMPO, with slightly increased swelling in the microparticle networks. **Figure 4.2c** depicts the network structure of cross-linked PEGDA, showing representative high and low crosslinker contents and the effect on equilibrium water content. Additional water swelling data for microparticles with mixed substitutions are included in **Appendix C**.

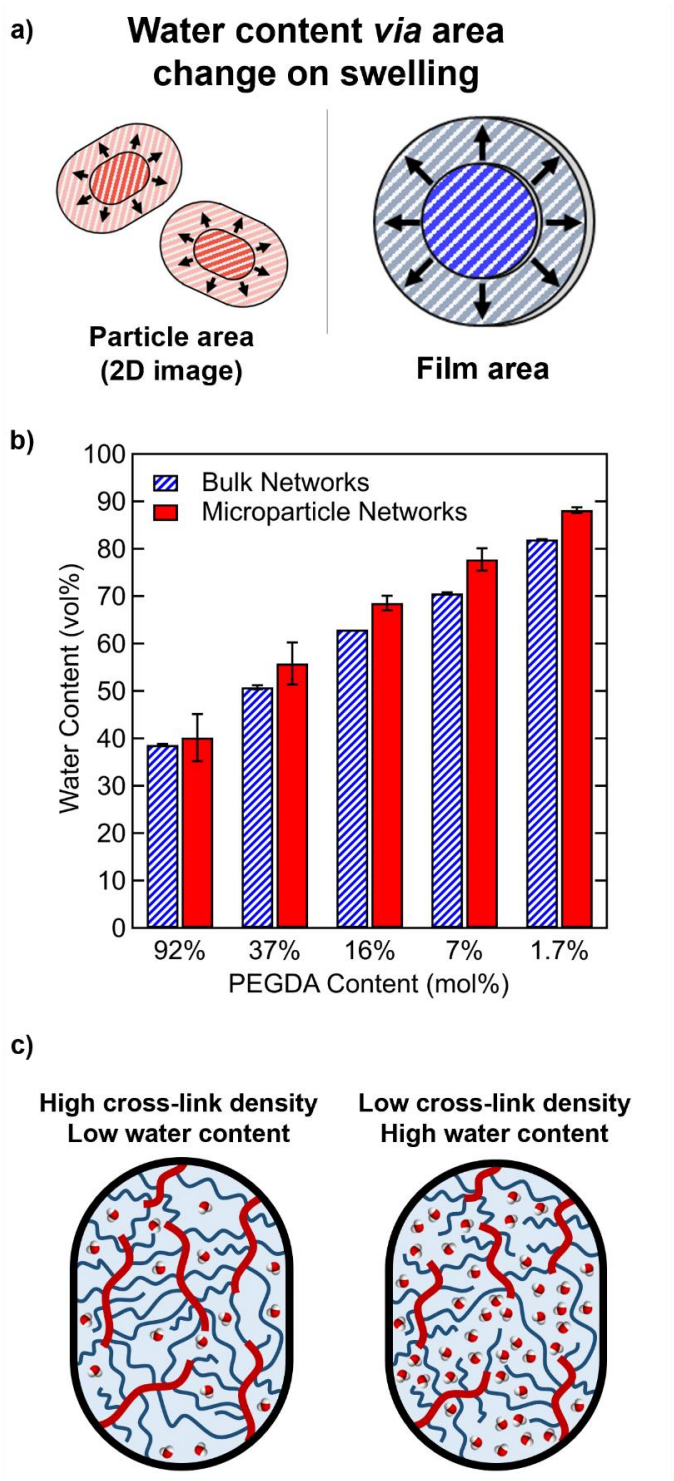


Figure 4.2. (a) Schematic representation of water swelling in PEGDA microparticles and bulk networks. (b) Water uptake in cross-linked PEGDA networks for microparticles (red) and bulk film networks (blue). (c) Cartoon representation showing cross-linked PEGDA network chemistry for low and high water content networks.

Equation 4.1: Water content determination from particle or bulk film area changes with water swelling.[54] V_{water} represents the volumetric water content (in vol %) and A_{wet} and A_{dry} represent the wet and dry area respectively of either microparticle area determined by microscope image analysis, or by calculating circular, macroscopic punch sample area from diameter.

$$V_{water} = 1 - \left(\frac{A_{wet}}{A_{dry}}\right)^{\frac{3}{2}}$$

ODNP and PFG-NMR experiments were performed to characterize the water self-diffusion across different length scales in PEGDA networks of varying water content. ODNP experiments were significantly enabled by the ability to load the network microparticles into narrow capillary sample holders in a reproducible and efficient manner (see **Appendix C** for loading techniques and experimental details). All network samples targeted approximately 500 μM TEMPO spin concentration and were measured at 18 °C. PFG-NMR experiments were then performed at 20 °C for water-swollen, bulk PEGDA hydrogel strips of the same network composition following the methods of Nordness et al.[38] PFG-NMR measurements were performed on bulk films rather than microparticles to directly measure water within the hydrogel samples and avoid errant signal contributions from water present in the interstitial spaces between particles (see **Appendix C** for more details). **Figure 4.3b** shows PFG-NMR bulk water diffusion coefficients measured for these PEGDA network hydrogels in comparison to previously published PFG-NMR bulk water diffusion coefficients in linear PEG polymer solutions, plotted along the water volume fraction calculated from solution densities. Both the PEGDA and PEG solution water diffusivities increase with increasing water content and display remarkable agreement despite the obvious differences in

crosslinking and water environments. In line with prior literature[24,38], we show that, at the microscale, the main driver for water diffusion is the total water volume content, and that water diffusivities within a solid, crosslinked network are unhindered, exhibiting solution-like behavior. PFG-NMR bulk water diffusion coefficients and ODNP local water diffusion coefficients within PEGDA microparticles are plotted in **Figure 4.3c** for networks of different composition and water volume fraction upon swelling. ODNP results demonstrate that the higher water content networks exhibit faster water dynamics, in line with previous studies from PFG-NMR and permeation measurements.[24,32,38] In addition, ODNP reveals that even on the nanometer scale, water probed within 1 nm of the PEGDA acrylate backbone exhibits water motion just as rapid as that sensed by PFG-NMR. The local water motion is relatively unhindered through interaction with the polymer backbone even at the nanometer length scale. Significantly, these two techniques show considerable qualitative and quantitative agreement, despite the vastly different length scales probed during measurement.

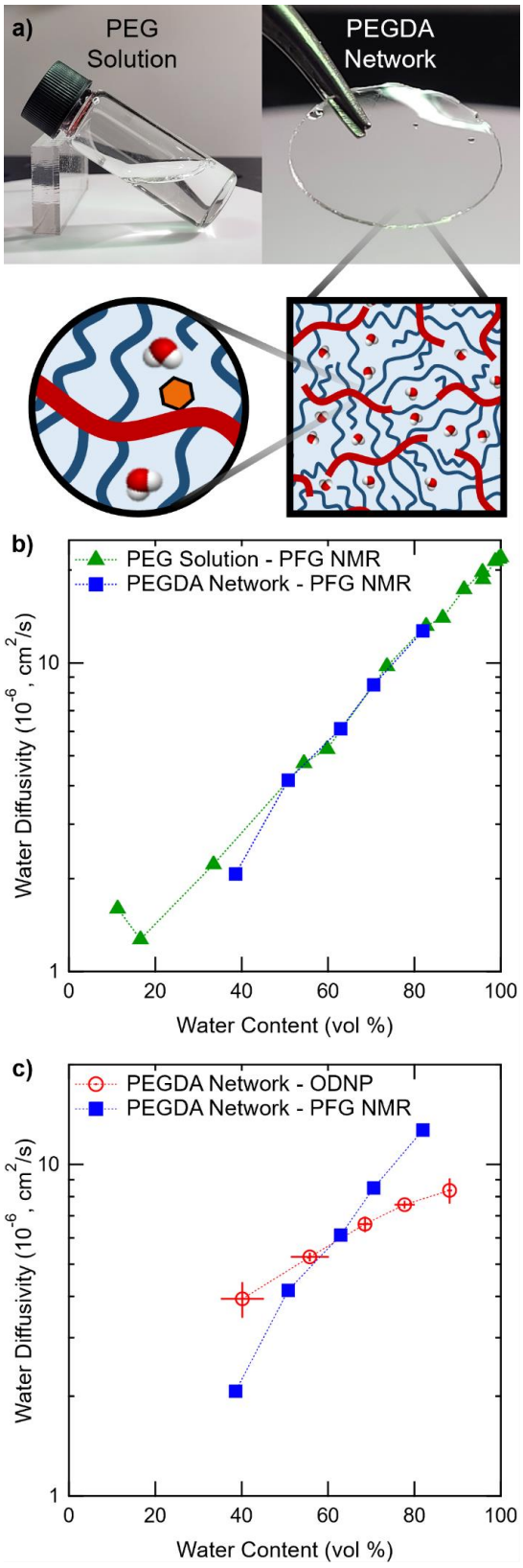

a)
PEG
Solution
PEGDA
Network
b)
PEG Solution - PFG NMR
PEGDA Network - PFG NMR
Water Diffusivity (10^-6, cm^2/s)
Water Content (vol %)
c)
PEGDA Network - ODNP
PEGDA Network - PFG NMR
Water Diffusivity (10^-6, cm^2/s)
Water Content (vol %)

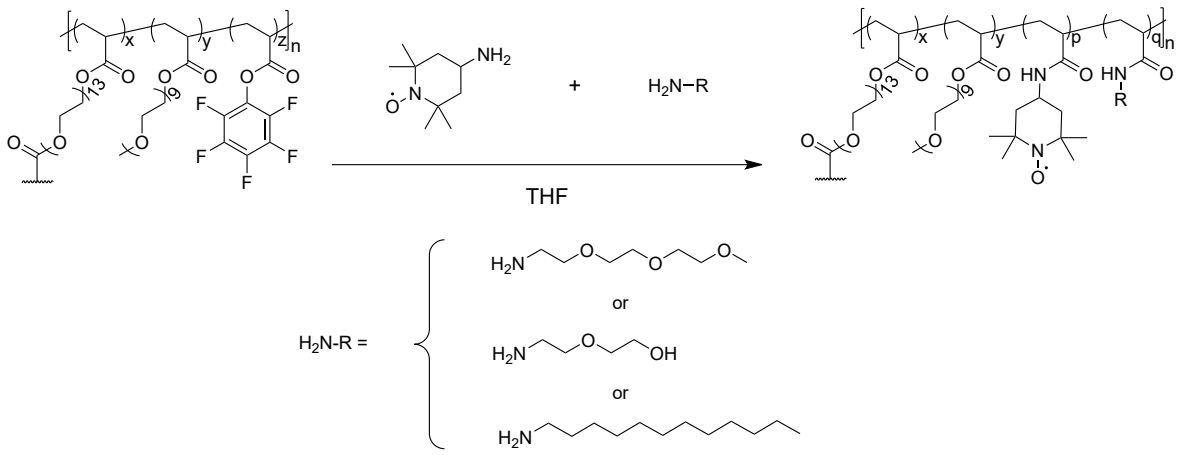
Figure 4.3. Water diffusivity from ODNP and PFG-NMR measurements as a function of water volume fraction in cross-linked PEGDA. (a) Overview of property differences between low molecular weight PEG solutions (upper left) and PEGDA networks (upper right) with network structure and spin label cartoons for PEGDA hydrogels (lower right and left respectively). (b) PFG-NMR water diffusion coefficients in cross-linked PEGDA (blue closed squares) and in PEG solution (green closed triangles) demonstrate water dynamics increase with increasing water volume fraction. (c) ODNP water diffusion coefficients in PEGDA networks (red open circles) and PFG-NMR in PEGDA networks (blue closed squares). PEGDA networks with higher water volume fractions allow for faster water transport local to the network chains (ODNP) and throughout the hydrogel (PFG-NMR) in qualitative agreement.

Critical to understanding this data is an appreciation of the vastly different observation length scales of ODNP and PFG-NMR, and non-ideal network topology of PEGDA networks. Our ODNP data here suggests water diffuses at approximately the same rate as PFG-NMR diffusivities within PEGDA networks, and spin labels sample water which is solution-like in its diffusion. This is in contrast to the findings in our previous study of water diffusion near linear, low-molecular weight PEG in aqueous solutions, where water dynamics observed by ODNP, local to the polymer backbone, were significantly *slowed* near the chain end (**Appendix C**).[39] Indeed, the ODNP water dynamics are approximately two times faster in cross-linked PEGDA networks than in non-cross-linked PEG solutions at the same nominal water content (**Figure C.8**). These results, while unexpected, show that water near the polymer network surface achieves comparable diffusivities as observed in PFG-NMR. Moreover, these results suggest that this local water diffusivity is tied to polymer chemistry and structure, rather than water movement *via* defects in network topology. Work from Malo de Molina[34] and others[35–37,55–57] have demonstrated that PEGDA networks display non-ideal network structures with fractal or star-like microstructures, and comparable features are expected in our materials. These reports elucidate the impact of topology and macromolecular

crosslinkers on physical properties, leading to significant deviations from the expected swelling behavior, as well as increased local rigidity the near high functionality, junction-like crosslinking sites. While we anticipate that these irregular network structures could impact water motion by changing local crosslink density, such effects would occur on length scales appreciably smaller than the micrometer length scales measured *via* PFG-NMR, and their influence would be washed out over the milliseconds timescale of measurement. However, even when we zoom in on the polymer network surface and sample water motion within the 1 nm scale radius observed by ODNP, we still observe comparably fast water diffusion. Consequentially, present ODNP diffusivities suggest that water motion near the hydrated polymer surface is relatively unhindered and is a feature of PEGDA's unique chemical identity, rather than purely an effect of water movement through defects in network structure. While these present results are encouraging, further research is needed to elucidate both the exact transport mechanism and the impact of polymer surface chemistry on water structuring and diffusivity *via* selective localization of spin probes in various chemical environments of the network.

Local water dynamics were further modulated by incorporation of side chain chemical groups within controlled PEGDA networks environments. The active ester chemistry employed in our material platform is easily amenable to investigate this connection and enables comparisons of sidechain chemistries with the significant benefit of a consistent network structure and backbone monomer across all samples.[5] Through modification of flow rate and fluorous phase in the above plug flow approach (**Appendix C**), the active ester monomer (c.a. ~20 mol%) could be incorporated into the network, verified by FTIR spectroscopy measurement, and for a range of diacrylate crosslinker contents (1.7 mol%, 7

mol%, and 16 mol%), amidated with one or more amino derivatives. Through co-reaction with a mixture of amino-TEMPO and a hydrophilic or a hydrophobic amine, particles with varied crosslinker composition, water content, and sidechain chemistry were prepared. A key benefit of this synthetic strategy is the ability to examine the impact of sidechain chemistry on water diffusivity in networks of the same topology and crosslinker content. The stability of the active ester group allows large parent batches of crosslinked particles to be synthesized, and then libraries of samples with the same network structure and backbone prepared *via* substitution with various mixtures of amino-TEMPO and hydrophilic or hydrophobic derivatives. Hydrophilic oligo-ethylene glycol amines or hydrophobic lauryl amines can be installed by reacting with amino-TEMPO and controlling the relative stoichiometry of each amino derivative (**Scheme 4.2**). Hydrophilic amines, diethylene glycol amine (DEG) and triethylene glycol ether amine (oligo-PEG), were selected to provide two key comparisons of a hydrophilic moiety containing a pendant hydroxy group (DEG) as a hydrogen bonding donor and acceptor, and a control (oligo-PEG) with comparable functionality to the ether terminated PEG-acrylate monomer. While these moieties are expected to have comparable water dynamics behavior, the oligo-PEG-amine allows for comparisons of near equivalent functionalities to the acrylate monomer without concerns of pendant hydroxyls reacting at active ester sites. The chain length of the oligo-PEG-amine is noted to be shorter than the PEG-acrylate monomer.



Scheme 4.2. Sub-stoichiometric, simultaneous reaction of TEMPO amine and either hydrophilic or hydrophobic amines at active ester sites within PEGDA microparticles.

PFG-NMR measurements on bulk PEGDA hydrogel strips with hydrophobic or hydrophilic sidechain groups incorporated were then performed. **Figure 4.4a** shows that, as with the un-functionalized networks, each functionalized network shows increasing water diffusion with increasing water volume fraction. PFG-NMR water diffusion coefficients in all three chemically functionalized PEGDA networks fall roughly on the same line with water content, in close agreement with the original, un-functionalized networks (*c.f.* **Figure 4.3**). While the hydrophobic lauryl-functionalized PEGDA networks give slightly lower bulk water diffusivities than the hydrophilic-functionalized PEGDA networks, the data collapses onto a single trendline by accounting for variations due to the effect of the functional groups on swelling behavior.

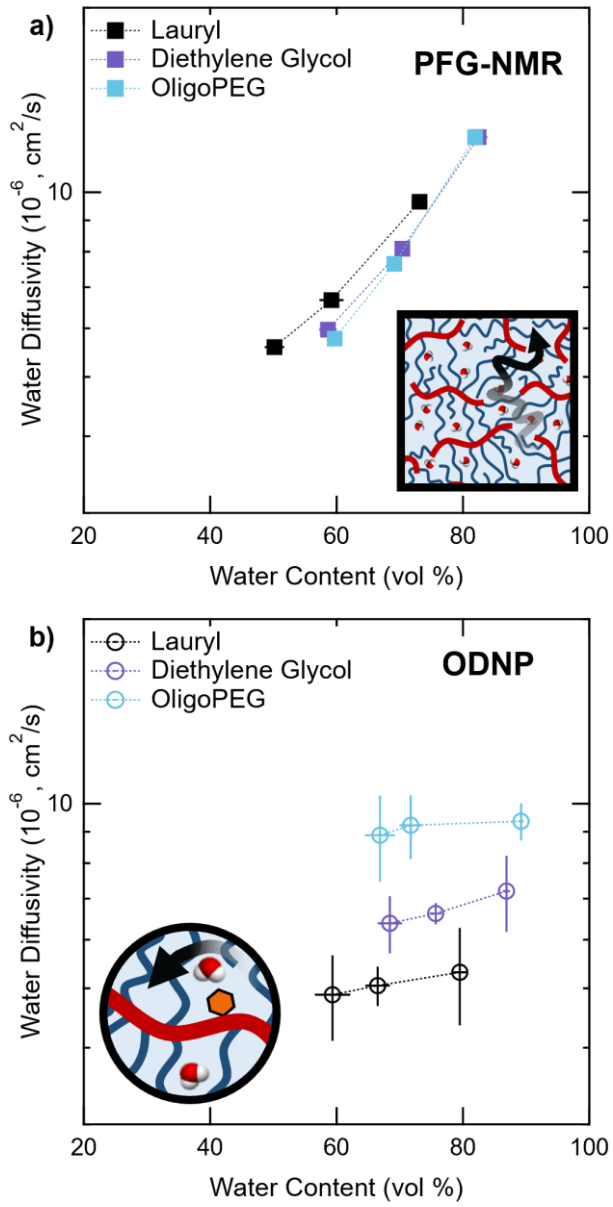


Figure 4.4. Water diffusion coefficients in cross-linked and spin-labeled PEGDA networks with a hydrophobic (lauryl amine, black data) or a hydrophilic (diethylene glycol amine, purple data, or an oligomeric PEG amine, blue data) functional group, prepared by simultaneous substitution with PFPA groups, measured by (a) PFG-NMR and (b) ODNP spectroscopy with inset cartoons depicting respective water motion. We observe no significant effect of local chemical groups on PFG-NMR bulk water diffusion coefficients, but slightly faster ODNP-measured local water

Figure 4.4b shows ODNP local water diffusion coefficients for cross-linked, spin-labeled PEGDA network microparticles of the same network composition and functionalization chemistries to determine if any local chemical effects emerge at smaller length scales. Indeed, we show that oligo PEG-functionalized networks exhibit faster water motion than the un-functionalized networks at all water contents (*c.f.* **Figure 4.3b**), while the DEG-functionalized networks exhibit water diffusivities in agreement with the un-functionalized networks. These effects may be due in part to slight changes in network structure as a result of higher active ester content and comonomer reactivity differences[51], as well as the reduced occupied volume of the shorter oligo-PEG chains relative to the PEG-acrylate, diluent monomer. We also note that the added functional groups bias the water volume fraction as they directly affect network swelling (see **Appendix C** for water swelling data in functionalized PEGDA networks). In contrast, the hydrophobic lauryl-functionalized PEGDA networks exhibit slower water motion local to the spin labels. This is consistent with observations from literature which show that water slows down near small length-scale (nanometer) nonpolar interfaces.[40,58–61] The addition of hydrophobic functional groups decreases water swelling in the networks. It should be noted that the ODNP data does not collapse entirely onto one trendline as with the PFG-NMR data. This indicates that a purely geometric water volume argument does not account entirely for changes in ODNP water dynamics, and that local chemical interactions play a role in mediating water dynamics in PEGDA networks.

We conclude that the local effects of these chemical modifications are confined to nanometer-length scale water dynamic observations, leaving only water volume fraction as the predictor for macroscopic water diffusion in cross-linked PEGDA networks. This supports

widely adopted diffusion models for transport in cross-linked PEGDA, which describe macroscopic diffusion as a function of volumetric water content. Significantly, the ODNP studies suggest that it is possible to chemically control and program surface water dynamics and local water-mediated interactions, such as solute capture and fouling near surfaces. For example, we expect that the increase in organic fouling near hydrophobic surfaces may in part be due to the low entropic cost to replace slower local water which exhibits stronger water-water hydrogen bonds and enhanced tetrahedral structuring.[62,63] Thus, the proposed design rule for engineering antifouling polymer surfaces is the addition of hydrophilic surface functionalities, which increase the entropic barrier for organic fouling adsorption while maintaining fast bulk diffusion and high membrane permeation.

4.4 Methods

Additional information (*e.g.*, reagents, microfluidic parts, equipment utilized, etc.) as well as tabulated data (*e.g.*, diffusivity data, FTIR characterization, network composition, etc.) are included in **Appendix C.** Key experimental methods are provided here for ease and context for the reader.

Particle synthesis was conducted according to **Figure 4.1** and **Scheme 4.1**, from neat mixtures of monomers: an active ester monomer, (pentafluorophenyl acrylate, PFPA), a diacrylate crosslinker (poly(ethylene glycol) diacrylate, PEGDA, Mn 700), and a monofunctional diluent monomer (poly(ethylene glycol) methyl ether acrylate, PEGMEA, Mn 480). Initiation was done by UV irradiation (3 mW/cm^2) at 365 nm using 2,2-dimethoxy-2-phenylacetophenone as the photo-initiator (1 wt.%, DMPA). These mild conditions and

efficient photoinitiation led to effective polymerization and crosslinking of microparticle networks on short timescales appropriate for flow synthesis with short residence times (ca. 30 seconds). Amine installation at active ester sites was conducted with minor modifications to previous procedures[5,36,49], and additional details are included in **Appendix C**.

Network microparticles were prepared by concomitant flow of the monomer mixture and a fluorous oil (FC-40 or FC-70) through sections of narrow bore, 100-micron internal diameter PFA-Plus tubing (IDEX Health and Science), with flow driven by two separate Harvard Apparatus PhD Ultra syringe pumps operated in continuous injection. The reactor was configured from simple off the shelf parts available from IDEX Health and Science (details in **Appendix C**). In brief, the flow diagram in **Figure 4.1** shows the directions of flow for each respective phase. The organic phase ran directly into a 4-way connector, while the fluorous phase would be directed from the syringe pump, through a T-connector to split it into two lines, and reconnected with the organic phase at the 4-way connector, with both phases flowing out through the reactor tube.

In a representative procedure, monomer resin and fluorous phase would be withdrawn into two separate BD-Plastipak, gas-tight syringes (3 mL) and connected *via* Luer connections (IDEX Health and Sciences) to the reactor. The monomer syringe was then wrapped in foil to prevent stray light exposure. Flow would be initiated and allowed to equilibrate for 15-20 minutes, and stable plug morphology would be confirmed *via* a USB optical microscope camera of the reactor tube and outlet. See **Appendix C** for flow rates and additional parameters. A shielding box would then be placed around the reactor tube and UV lamp to reduce the risk of polymerization in the connectors and inlet lines, or residual monomer polymerization at the collection point at the reactor outlet. The UV lamp would then be turned

on, the system allowed to equilibrate for an additional 10 minutes, and then collection would be started with the outlet transferred to an acetone filled collection vial. To prepare sufficient volumes of particles, the system was allowed to run for many hours (*e.g.*, 6+ hours) and was observed to be stable even during overnight runs without clogging. Collection would then be terminated, the outlet switched to an acetone filled, waste collection vial, the lamp turned off, and the system allowed to purge. After flushing unreacted monomer, particles, and solvent for an additional 5 minutes, syringes could then be disconnected and reactor tubing, mixers, and connections cleaned with acetone *via* syringe.

Through this approach PEGDA microparticles could be prepared with varied network compositions, as detailed in **Tables C.1 and C.2**. Key to the success of this strategy was the selection of a highly inert fluorous phase (FC-40 or FC-70) which preferentially wets the fluoropolymer tubing walls, encapsulating the monomers into well controlled plugs, with minimal sidewall sticking. Moreover, the minimal miscibility of the carrier with acrylate monomers allows for simple workup, *via* separation and washing of microparticles to remove any residual unreacted monomers and carrier solvent (**Appendix C**).

Control, bulk, networks could be prepared by using the same monomer mixtures and photoinitiator content used for microparticles, followed by dispensing the resin between quartz plates, with film thickness controlled at 250 microns by spacers between the plates as outlined previously work[5,36]. Polymer network films could then be cured by UV irradiation (3 mW/cm^2, 30s) and functionalized following prior procedures adapted for microparticle networks.

Microscopy characterization of particle dry and wet dimensions was conducted to determine water content in microparticle networks building on existing literature procedures

for determining network water content[54]. Optical microscopy was conducted on a Keyence VHX-5000 Microscope operated in mixed transmission and surface illumination modes. Particle dimensions were determined through use of the Keyence's built in area detection software, and area detection was determined as a function of color saturation and contrast with the transparent background (glass) stage. To aid in facile detection of particles in the installed software suite, particles were stained with a 0.1 wt% erythrosine B solution in water rendering the particles bright pink. Particles were then dialyzed in fresh DI water three times until the solution was clear.

Water swollen particles were taken up in an aliquot of DI water, placed between a glass slide and cover slip, and measurement was conducted using the auto area detection function. Small corrections were made to remove visual artifacts, break up errantly detected clusters of particles (*e.g.*, two particles adjacent to each other), and remove incomplete particles cut off by the image bounds. No significant changes were made to particle bounding metrics by the software. Dimensions of particle width, length, cross sectional area, and perimeter were then extracted for multiple images per particle sample-set. Values were compiled and averaged to achieve final swollen dimensions and error for each sample set. Swollen samples were then removed from the microscope, the cover slip was removed from the sample, and samples were allowed to dry in air until no film of water remained. Particles were then fully dried in a vacuum chamber held below 200 mTorr overnight prior to dry dimension measurement. The same measurement protocols were used for dry and wet samples. Values were tabulated, averages and error computed, and finally water content could be calculated using **Equation 4.1**.

To ensure that the presence of dye molecules did not significantly impact the overall swelling and dimension of the microparticle networks, control studies were done to determine the impact of the dye with details in **Appendix C**. In brief, a parent batch of microparticles was split into two groups, a control (unstained group) and an erythrosine B (2′,4′,5′,7′-Tetraiodofluorescein disodium salt) stained group as per **Figure C.4**. Particle diameters in the control group and stained group were measured manually using the Keyence's image analysis software and values were tabulated. Auto area detection was then done for the stained group and particle diameters were extracted. Control study data indicates no significant differences in dimension were observed as a result of the dye inclusion, and automated area detection provides more consistent particle dimension measurement than manual image analysis.

Electron paramagnetic resonance (EPR) experiments were performed to determine spin label concentration and rotational correlation times on TEMPO spin-labeled, cross-linked PEGDA microparticles, as described above. PEGDA networks were synthesized with 0.5 – 0.8 mol% of TEMPO spin label, varied to keep spin concentration constant by compensating for volumetric swelling of the networks with different cross-linker compositions. The microparticles swelled in water to equilibrium before they were loaded into sample capillaries for EPR and ODNP characterization. The samples were loaded into capillaries (round quartz capillaries with 0.6 mm ID x 0.84 mm OD dimensions (Vitrocom, New Jersey, USA) cut to 20 mm in length) following the above described in **Appendix C**. This method provided the most consistent loading of the microparticles into EPR capillaries by microscope inspection and by EPR concentration assessment. The loaded capillaries were sealed on one end with Critoseal and on the other end with melted beeswax. The continuous wave (cw)-EPR spectra was obtained on an X-band (9.8 GHz) electromagnet with a Bruker EMXPlus spectrometer at

20 dB microwave attenuation. The magnetic field was centered at 3500 G and a sweep range of 200 G. The modulation frequency was 100 kHz with a modulation amplitude of 1.0 G. Spin concentration was determined by double integration of the dispersive spectrum and compared to a calibration curve generated by free 4-hydroxy-TEMPO spin labels of various concentrations in water. cw-EPR lineshape analysis to determine the rotational correlation time of the spin labels was conducted using Multicomponent software[64]. cw-EPR spectra and fitting results are shown in **Appendix C**.

Overhauser Dynamic Nuclear Polarization (ODNP) experiments were conducted on spin-labeled, cross-linked PEGDA microparticles suspended in and swollen with liquid water, prepared as described in **Appendix C**. Samples capillaries were loaded into a home-built NMR probe in a high sensitivity EPR resonator (Bruker ER 4119HS-LC) which was placed in the center of the magnetic field in an X-band (9.8 GHz) electromagnet. EPR experiments were performed with a Bruker EMXPlus spectrometer while NMR experiments were performed with a Bruker Avance III NMR console (Bruker, Massachusetts, USA). ^{1}H NMR measurements (tuned to 14.8 MHz) were performed during continuous wave EPR saturation on the center peak of the nitroxide EPR spectrum, at 3484 G. To control the sample temperature, dry air flowed over the sample capillary continuously at 18°C and 20 SCFH. Determination of the ^{1}H longitudinal relaxation time of water was acquired with no microwave irradiation with ($T_1(0)$) and without ($T_{1,0}(0)$) the spin label present. The cross-linked PEGDA microparticles without spin labels were prepared from the same parent batches of PFPA containing microparticles and instead reacted with a diamagnetic (*e.g.*, radical free) TEMPO analogue. Low PFPA content microparticles were initially substituted with 4-(aminomethyl)piperidine. To better match amine substituent reactivity in mixed substitution

films and networks, high-PFPA content microparticles and control bulk materials were substituted with 4-amino-2,2,6,6-tetramethylpiperidine (ATMP) and the respective hydrophilic or hydrophobic secondary amines at equivalent molar ratios. ATMP presents a good structural analogue to TEMPO but without the nitroxide radical and is expected to have comparable incorporation to TEMPO during substitution at active ester sites in mixed amine installations. ODNP hydration parameters such as the cross-relaxation rate k_σ, self-relaxation rate k_ρ, coupling factor ξ, and ODNP local water diffusivity D_{ODNP} were calculated using DNPLab[65], a Python-based software package. Further details on the ODNP theory, experiment, and data analysis are described thoroughly in previous work.[41–44]

Hydrated membranes samples were prepared for NMR measurement by slicing the hydrated membranes into equivalent strips about 1 mm wide and packed into an NMR tube, which was sealed with parafilm. NMR measurements were performed at 20 ℃ on a Bruker Avance III 300 spectrometer with a 7.05 T super-wide bore (150 mm) superconducting magnet equipped with a Bruker DiffBB probe (maximum gradient strength of 17 T m^{-1}), operating at 300.15 MHz for ^{1}H. Dry N_2 was pumped into the probe at a flow rate of 800 L h^{-1} to control temperature. Recycle delays for all experiments were calibrated such that all nuclear spins relaxed to thermal equilibrium between scans (>5 × T_1) and π/2 pulses were calibrated to be 7.75 μs (32.3 kHz). The stimulated-echo pulse sequence was used for all measurements of self-diffusion coefficients, *D,* with 16 logarithmic-scaled steps from low to high gradient strengths. The data were fit to mono-exponential decays using the Stejskal-Tanner equation (**Equation 4.2**), here *I(g)* represents the signal intensity as a function of gradient strength, *g*, I_0 is the initial signal intensity, γ is the gyromagnetic ratio, δ is the

gradient pulse length, and Δ is the diffusion time. The diffusion data were processed and analyzed in Topspin 4.3.0.

Equation 4.2. Stejskal-Tanner equation utilized for PFG-NMR studies.

$$\frac{I(g)}{I_0} = e^{-(\gamma\delta g)^2\left(\Delta-\frac{\delta}{3}\right)D}$$

4.5 Conclusions and Future Work

This work demonstrates a methodology for measuring *in situ* nanoscale water dynamics *via* ODNP in cross-linked PEGDA network microparticles with varied water content and sidechain chemistry. By varying the composition of diacrylate crosslinker and utilizing plug-flow synthesis, well-defined microparticles with a wide range of water contents (40 – 90 vol%) can be prepared in a scalable manner, in comparison to bulk networks of the same composition. ODNP diffusivity measurements of PEGDA microparticle networks yield water diffusivity trends which correlate to those observed in PFG-NMR, namely increasing diffusivity with increasing water content in the hydrogel. PEGDA is a material that exhibits rapid, solution-like water diffusivities due to its hydrophilicity and high water content and despite the presence of a solid network structure. We further show that libraries of derivatized microparticles can be prepared from parent systems using active ester containing monomers to tune the network water content and hydrophilicity through reaction of the active ester groups with various amines, allowing for controlled incorporation of hydrophilic or

hydrophobic moieties. Again, using ODNP we show that hydrophobic groups both decrease the water content in the network as well as the local water diffusivity in the vicinity of the polymer backbone relative to hydrophilic substituents and control PEG-acrylate networks. This observation agrees with previous work on nonpolar interfaces and builds greater molecular understanding of water diffusivity in PEG-acrylate hydrogels. Interestingly, PFG-NMR demonstrates that the distinct local effects of these chemical groups become diminished during diffusivity measurements at longer length scales, leading to minimal impact on macroscopic diffusivity for materials of comparable water content. The ability to prepare libraries of well-defined crosslinked systems demonstrates the effect of network chemistry on local water dynamics and opens significant new possibilities for future studies with varied backbone chemistry and cross linking. The consistent network structure between samples will also enable modeling of different diffusion theories and structure-property relationships. These results offer critical insight and a roadmap into the molecular design of highly permeable coatings for water treatment membranes engineered for advanced separations.

4.6 References

(1) Sujanani, R.; Landsman, M. R.; Jiao, S.; Moon, J. D.; Shell, M. S.; Lawler, D. F.; Katz, L. E.; Freeman, B. D. Designing Solute-Tailored Selectivity in Membranes: Perspectives for Water Reuse and Resource Recovery. *ACS Macro Lett.* **2020**, *9* (11), 1709–1717. https://doi.org/10.1021/acsmacrolett.0c00710.

(2) Warnock, S. J.; Sujanani, R.; Zofchak, E. S.; Zhao, S.; Dilenschneider, T. J.; Hanson, K. G.; Mukherjee, S.; Ganesan, V.; Freeman, B. D.; Abu-Omar, M. M.; Bates, C. M. Engineering Li/Na Selectivity in 12-Crown-4–Functionalized Polymer Membranes. *Proc. Natl. Acad. Sci.* **2021**, *118* (37), e2022197118. https://doi.org/10.1073/pnas.2022197118.

(3) Landsman, M. R.; Sujanani, R.; Brodfuehrer, S. H.; Cooper, C. M.; Darr, A. G.; Davis, R. J.; Kim, K.; Kum, S.; Nalley, L. K.; Nomaan, S. M.; Oden, C. P.; Paspureddi, A.; Reimund, K. K.; Rowles, L. S.; Yeo, S.; Lawler, D. F.; Freeman, B. D.; Katz, L. E. Water Treatment: Are Membranes the Panacea? *Annu. Rev. Chem. Biomol. Eng.* **2020**, *11* (1), 559–585. https://doi.org/10.1146/annurev-chembioeng-111919-091940.

(4) Miller, D. J.; Dreyer, D. R.; Bielawski, C. W.; Paul, D. R.; Freeman, B. D. Surface Modification of Water Purification Membranes. *Angew. Chem. Int. Ed.* **2017**, *56* (17), 4662–4711. https://doi.org/10.1002/anie.201601509.

(5) Moon, J. D.; Sujanani, R.; Geng, Z.; Freeman, B. D.; Segalman, R. A.; Hawker, C. J. Versatile Synthetic Platform for Polymer Membrane Libraries Using Functional Networks. *Macromolecules* **2021**, *54* (2), 866–873. https://doi.org/10.1021/acs.macromol.0c02414.

(6) de Rutte, J.; Dimatteo, R.; Archang, M. M.; van Zee, M.; Koo, D.; Lee, S.; Sharrow, A. C.; Krohl, P. J.; Mellody, M.; Zhu, S.; Eichenbaum, J. V.; Kizerwetter, M.; Udani, S.; Ha, K.; Willson, R. C.; Bertozzi, A. L.; Spangler, J. B.; Damoiseaux, R.; Di Carlo, D. Suspendable Hydrogel Nanovials for Massively Parallel Single-Cell Functional Analysis and Sorting. *ACS Nano* **2022**, *16* (5), 7242–7257. https://doi.org/10.1021/acsnano.1c11420.

(7) Aswathy, S. H.; Narendrakumar, U.; Manjubala, I. Commercial Hydrogels for Biomedical Applications. *Heliyon* **2020**, *6* (4), e03719. https://doi.org/10.1016/j.heliyon.2020.e03719.

(8) Cavallo, A.; Madaghiele, M.; Masullo, U.; Lionetto, M. G.; Sannino, A. Photo-Crosslinked Poly(Ethylene Glycol) Diacrylate (PEGDA) Hydrogels from Low Molecular Weight Prepolymer: Swelling and Permeation Studies. *J. Appl. Polym. Sci.* **2017**, *134* (2). https://doi.org/10.1002/app.44380.

(9) Browning, M. B.; Wilems, T.; Hahn, M.; Cosgriff-Hernandez, E. Compositional Control of Poly(Ethylene Glycol) Hydrogel Modulus Independent of Mesh Size. *J. Biomed. Mater. Res. A* **2011**, *98A* (2), 268–273. https://doi.org/10.1002/jbm.a.33109.

(10) Jongpaiboonkit, L.; King, W. J.; Lyons, G. E.; Paguirigan, A. L.; Warrick, J. W.; Beebe, D. J.; Murphy, W. L. An Adaptable Hydrogel Array Format for 3-Dimensional Cell

Culture and Analysis. *Biomaterials* **2008**, *29* (23), 3346–3356. https://doi.org/10.1016/j.biomaterials.2008.04.040.

(11) Chang, C.-W.; Spreeuwel, A. van; Zhang, C.; Varghese, S. PEG/Clay Nanocomposite Hydrogel: A Mechanically Robust Tissue Engineering Scaffold. *Soft Matter* **2010**, *6* (20), 5157–5164. https://doi.org/10.1039/C0SM00067A.

(12) Zhang, Y.; An, D.; Pardo, Y.; Chiu, A.; Song, W.; Liu, Q.; Zhou, F.; McDonough, S. P.; Ma, M. High-Water-Content and Resilient PEG-Containing Hydrogels with Low Fibrotic Response. *Acta Biomater.* **2017**, *53*, 100–108. https://doi.org/10.1016/j.actbio.2017.02.028.

(13) Chapla, R.; Alhaj Abed, M.; West, J. Modulating Functionalized Poly(Ethylene Glycol) Diacrylate Hydrogel Mechanical Properties through Competitive Crosslinking Mechanics for Soft Tissue Applications. *Polymers* **2020**, *12* (12), 3000. https://doi.org/10.3390/polym12123000.

(14) Mazzoccoli, J. P.; Feke, D. L.; Baskaran, H.; Pintauro, P. N. Mechanical and Cell Viability Properties of Crosslinked Low- and High-Molecular Weight Poly(Ethylene Glycol) Diacrylate Blends. *J. Biomed. Mater. Res. A* **2010**, *93A* (2), 558–566. https://doi.org/10.1002/jbm.a.32563.

(15) Morris, V. B.; Nimbalkar, S.; Younesi, M.; McClellan, P.; Akkus, O. Mechanical Properties, Cytocompatibility and Manufacturability of Chitosan:PEGDA Hybrid-Gel Scaffolds by Stereolithography. *Ann. Biomed. Eng.* **2017**, *45* (1), 286–296. https://doi.org/10.1007/s10439-016-1643-1.

(16) Daly, A. C.; Riley, L.; Segura, T.; Burdick, J. A. Hydrogel Microparticles for Biomedical Applications. *Nat. Rev. Mater.* **2020**, *5* (1), 20–43. https://doi.org/10.1038/s41578-019-0148-6.

(17) Kalakkunnath, S.; Kalika, D. S.; Lin, H.; Freeman, B. D. Segmental Relaxation Characteristics of Cross-Linked Poly(Ethylene Oxide) Copolymer Networks. *Macromolecules* **2005**, *38* (23), 9679–9687. https://doi.org/10.1021/ma051741t.

(18) Werber, J. R.; Osuji, C. O.; Elimelech, M. Materials for Next-Generation Desalination and Water Purification Membranes. *Nat. Rev. Mater.* **2016**, *1* (5), 1–15. https://doi.org/10.1038/natrevmats.2016.18.

(19) Sagle, A. C.; Van Wagner, E. M.; Ju, H.; McCloskey, B. D.; Freeman, B. D.; Sharma, M. M. PEG-Coated Reverse Osmosis Membranes: Desalination Properties and Fouling Resistance. *J. Membr. Sci.* **2009**, *340* (1), 92–108. https://doi.org/10.1016/j.memsci.2009.05.013.

(20) Kang, G.; Cao, Y.; Zhao, H.; Yuan, Q. Preparation and Characterization of Crosslinked Poly(Ethylene Glycol) Diacrylate Membranes with Excellent Antifouling and Solvent-Resistant Properties. *J. Membr. Sci.* **2008**, *318* (1), 227–232. https://doi.org/10.1016/j.memsci.2008.02.045.

(21) Kang, G.; Liu, Z.; Yu, H.; Cao, Y. Enhancing Antifouling Property of Commercial Polyamide Reverse Osmosis Membrane by Surface Coating Using a Brush-like Polymer Containing Poly (Ethylene Glycol) Chains. *Desalination Water Treat.* **2012**, *37* (1–3), 139–145. https://doi.org/10.1080/19443994.2012.661265.

(22) Kang, G.; Cao, Y. Development of Antifouling Reverse Osmosis Membranes for Water Treatment: A Review. *Water Res.* **2012**, *46* (3), 584–600. https://doi.org/10.1016/j.watres.2011.11.041.

(23) Tran, T. N.; Ramanan, S. N.; Lin, H. Synthesis of Hydrogels with Antifouling Properties As Membranes for Water Purification. *J. Vis. Exp. JoVE* **2017**, No. 122, 55426. https://doi.org/10.3791/55426.

(24) Ju, H.; Sagle, A. C.; Freeman, B. D.; Mardel, J. I.; Hill, A. J. Characterization of Sodium Chloride and Water Transport in Crosslinked Poly(Ethylene Oxide) Hydrogels. *J. Membr. Sci.* **2010**, *358* (1), 131–141. https://doi.org/10.1016/j.memsci.2010.04.035.

(25) Geise, G. M.; Paul, D. R.; Freeman, B. D. Fundamental Water and Salt Transport Properties of Polymeric Materials. *Prog. Polym. Sci.* **2014**, *39* (1), 1–42. https://doi.org/10.1016/j.progpolymsci.2013.07.001.

(26) Ju, H.; McCloskey, B. D.; Sagle, A. C.; Wu, Y.-H.; Kusuma, V. A.; Freeman, B. D. Crosslinked Poly(Ethylene Oxide) Fouling Resistant Coating Materials for Oil/Water Separation. *J. Membr. Sci.* **2008**, *307* (2), 260–267. https://doi.org/10.1016/j.memsci.2007.09.028.

(27) Destgeer, G.; Ouyang, M.; Wu, C.-Y.; Carlo, D. D. Fabrication of 3D Concentric Amphiphilic Microparticles to Form Uniform Nanoliter Reaction Volumes for Amplified Affinity Assays. *Lab. Chip* **2020**, *20* (19), 3503–3514. https://doi.org/10.1039/D0LC00698J.

(28) Li, W.; Zhang, L.; Ge, X.; Xu, B.; Zhang, W.; Qu, L.; Choi, C. H.; Xu, J.; Zhang, A.; Lee, H.; Weitz, D. A. Microfluidic Fabrication of Microparticles for Biomedical Applications. *Chem. Soc. Rev.* **2018**, *47* (15), 5646–5683. https://doi.org/10.1039/c7cs00263g.

(29) Wu, Y.-H.; Park, H. B.; Kai, T.; Freeman, B. D.; Kalika, D. S. Water Uptake, Transport and Structure Characterization in Poly(Ethylene Glycol) Diacrylate Hydrogels. *J. Membr. Sci.* **2010**, *347* (1), 197–208. https://doi.org/10.1016/j.memsci.2009.10.025.

(30) Galizia, M.; Paul, D. R.; Freeman, B. D. Liquid Methanol Sorption, Diffusion and Permeation in Charged and Uncharged Polymers. *Polymer* **2016**, *102*, 281–291. https://doi.org/10.1016/j.polymer.2016.09.010.

(31) Jang, E.-S.; Kamcev, J.; Kobayashi, K.; Yan, N.; Sujanani, R.; Dilenschneider, T. J.; Park, H. B.; Paul, D. R.; Freeman, B. D. Influence of Water Content on Alkali Metal Chloride Transport in Cross-Linked Poly(Ethylene Glycol) Diacrylate.1. Ion Sorption. *Polymer* **2019**, *178*, 121554. https://doi.org/10.1016/j.polymer.2019.121554.

(32) Jang, E.-S.; Kamcev, J.; Kobayashi, K.; Yan, N.; Sujanani, R.; Dilenschneider, T. J.; Park, H. B.; Paul, D. R.; Freeman, B. D. Influence of Water Content on Alkali Metal Chloride Transport in Cross-Linked Poly(Ethylene Glycol) Diacrylate.2. Ion Diffusion. *Polymer* **2020**, *192*, 122316. https://doi.org/10.1016/j.polymer.2020.122316.

(33) Dobyns, B. M.; Kim, J. M.; Beckingham, B. S. Multicomponent Transport of Methanol and Sodium Acetate in Poly(Ethylene Glycol) Diacrylate Membranes of Varied Fractional Free Volume. *Eur. Polym. J.* **2020**, *134*, 109809. https://doi.org/10.1016/j.eurpolymj.2020.109809.

(34) Malo de Molina, P.; Lad, S.; Helgeson, M. E. Heterogeneity and Its Influence on the Properties of Difunctional Poly(Ethylene Glycol) Hydrogels: Structure and Mechanics. *Macromolecules* **2015**, *48* (15), 5402–5411. https://doi.org/10.1021/acs.macromol.5b01115.

(35) Wu, B.; Chassé, W.; Peters, R.; Brooijmans, T.; Dias, A. A.; Heise, A.; Duxbury, C. J.; Kentgens, A. P. M.; Brougham, D. F.; Litvinov, V. M. Network Structure in Acrylate Systems: Effect of Junction Topology on Cross-Link Density and Macroscopic Gel Properties. *Macromolecules* **2016**, *49* (17), 6531–6540. https://doi.org/10.1021/acs.macromol.6b01070.

(36) Shannon, D. P.; Moon, J. D.; Barney, C. W.; Sinha, N. J.; Yang, K.-C.; Jones, S. D.; Garcia, R. V.; Helgeson, M. E.; Segalman, R. A.; Valentine, M. T.; Hawker, C. J. Modular Synthesis and Patterning of High-Stiffness Networks by Postpolymerization Functionalization with Iron–Catechol Complexes. *Macromolecules* **2023**, *56* (6), 2268–2276. https://doi.org/10.1021/acs.macromol.2c02561.

(37) Borges, F. T. P.; Papavasiliou, G.; Teymour, F. Characterizing the Molecular Architecture of Hydrogels and Crosslinked Polymer Networks beyond Flory–Rehner—I. Theory. *Biomacromolecules* **2020**, *21* (12), 5104–5118. https://doi.org/10.1021/acs.biomac.0c01256.

(38) Nordness, O.; Moon, J. D.; Marioni, N.; Zofchak, E. S.; Richardson, P. M.; Landsman, M. R.; Katz, L. E.; Hawker, C. J.; Ganesan, V.; Segalman, R. A.; Clément, R. J. Probing Water and Ion Diffusion in Functional Hydrogel Membranes by PFG-NMR. *Macromolecules* **2023**, *56* (12), 4669–4680. https://doi.org/10.1021/acs.macromol.3c00306.

(39) Moon, J. D.; Webber, T. R.; Robinson Brown, D.; Richardson, P. M.; Casey, T. M.; Segalman, R. A.; Shell, M. S.; Han, S. Nanoscale Water–Polymer Interactions Tune Macroscopic Diffusivity of Water in Aqueous Poly(Ethylene Oxide) Solutions. *Chem. Sci.* **2024**. https://doi.org/10.1039/D3SC05377F.

(40) Jiao, S.; Rivera Mirabal, D. M.; DeStefano, A. J.; Segalman, R. A.; Han, S.; Shell, M. S. Sequence Modulates Polypeptoid Hydration Water Structure and Dynamics. *Biomacromolecules* **2022**. https://doi.org/10.1021/acs.biomac.1c01687.

(41) Franck, J. M.; Pavlova, A.; Scott, J. A.; Han, S. Quantitative Cw Overhauser Effect Dynamic Nuclear Polarization for the Analysis of Local Water Dynamics. *Prog. Nucl. Magn. Reson. Spectrosc.* **2013**, *74*, 33–56. https://doi.org/10.1016/j.pnmrs.2013.06.001.

(42) Franck, J. M.; Han, S. Chapter Five - Overhauser Dynamic Nuclear Polarization for the Study of Hydration Dynamics, Explained. In *Methods in Enzymology*; Wand, A. J., Ed.; Biological NMR Part B; Academic Press, 2019; Vol. 615, pp 131–175. https://doi.org/10.1016/bs.mie.2018.09.024.

(43) Franck, J. M.; Ding, Y.; Stone, K.; Qin, P. Z.; Han, S. Anomalously Rapid Hydration Water Diffusion Dynamics Near DNA Surfaces. *J. Am. Chem. Soc.* **2015**, *137* (37), 12013–12023. https://doi.org/10.1021/jacs.5b05813.

(44) Barnes, R.; Sun, S.; Fichou, Y.; Dahlquist, F. W.; Heyden, M.; Han, S. Spatially Heterogeneous Surface Water Diffusivity around Structured Protein Surfaces at Equilibrium. *J. Am. Chem. Soc.* **2017**, *139* (49), 17890–17901. https://doi.org/10.1021/jacs.7b08606.

(45) Cheng, C.-Y.; Varkey, J.; Ambroso, M. R.; Langen, R.; Han, S. Hydration Dynamics as an Intrinsic Ruler for Refining Protein Structure at Lipid Membrane Interfaces. *Proc. Natl. Acad. Sci.* **2013**, *110* (42), 16838–16843. https://doi.org/10.1073/pnas.1307678110.

(46) Schrader, A. M.; Monroe, J. I.; Sheil, R.; Dobbs, H. A.; Keller, T. J.; Li, Y.; Jain, S.; Shell, M. S.; Israelachvili, J. N.; Han, S. Surface Chemical Heterogeneity Modulates Silica Surface Hydration. *Proc. Natl. Acad. Sci. U. S. A.* **2018**, *115* (12), 2890–2895. https://doi.org/10.1073/pnas.1722263115.

(47) Moon, H.; Collanton, R. P.; Monroe, J. I.; Casey, T. M.; Shell, M. S.; Han, S.; Scott, S. L. Evidence for Entropically Controlled Interfacial Hydration in Mesoporous Organosilicas. *J. Am. Chem. Soc.* **2022**, *144* (4), 1766–1777. https://doi.org/10.1021/jacs.1c11342.

(48) DeStefano, A. J.; Nguyen, M.; Fredrickson, G. H.; Han, S.; Segalman, R. A. Design of Soft Material Surfaces with Rationally Tuned Water Diffusivity. *ACS Cent. Sci.* **2023**, *9* (5), 1019–1024. https://doi.org/10.1021/acscentsci.3c00208.

(49) Ulrich, S.; Sadeghpour, A.; Rossi, R. M.; Bruns, N.; Boesel, L. F. Wide Range of Functionalized Poly(*N* -Alkyl Acrylamide)-Based Amphiphilic Polymer Conetworks via Active Ester Precursors. *Macromolecules* **2018**, *51* (14), 5267–5277. https://doi.org/10.1021/acs.macromol.8b00841.

(50) Alex, J.; Ulbrich, J.; Rosales-Guzmán, M.; Weber, C.; Schubert, U. S.; Guerrero-Sanchez, C. Kinetic Investigations on Homo- and Co-Polymerizations of Pentafluorophenyl (Meth)Acrylates. *Eur. Polym. J.* **2021**, *143*, 110175. https://doi.org/10.1016/j.eurpolymj.2020.110175.

(51) Beija, M.; Li, Y.; Lowe, A. B.; Davis, T. P.; Boyer, C. Factors Influencing the Synthesis and the Post-Modification of PEGylated Pentafluorophenyl Acrylate Containing Copolymers. *Eur. Polym. J.* **2013**, *49* (10), 3060–3071. https://doi.org/10.1016/j.eurpolymj.2013.05.003.

(52) He, L.; Shang, J.; Theato, P. Preparation of Dual Stimuli-Responsive Block Copolymers Based on Different Activated Esters with Distinct Reactivities. *Eur. Polym. J.* **2015**, *69*, 523–531. https://doi.org/10.1016/j.eurpolymj.2015.01.045.

(53) Das, A.; Theato, P. Activated Ester Containing Polymers: Opportunities and Challenges for the Design of Functional Macromolecules. *Chem. Rev.* **2016**, *116* (3), 1434–1495. https://doi.org/10.1021/acs.chemrev.5b00291.

(54) Moon, J. D.; Galizia, M.; Borjigin, H.; Liu, R.; Riffle, J. S.; Freeman, B. D.; Paul, D. R. Water Vapor Sorption, Diffusion, and Dilation in Polybenzimidazoles. *Macromolecules* **2018**, *51* (18), 7197–7208. https://doi.org/10.1021/acs.macromol.8b01659.

(55) Sommer, J. -U.; Vilgis, T. A.; Heinrich, G. Fractal Properties and Swelling Behavior of Polymer Networks. *J. Chem. Phys.* **1994**, *100* (12), 9181–9191. https://doi.org/10.1063/1.466673.

(56) Krzeminski, M.; Molinari, M.; Troyon, M.; Coqueret, X. Characterization by Atomic Force Microscopy of the Nanoheterogeneities Produced by the Radiation-Induced Cross-Linking Polymerization of Aromatic Diacrylates. *Macromolecules* **2010**, *43* (19), 8121–8127. https://doi.org/10.1021/ma101615k.

(57) Gao, Y.; Zhou, D.; Lyu, J.; A, S.; Xu, Q.; Newland, B.; Matyjaszewski, K.; Tai, H.; Wang, W. Complex Polymer Architectures through Free-Radical Polymerization of Multivinyl Monomers. *Nat. Rev. Chem.* **2020**, *4* (4), 194–212. https://doi.org/10.1038/s41570-020-0170-7.

(58) Seto, T.; Mashimo, T.; Yoshiya, I.; Shimizu, A.; Fumino, K.; Taniguchi, Y. NMR Studies on Dynamic Structure of Hydrated Water Molecules in Alcohol-D2 O Solutions. *J. Mol. Liq.* **1996**, *70* (1), 1–9. https://doi.org/10.1016/0167-7322(96)00951-8.

(59) Russo, D.; Murarka, R. K.; Copley, J. R. D.; Head-Gordon, T. Molecular View of Water Dynamics near Model Peptides. *J. Phys. Chem. B* **2005**, *109* (26), 12966–12975. https://doi.org/10.1021/jp051137k.

(60) Qvist, J.; Halle, B. Thermal Signature of Hydrophobic Hydration Dynamics. *J. Am. Chem. Soc.* **2008**, *130* (31), 10345–10353. https://doi.org/10.1021/ja802668w.

(61) Niehues, G.; Heyden, M.; A. Schmidt, D.; Havenith, M. Exploring Hydrophobicity by THz Absorption Spectroscopy of Solvated Amino Acids. *Faraday Discuss.* **2011**, *150* (0), 193–207. https://doi.org/10.1039/C0FD00007H.

(62) Robinson Brown, D. C.; Webber, T. R.; Jiao, S.; Rivera Mirabal, D. M.; Han, S.; Shell, M. S. Relationships between Molecular Structural Order Parameters and Equilibrium Water Dynamics in Aqueous Mixtures. *J. Phys. Chem. B* **2023**, *127* (20), 4577–4594. https://doi.org/10.1021/acs.jpcb.3c00826.

(63) Monroe, J. I.; Shell, M. S. Computational Discovery of Chemically Patterned Surfaces That Effect Unique Hydration Water Dynamics. *Proc. Natl. Acad. Sci.* **2018**, *115* (32), 8093–8098. https://doi.org/10.1073/pnas.1807208115.

(64) *altenbach - MultiComponent*. https://sites.google.com/site/altenbach/labview-programs/epr-programs/multicomponent (accessed 2024-05-07).

(65) *Welcome to DNPLab*. http://dnplab.net/ (accessed 2023-10-05).

Chapter 5. Conclusions

In summary, modular design of polymer networks via post polymerization modification with active ester chemistry presents a facile method to prepare designer materials for a diverse range of applications. The pentafluorophenyl acrylate (PFPA) active ester network platform was leveraged in Chapter 2 to conduct facile installation of dopamine into PEG-acrylate networks, crucially without the need for protection or deprotection chemistry. Such approaches enabled large scale preparation of catechol functionalized network materials through simple wash procedures on multi-gram scale without oxidation of sensitive catechol moieties, and the complexation of catechol motifs with Fe^{3+} salts demonstrated the ability to tune mechanical properties over a wide range of elastic moduli, spanning two orders of magnitude. This was demonstrated in a range of approaches, either through tuning the catechol content of the patent network, or via gradients in iron ion diffusion and complexation into the material. Moreover, these gradients in iron diffusion into the network could be exploited and combined with soft lithography techniques from the literature to prepare patterned materials with heterogeneous, composite like behavior in a continuous network sample. This approach provides a user-friendly strategy for preparing bespoke materials with an array of tunable and localizable mechanical behavior and enables the development of novel materials for potential applications in soft robotics and bioinspired composite systems, though further research is required.

Building on the concepts developed in preparation of catechol functionalized materials, these approaches could be extended to prepare novel hydroxypyridinone (HOPO) containing networks, as detailed in Chapter 3. HOPO motifs offer many of the same advantageous metal-chelation behaviors of catechol analogues, but without their concomitant

drawbacks in oxidation, presenting an enticing motif to incorporate into network polymers. To leverage the PFPA active ester network platform, an amine terminated HOPO ligand was designed, building upon recently developed boronic-acid chemistry to prepare the target material on multi-gram scale, in a one-pot approach. Functionalization of network materials could again be conducted in simple wash procedures, and HOPO motifs could be complexed with metal salts. Crucially, owing to the wider chelation scope of the HOPO ligand, networks were able to be complexed with both transition metal ions (Fe^{3+}) as well as lanthanide ions (Ho^{3+}, Tb^{3+}) to impart a diverse range of behaviors. While all metal ions were able to introduce significant enhancements in mechanical properties, the inherent paramagnetic nature and fluorescent nature of lanthanide species could be leveraged to prepare materials with added functionalities. Moreover, patterning approaches could be extended and expanded upon to incorporate one or more metal centers into HOPO functionalized networks. In the simple case of patterning one ion, it was demonstrated to prepare samples with mechanical and magnetic heterogeneity by localization and complexations of Ho^{3+} ions into the network. This was extended to prepare surface patterned samples *via* ion exchange into a Tb^{3+} chelated film, demonstrating localization of Fe^{3+}, Ho^{3+}, and Tb^{3+}, for control of mechanical, magnetic, and fluorescent properties. These approaches complement earlier work and further demonstrate the utility of this network platform for preparing bespoke materials. Moreover, present work provides further tools for preparing materials for soft robotics and materials scale applications through incorporation and localization of magnetic and fluorescent responses in addition to mechanical property control.

Lastly, this versatile network chemistry was extended for hydrogel systems to install electron paramagnetic resonance (EPR) active TEMPO motifs and a range of sidechain groups

into the network to conduct in-situ measurement of nanoscale water diffusivity and identify the impact of sidechain chemistry. By leveraging the fast, facile, free radical network polymerization of PFPA and PEG-acrylates, networks could be prepared as microparticles in a biphasic flow synthesis at a range of crosslinker and PFPA contents to control final material water content through network structure and chemistry. Moreover, through utilization of this approach, large batches of parent (PFPA) materials could be prepared and derivatized with amine terminated TEMPO and sidechain chemistries, without the need for protection/deprotection of TEMPO motifs and simultaneously maintaining network topology. This synthetic methodology allows for direct comparison of network functionality without limitations of changing network structure with changing pendant moieties, or repeated synthesis of microparticles. Fundamentally, this approach enabled effective preparation of microparticle networks with varied crosslinker and water contents for nanoscale measurements of water diffusivity at the polymer surface *via* Overhauser Dynamic Nuclear Polarization (ODNP, a combined EPR and NMR technique). In the simple case, measurement of water transport in networks with water content varied by crosslinker content, nanoscale water transport was observed to be solution-like in character and unhindered by the non-ideal PEGDA network architecture. Such measurements are in agreement with pulsed field gradient (PFG) nuclear magnetic resonance (NMR) measurements of networks with the same composition. Critically though, for materials with varied sidechain chemistry, nanoscale water diffusivities at the polymer surface were found to change with pendant motif while bulk (PFG) based diffusivities were unaffected, highlighting the crucial impact of network substituent chemistry on water diffusivity and transport. These results demonstrate an exciting step forward in understanding how chemical identity at the nanoscale impacts local water

behavior and provide fundamental insight for design rules in preparing next generation membrane materials.

To close, present work entailed in this thesis has demonstrated the versatility of active ester polymer networks as a tool for engineers and chemists to prepare bespoke materials with a range of tunable materials properties through post network polymerization modification of sidechain groups. This approach has enabled direct preparation of functional and patterned materials which would otherwise prove challenging due to their protection and deprotection chemistry, and it has further demonstrated the utility of easily preparing and derivatizing parent network materials without concerns of topological changes. As a whole, these methodologies present a facile way to screen and design network polymers for next generation materials systems.

Appendix A. Supporting Information for Chapter 2

Materials and Instrumentation

All chemicals were purchased and used as received. Poly(ethylene glycol diacrylate) (PEGDA, M_n 700, with inhibitor), poly(ethylene glycol methyl ether acrylate) (PEGMEA, M_n 480, with inhibitor), pentafluorophenol, acryloyl chloride (with inhibitor), dopamine hydrochloride salt, triethyl amine, and DMPA (2,2-dimethoxy-2-phenylacetophenone), were purchased from Sigma Aldrich and used as received. Bicine was purchased from TCI, and $Fe(NO_3)_3$ (nonahydrate, ACS reagent Grade) was purchased from Fischer Scientific (Acros Organics). Isopropanol, hexanes, methanol, and other solvents were procured from Sigma Aldrich and used as received without further drying or distillation, with the exception of DCM used in PFPA synthesis, which was dried via a PureSolv MD-5 dry solvent system.

Fourier Transform Infrared Spectroscopy with Attenuated Total Reflection (FTIR-ATR) analysis of polymer films was conducted on a Thermo Nicolet iS10 spectrometer equipped with a diamond ATR accessory using 64 scans. FTIR measurements were taken at room temperature under ambient atmosphere. Data were corrected using automatic baseline correction.

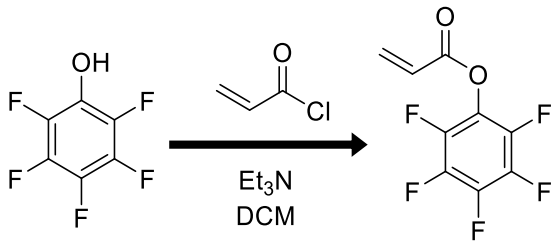
Raman Spectroscopy was conducted on cut film interior surfaces using a Horiba Jobin Yvon instrument with confocal microscopy and a 632 nm laser. Hole and slit sizes were both set to 500 microns, with 20 accumulations at 2 seconds each.

Optical microscopy images were taken on samples using a Keyence VHX-5000 optical (digital) microscope. Surface illumination was used unless otherwise specified.

Nuclear Magnetic Resonance (NMR) Spectroscopy measurements were collected on a Bruker 400 MHz NMR-Spectrometer in deuterated chloroform ($CDCl_3$).

PDMS sheeting used in masking procedures was obtained from B & J rubber products with mylar backing and a PDMS sheet thickness of 250 microns. Sheets were cut to the desired geometry using a Trotec Speedy 100 laser cutter. Acrylic panels and holders were laser cut using the same equipment.

Synthesis of PFPA Monomer



Scheme A.1. Synthesis of pentafluorophenyl acrylate (PFPA) monomer.

A revised version of prior synthetic procedure[1] was followed for PFPA synthesis. In short, pentafluorophenol (50 g, 0.27 mol) and Et_3N(40 mL, 0.29 mol) were dissolved in anhydrous DCM (700 mL) and cooled to 0 °C. In a separate flask, acryloyl chloride (24.5 mL, 0.303 mol) was dissolved in 50mL of anhydrous DCM and was added dropwise to cooled pentafluorophenol solution. The mixture was stirred and allowed to warm to room temperature overnight. The reaction was washed with 1M HCl (3x 300mL), then washed with concentrated

$NaHCO_3$ (2x 300mL), and dried over $MgSO_4$. The organic phase was then filtered through a layered plug of basic alumina and charcoal and allowed to sit with additional charcoal for 3 hours to remove yellow coloration, filtered, and then concentrated to obtain a clear oil (75% yield). 6.70 (d, *J*= 17.5Hz, 1 H), 6.36 (dd, 1 H), 6.18 (d, *J*=10.5 Hz, 1 H)

Polymer Network Synthesis

In a representative procedure of network preparation, DMPA as photoinitiator, PEGMEA, PFPA, and PEGDA were mixed and sonicated for 2 minutes. Monomer resin was dispensed between two quartz plates, with film thickness controlled by steel spacers placed between the plates. Samples were irradiated on one side with 365 nm UV (3 mW/cm^2 power density) for 2 minutes to crosslink the networks. Samples containing PFPA were then immediately placed into a degassed methanol solution containing excess dopamine hydrochloride salt (3 equivalents relative to PFPA), and Et_3N (1.5 equivalents relative to dopamine) was added to begin the catechol substitution. The reaction was gently stirred at room temperature under nitrogen sparging for 24 hours, and films were then placed in increasingly dilute HCl washes for 24 hours (0.1 M and 1 mM) to neutralize unreacted starting material and gradually adjust pH. Swollen films were stored in dilute HCl (1 mM).

Deswelling f Large Area Films

To prepare large area films for patterning and mechanical testing, a solvent deswelling procedure was developed. Films swollen in aqueous solutions frequently cracked during direct dehydration under vacuum, so a gentle solvent gradient was developed to slowly remove water from the networks. Water swollen films were placed into a solution with a 3:1 volumetric ratio

of DI water and isopropanol (IPA). IPA was gradually added to achieve a 2:1, 1:1, 1:2, and finally 1:3 volumetric ratio of water to IPA with 30 minutes to 1 hour between solvent additions depending on film thickness. Films were then transferred to pure IPA, and hexanes was added stepwise to achieve the same volumetric ratios. Films were then removed from the mixed organic solvent solution and dried directly in vacuum.

Bulk Iron Treatment of Catechol Films

Catechol substituted films were removed from their 1mM HCl storage solutions and blotted dry to remove excess solution. Films were then immediately transferred to a solution of 0.05 M $Fe(NO_3)_3$ and 0.2 M Bicine buffered with KOH to pH 7.5. Solution volume was adjusted to be in significant excess (>5×) of the iron content need to fully crosslink films. Unless otherwise noted, bulk samples were left in the iron treatment solution for 3 days. Samples were then removed, blotted dry, and placed into deionized (DI) water to remove residual salts. Films were dialyzed for 3 days with daily exchange of the DI solution, followed by the deswelling procedure described above.

Optical Microscopy Images of Fe^{3+}-Catechol Films with High PEGDA Content

Optical microscopy images in the main text (**Fig. 2.6**) were taken on cross-sectioned samples using a Keyence VHX-5000 optical (digital) microscope. Mixed transmission and surface illumination was used to highlight dark, opaque regions that were complexed with iron and more transparent regions that were relatively iron free. Samples were noted to have decreasing iron intrusion depths with increasing covalent crosslinker density at high catechol grafting densities.

Table A.1: Network compositions for high covalent crosslinker content films. Note, metal-ligand crosslinking ratio targets were not achieved through the bulk of the film due to limited iron diffusion.

Network Composition			**Theoretical Maximum Crosslink Density (mmol/cm^3)**			**Metal-Ligand to Covalent Crosslink Ratio**	**Iron Treat. Duration**
mol% Catechol	mol% PEGDA	mol% PEGMEA	Total Crosslink Density	Covalent Crosslink Density	Metal-Ligand Crosslink Density		
58%	3%	39%	1.10	0.10	1.00	10	6 days
59%	7%	33%	1.25	0.25	1.00	4.0	3 days
61%	15%	24%	1.50	0.50	1.00	2.0	3 days

Oxidation of Control Samples

To conduct control studies of intentionally oxidized films, a 0.05 M solution of $NaIO_4$ was prepared. Catechol containing films were removed from their 1 mM HCl dialysis, blotted dry, and placed in significant excess of the periodate solution (>5× excess mol. catechol groups). Samples were allowed to oxidize for 4 days, removed, and dialyzed in DI water for 24 hours before deswelling and drying. Note, caution should be exercised when handling strong oxidizers. Upon exposure to oxidizing conditions, films were noted to have an immediate color change from transparent to a light orange or yellow hue, deepening to the orange/red hues observed in **Figure A.1**.

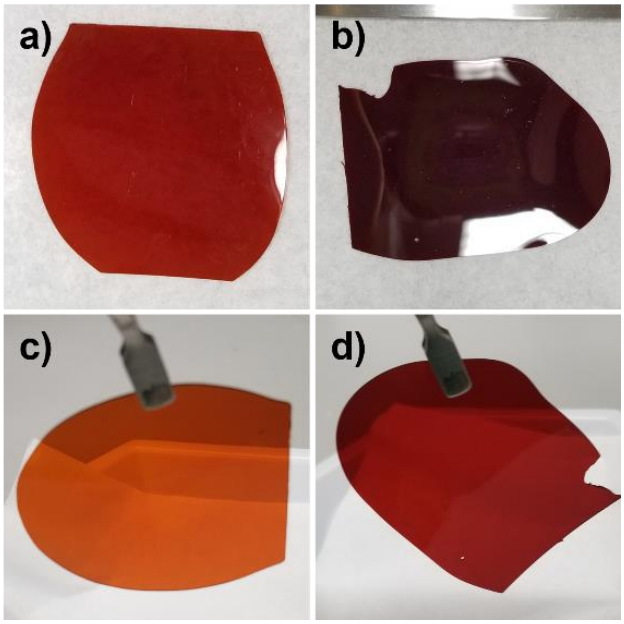


Figure A.1: Images of catechol films after oxidation with NaIO4. (a) 3.5 mol% / 35 mol% / 61 mol% PEGDA/catechol/PEGMEA network after oxidation with NaIO4, (b) 2.9 mol% / 58 mol% / 39 mol% PEGDA/catechol/PEGMEA network after oxidation with NaIO4 (c-d). Oxidized films held vertically to demonstrate transparency.

Fe^{3+} Patterning of Catechol Films

Patterning of iron-catechol domains could be conducted through a modified literature procedure from a solution-soaked filter paper[2] or directly from solution. For patterning from a soaked filter paper, catechol containing films were removed from a 1 mM HCl storage solution, placed against a glass slide and blotted dry of excess solution. The PDMS mask was then adhered to the film, completely covering the sample, and was then secured to a glass substrate to form an effective seal and prevent iron solution intrusion. The edges of the mask were then secured to the slide using Kapton tape to further prevent leakage. Next, a stack of 4 sheets of filter paper, soaked in the $Fe(NO_3)_3$ solution, was gently pressed against the masked catechol film. The entire assembly was then secured with a top glass slide and fixed in place

with binder clips. The assembled patterning holder was then submerged in the iron solution for the desired patterning duration.

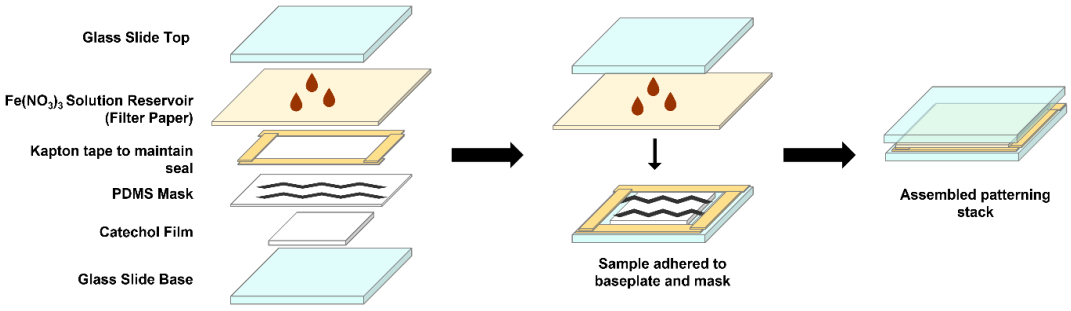


Figure A.2: Graphic depicting the components and setup for patterning catechol films from a soaked filter paper.

To pattern samples directly from solution, a similar PDMS masking approach was used, and films could be patterned from both sides. To pattern films from solution, a porous, rigid sample holder (**Figure A.3A**) was prepared from laser cut acrylic sheeting to allow the solution to reach the film surface. Two PDMS masks were laser cut for the front and back of the film, and a PDMS "spacer" of comparable thickness to the catechol film (c.a. 250 microns) was cut to act as a gasket to seal the film between the PDMS masks. To prepare the sample for patterning, one PDMS mask was adhered to the porous acrylic backing, then the PDMS spacer was placed on top of the mask forming a border around the edge of the sample holder (**Figure A.3B**). The catechol film was blotted dry and adhered to the mask on the sample holder, and the top mask was aligned and placed on the surface of the catechol film, sealing with the PDMS spacer below (**Figure A.3C**). The top porous acrylic holder was placed on the assembly (**Figure A.3D**), secured with binder clips, and submerged in iron solution for the

desired time period. The sample could then be removed (**Figure A.3E**), dialyzed, and opened (**Figure A.3F**) to reveal the patterned sample (**Figure A.3G**).

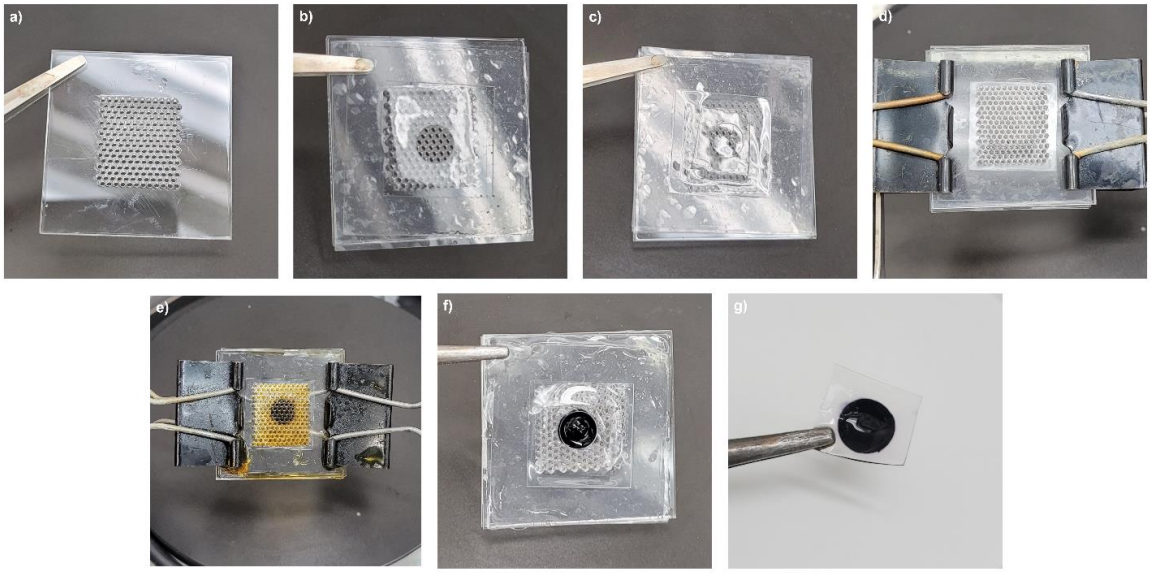


Figure A.3: Solution patterning holder assembly. (a) Laser cut, porous acrylic back panel, (b) adhered rear mask and gasket PDMS layers, (c) adhered catechol film and top mask layer, (d) top acrylic panel secured to stack with clips, (e) sample after immersion in iron solution, (f) sample after immersion in iron solution with top acrylic panel removed, (g) solution patterned sample.

Rheological Experimental Procedures and Results

Rheological measurements were made on an ARES-G2 strain-controlled rheometer manufactured by TA instruments. Stainless steel 8 mm parallel plates were used for all measurements. Rheology samples were prepared by using an 8 mm diameter die-punch to prepare flat, circular samples from vacuum dried films. Samples were placed on the rheometer and compressed at 90 °C and 5N of force. During operation all samples were enclosed in a nitrogen-purged oven chamber. Final sample thicknesses were maintained within a range of 0.5 mm. All measurements were made in the 'linear regime' as determined via strain sweep measurements. Temperature-dependent frequency measurements for time temperature

superposition were performed as a sequence of experiments with 5 minutes of soak time between steps. To investigate long-time responses of the materials, linear stress relaxation experiments were also performed. The glassy timescale of the material was determined using fitting to the phenomenological Kohlrausch-Williams-Watts (KWW) expression for the time-dependent modulus G(t). Fitting was performed in frequency space as described in our previous work[3] and utilized the 'libkww' library which provides an approximation for the Fourier transform of stretched exponential functions[4].

Rheological testing of Fe^{3+}-catechol networks at elevated temperatures revealed minimal stress relaxation during the timescale of beam bending (nominally ~5s, **Figure A.4**). These results indicate that during the timescale of beam bending testing, Fe^{3+}-catechol crosslinks behave as quasistatic crosslinks rather than dynamic linkages. To further evaluate the amount of stress relaxation relative to the crosslinked plateau modulus of the iron free network, frequency sweeps at varied temperatures were conducted to generate master curves from the time temperature super positions and the rubbery plateau was identified from (**Fig. A.5**). Even at extended timescales (1000s), samples do not relax to the value of the long timescale crosslinking plateau (**Figure A.5**).

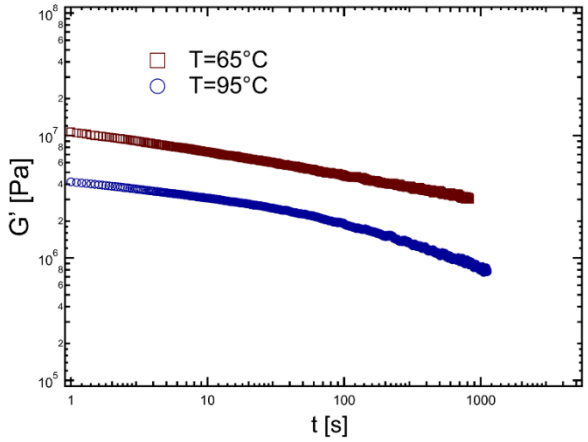


Figure A.4: Stress relaxation measurements at elevated temperature of a 2.9/39/58 mol% PEGDA/PEGMEA/catechol network after complexation with Fe^{3+}. Storage moduli of elevated temperature stress relaxation measurements at 65°C (red squares), and 95°C (blue circles) demonstrate minimal stress relaxation during the timescale of beam bending tests (nominally 5s).

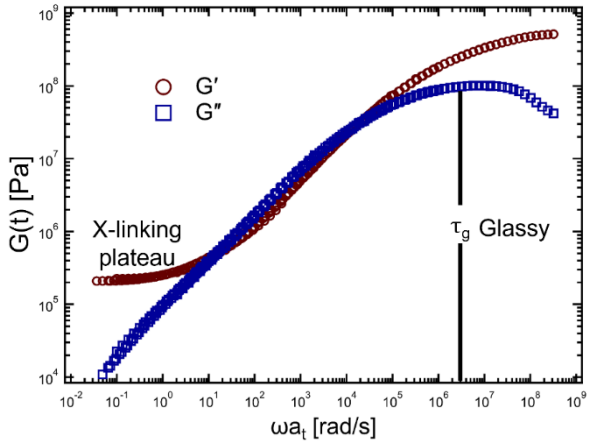


Figure A.5: Master curves of storage (red circles) and loss (blue squares) moduli from time temperature superposition *vs.* (shifted) frequency of iron free catechol network, with composition of 2.9/39/58 mol% PEGDA/PEGMEA/catechol, demonstrating expected crosslinking plateau and viscoelastic behavior.

Beam Bending Methods and Summary Data

Beam bending was conducted on sectioned samples. Three-point beam bending was performed on a TA.XT Plus Connect Texture Analyzer with a 50 N load cell. Samples were

cut into rectangular strips and deformed at a displacement rate of 0.1 mm/s to a turnaround force between 10 and 30 mN depending on sample stiffness. Beam spans were also altered between 15 and 25 mm to control sample stiffness. Summary data and an example plot showing these tests are shown in **Figure A.6** and **Tables A.2**, **A.3**, and **A.4**. Moduli were calculated according to **Equation A.1**, using the sample stiffness k, beam length L, beam width b, and beam height h according to the bending equation for a center loaded beam with simply supported ends[5].

$$E = \frac{kL^3}{4bh^3}$$

Equation A.1: Moduli calculation from the bending equation for a center loaded beam.

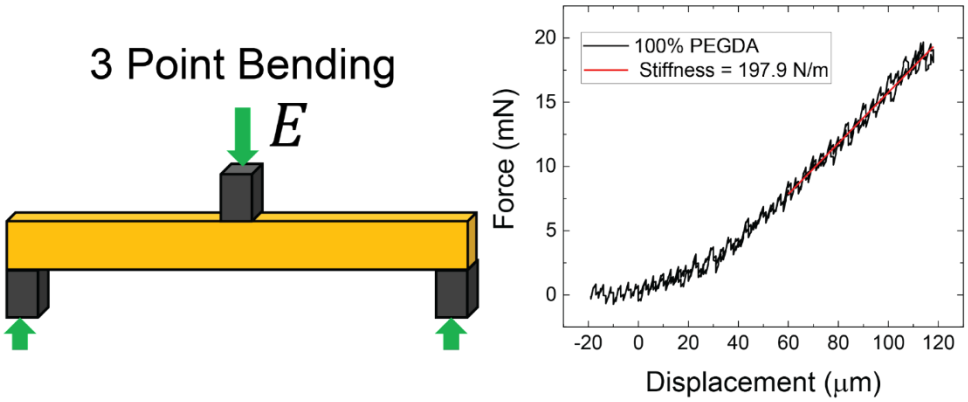


Figure A.6: (Left) Diagram of 3-point bending test and (right) example plot of force vs. displacement data (black) and curve fitting of sample stiffness in linear regime (red overlay trace).

Table A.2: Beam bending summary data of Fe^{3+}-Catechol films.*Note: Samples at this composition frequently cracked due to brittle nature of the film, resulting in insufficient surface area for multiple measurements

Network Composition	mol% Catechol	4.40%	20%	35%	48%	58%
	mol% PEGDA	4.40%	3.90%	3.50%	3.20%	2.90%
	mol% PEGMEA	91%	76%	61%	49%	39%
Theoretical Maximum Crosslink Density ($mmol/cm^3$)	Total Crosslink Density	0.15	0.35	0.6	0.85	1.1
	Covalent Crosslink Density	0.1	0.1	0.1	0.1	0.1
	Metal-Ligand Crosslink Density	0.05	0.25	0.5	0.75	1
Metal-Ligand to Covalent Crosslink Ratio		0.5	2.5	5	7.5	10
Young's Modulus, E,	**(MPa)**	2.7	10.2	30.3	46.5	245
Standard Deviation	**(MPa)**	--	1.2	2	8.5	26
Number of replicates,	**n**	1*	3	5	6	6

Table A.3: Beam bending summary data for control PEGDA/PEMGEA films

Network Composition		**Theoretical Maximum Crosslink Density ($mmol/cm^3$)**	**Young's Modulus, E, (MPa)**	**Standard Deviation (MPa)**	**Number of replicates, n**
mol% PEGDA	mol% PEGMEA				
4.5%	95.5%	0.1	1.7	0.7	6
12%	88%	0.25	5.2	0.7	4
24%	76%	0.50	9.2	1.0	7
54%	46%	1.0	16.3	0.9	4
100%	0%	1.6	28.4	3.2	7

Table A.4: Beam bending summary data of oxidized catechol films

Network Composition			**Young's Modulus, E, (MPa)**	**Standard Deviation (MPa)**	**Number of replicates, n**
mol% Catechol	mol% PEGDA	mol% PEGMEA			
35%	3.5%	61%	3.7	0.4	3
58%	2.9%	39%	28.4	5.5	3

SEM EDS Characterization of Fe^{3+} Content

Fe^{3+} distribution through the film was further characterized by scanning electron microscopy (SEM) using a ThermoFisher Apreo C with accelerating voltages of 5 keV. Flat cross sections were prepared by cutting the samples with a blade after quenching in liquid nitrogen. The samples were sputter-coated with 2-3 nm of platinum before imaging. The chemical compositions across the film were analyzed by line scan of energy-dispersive X-ray spectroscopy (EDS).

Iron diffusion gradients could be designed bulk samples (**Figure A.7**) or in surface patterned films (**Figure A.8**) through both temporal and directional control. During iron treatment of bulk catechol films, significant gradients in iron content from the film exterior to interior could be designed through short exposure to the Fe^{3+} solution, with increasing iron content until a homogenous film was achieved. Similarly, in a filter paper patterned sample, iron diffusion gradients could be designed to be directional from a single side of the film and intrusion into the film could be controlled through the duration of patterning.

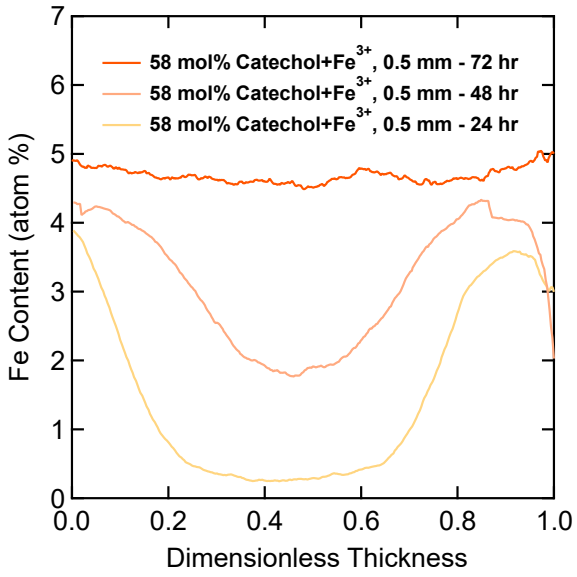


Figure A.7: SEM EDS characterization of Fe^{3+} distributions across film thicknesses in a 3/39/58 mol% PEGDA/PEGMEA/catechol film at various timepoints during iron treatment.

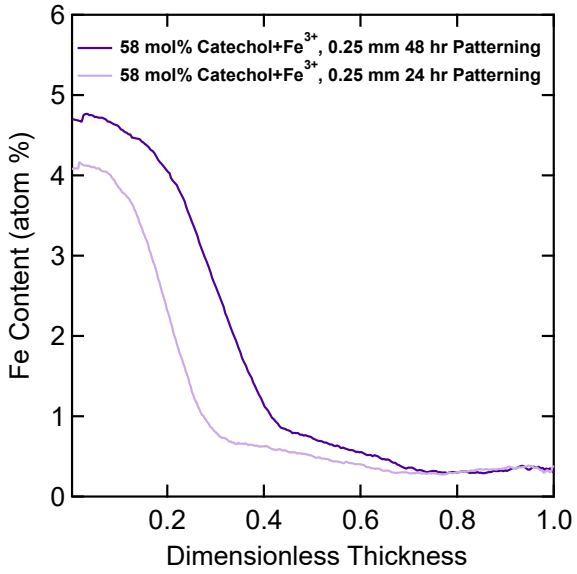


Figure A.8: SEM EDS characterization of Fe^{3+} distributions across film thicknesses in a 3/39/58 mol% PEGDA/PEGMEA/catechol film at various timepoints during selective patterning and iron treatment from a saturated filter paper.

SAXS and WAXS Experiment

A standard procedure for scattering was as follows. Silver behenate was loaded into a capillary tube and used as a calibration standard. X-ray scattering was conducted using a 1.54 angstrom X-ray beam from a XENOCS Genix 50 W x-ray micro-source, focus size 50 microns, with a XENOCS FOX2D monochromator and Dectris EIGER R 1M detector. X-ray scattering was conducted on each sample for 30 minutes of exposure. Fitting and circular averaging was conducted in Igor pro using the Nika macro program[6]. During SAXS measurements, sections of film in water swollen and dry states were individually placed between protective layers of Kapton tape and affixed to the sample holder. For WAXS measurements, the same instrumentation was used, but no Kapton film was used to cover the material, and dry film sections were suspended in air to reduce noise from Kapton tape layers. All measurements, both SAXS and WAXS, were conducted in triplicate on separate batch of polymer network samples, with no significant deviations in trace morphology observed. Representative data is shown in the main text and in **Figures A.10, A.11, A.12, and A.13**.

SAXS measurements of water swollen PFPA or Fe^{3+}-catechol films at higher PFPA/catechol content reveal similar morphological features to films discussed in the main text. Notably for water swollen PFPA samples a significant peak is observed (**Figure A.9C**), corresponding the correlation lengths between PFPA rich regions. Moreover, similar to lower active ester and catechol content networks, upon substitution and Fe^{3+} complexation in catechol films, a shoulder is observed at comparable length scale to the PFPA rich domains, indicating the formation of clusters (**Figure A.19D**). Scattering of control, catechol networks without iron was alco conducted and is shown in **Figure A.10**.

SAXS and WAXS was also conducted on dried films and demonstrated a decrease in feature size for Fe^{3+}-catechol clusters (cf., shift of peak/shoulder features to the right in **Figure A.11D** & **A.11F**) and a lack of crystalline domains (**Figure A.12**) in iron complexed films. Minimal information was gleaned from dried control PEG-acrylate films and PFPA containing films due to their collapsed structure. WAXS traces of Fe^{3+}-catechol films and control PEG-acrylate films reveal smooth, non-crystalline features indicating the amorphous structure of the catechol clusters.

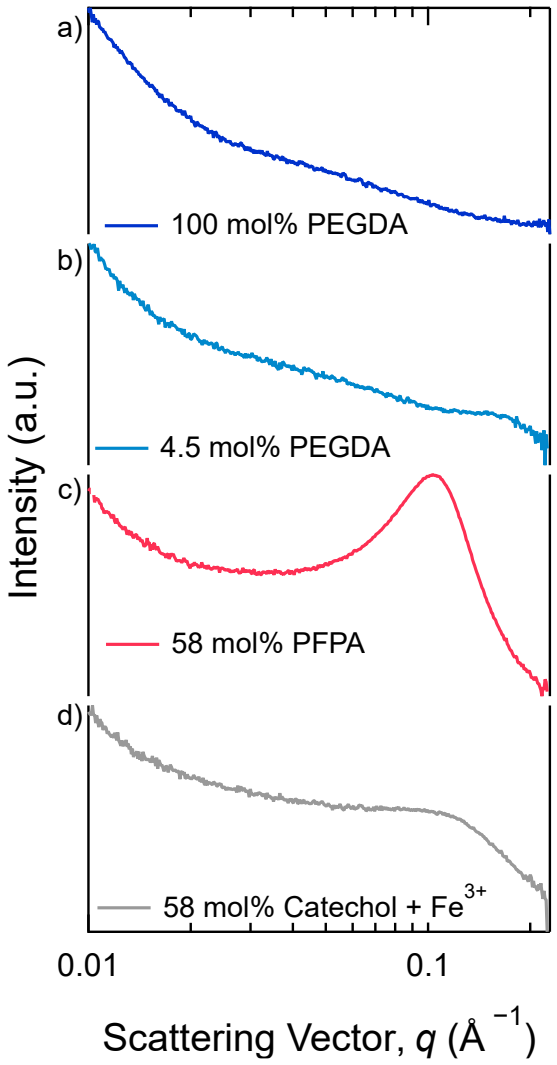


Figure A.9: Small angle x-ray scattering of water swollen polymer networks with comparisons between control and 58 mol% PFPA or catechol networks (a) Scattering of 100 mol% PEGDA network, (b) scattering of 4.5/95.5 mol% PEGDA/PEGMEA network, (c) scattering of 2.9/39/58 mol% PEGDA/PEGMEA/PFPA network, (d) Scattering of 2.9/39/58 mol% PEGDA/PEGMEA/catechol network after substitution with dopamine and subsequent Fe^{3+} complexation.

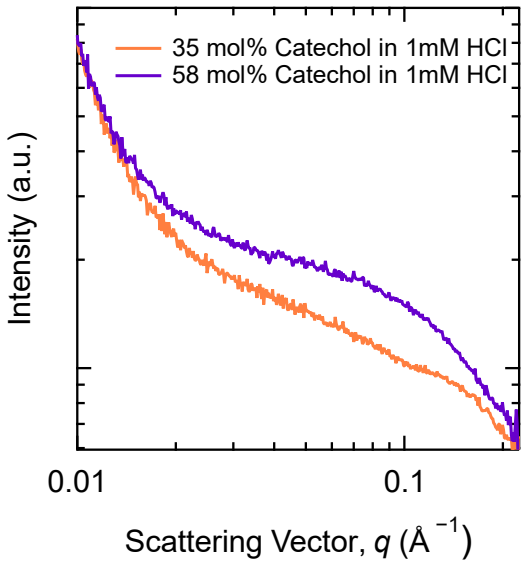


Figure A.10: Small angle x-ray scattering of swollen catechol grafted networks in 1mM HCl solution with 3.5/61/35 mol% PEGDA/PEMGEA/catechol (orange) and 2.9/39/58 mol% PEGDA/PEGMEA/catechol (purple)

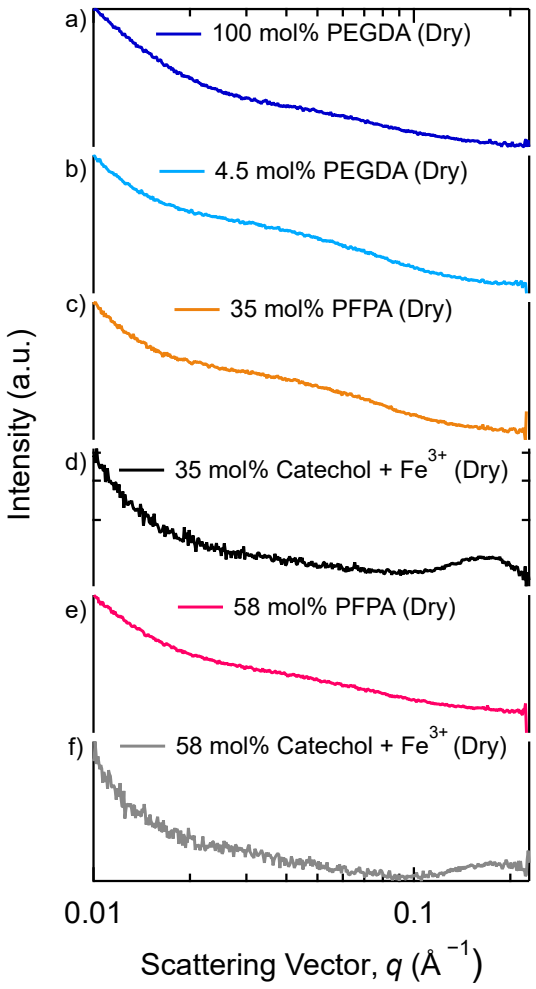


Figure A.11: Small angle x-ray scattering of dry polymer networks with comparisons between control, PFPA, and Fe^{3+}-catechol networks. (a) Scattering of 100 mol% PEGDA network, and (b) scattering of 4.5/95.5 mol% PEGDA/PEGMEA network. (c) Scattering of 4/61/35 mol% PEGDA/PEGMEA/PFPA network before dopamine substitution and (d) scattering after substitution and Fe^{3+} incorporation to form a 4/61/35% PEGDA/PEGMEA/catechol-Fe^{3+} film. (e) Scattering of a 2.9/39/58 mol% PEGDA/PEGMEA/PFPA network and (f) after substitution with dopamine and subsequent Fe^{3+} complexation.

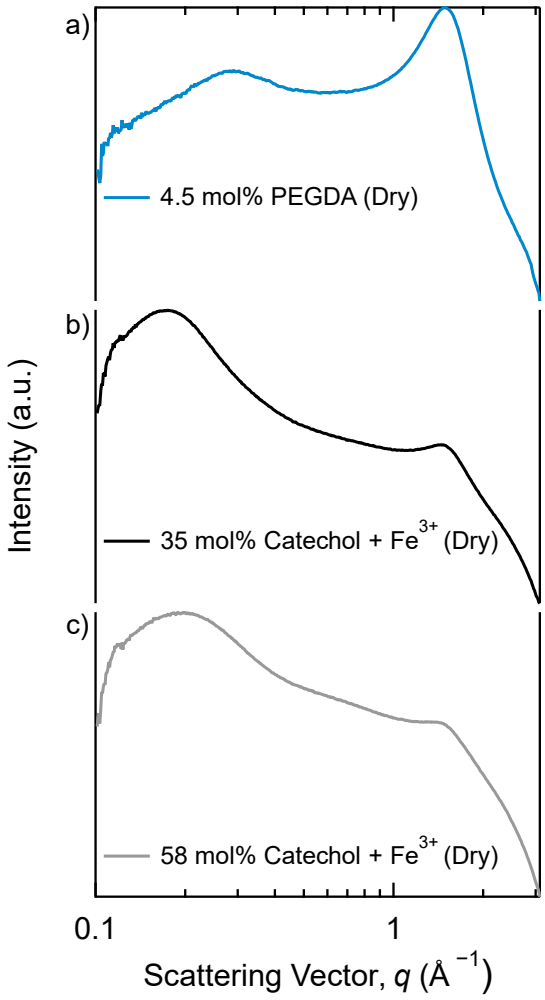


Figure A.12: Wide angle x-ray scattering of dry polymer networks with comparisons between control (a) 4.5/95.5 mol% PEGDA/PEGMEA network, and catechol networks after substitution with dopamine and subsequent Fe^{3+} complexation. (b) Scattering of a 4/61/35% PEGDA/PEGMEA/catechol network, and (c) scattering of 2.9/39/58 mol% PEGDA/PEGMEA/catechol network.

References:

(1) Moon, J. D.; Sujanani, R.; Geng, Z.; Freeman, B. D.; Segalman, R. A.; Hawker, C. J. Versatile Synthetic Platform for Polymer Membrane Libraries Using Functional Networks. Macromolecules 2021, 54 (2), 866–873. https://doi.org/10.1021/acs.macromol.0c02414.

(2) Yin, Q.; Wang, L.; Jiang, J.; Dai, C.; Weng, G.; He, J. Three-Dimensional Shape Transformation of Eu3+-Containing Polymer Films through Modulating Dynamic Eu3+-Iminodiacetate Coordination. Chem. Mater. 2022, 34 (5), 2176–2186. https://doi.org/10.1021/acs.chemmater.1c03722.

(3) Jones, S. D.; Schauser, N. S.; Fredrickson, G. H.; Segalman, R. A. The Role of Polymer-Ion Interaction Strength on the Viscoelasticity and Conductivity of Solvent-Free Polymer Electrolytes. Macromolecules 2020, 53 (23), 10574–10581. https://doi.org/10.1021/acs.macromol.0c02233.

(4) Wuttke, J. Laplace–Fourier Transform of the Stretched Exponential Function: Analytic Error Bounds, Double Exponential Transform, and Open-Source Implementation "Libkww." Algorithms 2012, 5 (4), 604–628. https://doi.org/10.3390/a5040604.

(5) Love, A. A Treatise on the Mathematical Theory of Elasticity; 1892; Vol. 1.

(6) Ilavsky, J. Nika: Software for Two-Dimensional Data Reduction. J. Appl. Crystallogr. 2012, 45 (2), 324–328. https://doi.org/10.1107/S0021889812004037.

Appendix B. Supporting Information for Chapter 3

Materials and Instrumentation

All chemicals were purchased and used as received. Maltol, phenylboronic acid, dopamine hydrochloride salt, DMPA (2.2-dimethoxy-2-phenylacetophenone), pentafluorophenyl, acryloyl chloride (inhibited), PEGMEA (poly(ethylene glycol) methyl ether acrylate, M_n 480, with inhibitor), PEGDA (poly(ethylene glycol diacrylate), M_n 700, with inhibitor), triethyl amine, concentrated hydrochloric acid (12.1 M, 37%), $Ho(NO_3)_3$ (pentahydrate), $DyCl_3$ (hexahydrate), $TbCl_3$ (hexahydrate), and $NaIO_4$ were purchased from Sigma Aldrich. Bicine was purchased from TCI, N-boc-ethylene diamine was purchased from A2B Chem., and Fe(NO3)3 (nonahydrate, ACS reagent grade) was purchased from Acros Organics. All solvents (isopropanol, hexanes, tetrahydrofuran (inhibited), methanol, dimethyl sulfoxide (dry, sure seal)) used were purchased from Sigma Aldrich and used as received without further drying or distillation, with the exception of dichloromethane (DCM) used for synthesis of the PFPA monomer. DCM was dried using a PureSolv MD-5 dry solvent system.

Nuclear Magnetic Resonance (NMR) spectroscopy measurements were collected on a Bruker 400 MHz NMR-spectrometer in deuterated solvents. Measurements of PFPA monomer were taken in deuterated chloroform ($CDCl_3$) and measurements of the amine terminated HOPO ligand (salt final product) were measured in D_2O.

Fourier Transform Infrared Spectroscopy was conducted with attenuated total reflection (FTIR-ATR) on a Thermo Nicolet iS10 spectrometer equipped with a diamond ATR

accessory. 64 scans were taken for all polymer films measured at room temperature under ambient atmosphere.

Raman spectroscopy was conducted on dry polymer films using a Horiba Jobin Yvon spectrometer with confocal microscopy and a 785 nm laser. Hole and slit sizes were set to 500 microns. Accumulation numbers and times were adjusted appropriately to collect high resolution data without burning the sample.

Magnetometry measurements were conducted on Quantum Design SQUID MPMS3 magnetometer. Magnetization versus field measurements were recorded at room temperature from -70 kOe to 70 kOe, with samples secured to a quartz paddle with Kapton tape to secure the sample.

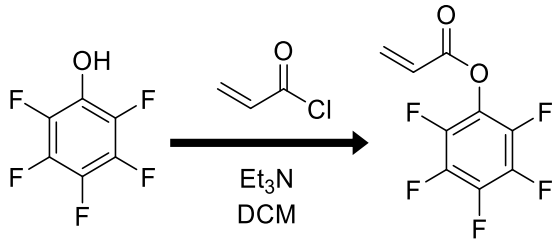
Optical microscope images of dry samples were taken using a Keyence VHX-5000 optical, digital microscope. Samples were imaged with surface illumination unless otherwise noted.

A Trotec Speedy 100 laser cutter was used for manufacture of all PDMS and acrylic sample masks and holders. PDMS sheeting was purchased from B&J Rubber Products with mylar top and bottom backing with 250 micron thickness.

Mechanical testing was conducted on a TA.XT Plus Connect Texture Analyzer with a 50N load cell. The system was operated in compression using the manufacturer's three-point bend test stage.

Synthetic Methods

Synthesis of the PFPA Monomer

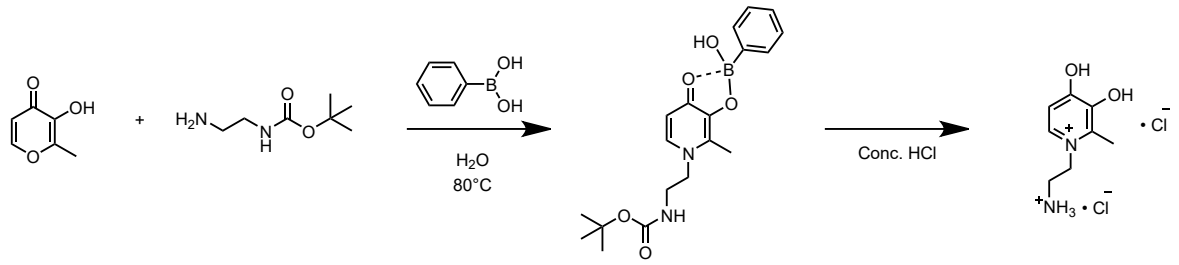


Scheme B.1. Synthesis of the PFPA (pentafluorophenyl acrylate) monomer.

Synthesis of the PFPA monomer was conducted following prior procedures[1]. Pentafluorophenol (0.27 mol, 50g) and triethyl amine (0.29 mol, 40 mL) were dissolved in 700 mL of anhydrous DCM (dried *via* PureSolve MD-5 solvent system) in a large round bottom flask. The flask was cooled to 0°C with an ice bath. In a separate flask, acryloyl chloride (0.303 mol, 24.5 mL) was dissolved in 50 mL of DCM (anhydrous). The acryloyl chloride solution was added dropwise to the cooled solution of pentafluorophenol. The mixture was stirred and allowed to warm to room temperature, and the reaction was allowed to proceed overnight. Consumption of the phenol was verified by TLC. The reaction mixture was washed with 1M HCl three times (300 mL each), followed by three washes with concentrated $NaHCO_3$ (300 mL each). The organic layer was dried over $MgSO_4$, then filtered

through a layered plug of basic alumina and charcoal, and then allowed to sit in solution with additional charcoal for 3 hours to remove yellow discoloration. Product was filtered and concentrated to achieve a clear oil (75% yield), and verified by NMR spectroscopy in $CDCl_3$. 6.70 (d, *J*= 17.5Hz, 1 H), 6.36 (dd, 1 H), 6.18 (d, *J*=10.5 Hz, 1 H).

Synthesis of the HOPO ligand



Scheme B.2: Synthesis of amine terminated HOPO ligand. Same as **Scheme 3.2** but reproduced for reader convenience.

General methods for ligand synthesis were adapted from the approach of Ke, Zhang, and co.[2] to prepare the target material. Maltol (1 equiv., 5g, 40 mmol) and phenylboronic acid (1.2 equiv., 5.85g, 40 mmol) were added to a round bottom flask, followed by addition of 20 mL of deionized (DI) water. The mixture was heated to 80°C under ambient atmosphere with stirring until dissolved. After 10 minutes, N-boc-ethylene diamine (97% purity, 1.07 equiv., 43 mmol, 6.76 mL) was added to the reaction flask and the reaction was allowed to proceed for 3 hours. Conversion was monitored via thin layer chromatography (TLC) with 10% isopropanol in dichloromethane, and upon completion the reaction was allowed to cool. The crude product was observed as a viscous red-orange oil at the bottom of the reaction vessel, and the remaining water was decanted off, and the product briefly washed again with DI water

which was again decanted. 25 mL of concentrated hydrochloric acid (12.1M, 37%) was added and immediate bubbling of the product was observed. Deprotection was allowed to proceed overnight for complete consumption of the oil layer, producing a fluffy, cream-colored crude product. Resultant material was filtered and washed with 1:1 isopropanol:THF (vol:vol). Product was dissolved in 50 mL of DI water, diluted with 200 mL of isopropanol, and recrystallized *via* layered addition of tetrahydrofuran. Initially 400 mL THF was added, and the flask was cooled (freezer, -20°C, 10 mins) to produce seed crystals, followed by addition of another 250 mL of THF and 15 minutes in the freezer. The recrystallized product was incredibly fluffy with needle-like, cream-colored crystals. Product was filtered and dried under vacuum and collected in good yield (65%). Purity of recrystallized material was verified by nuclear magnetic resonance spectroscopy (**Figure B.1**, ^{1}H-NMR and ^{13}C-NMR), in agreement with literature as a dichloride salt[3].

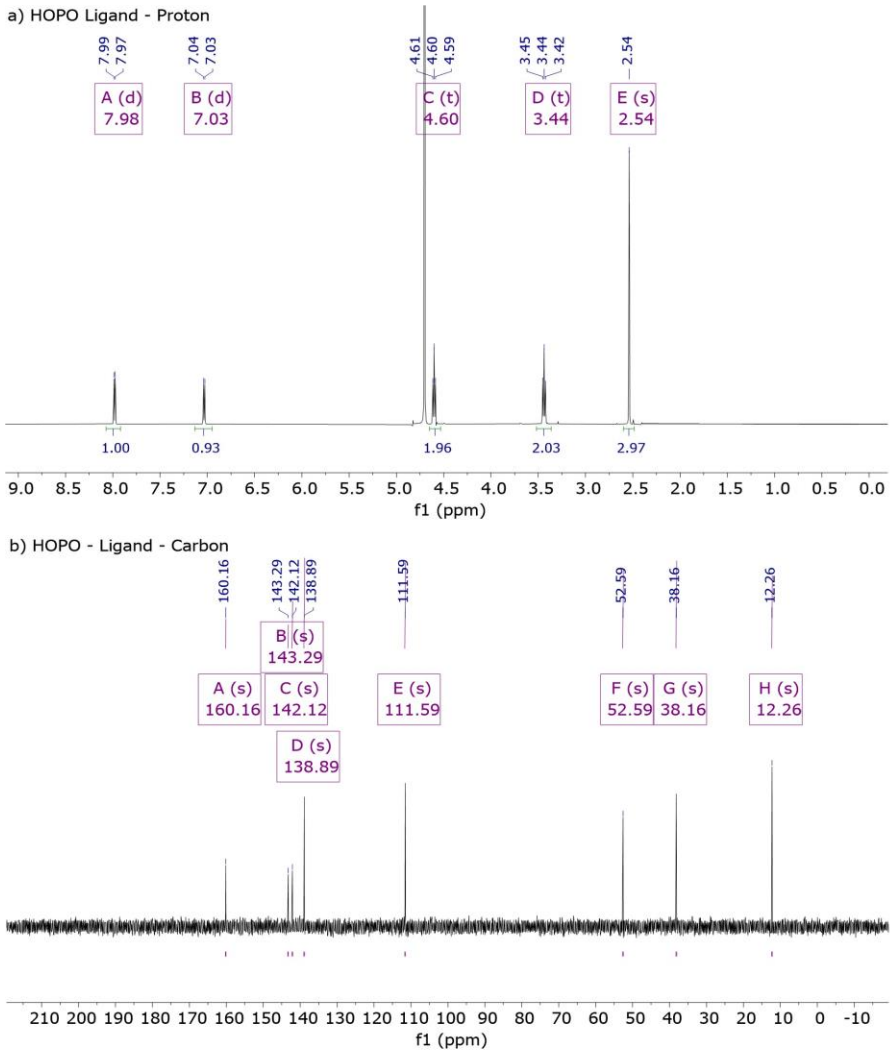


Figure B.1. (a) ^{1}H-NMR of amine terminated HOPO ligand in D_2O. ^{1}H NMR (500 MHz, Deuterium Oxide) δ 7.98 (d, *J* = 7.2 Hz, 1H), 7.03 (d, *J* = 7.0 Hz, 1H), 4.60 (t, *J* = 7.0 Hz, 2H), 3.44 (t, *J* = 7.0 Hz, 2H), 2.54 (s, 3H). (b) ^{13}C-NMR of amine terminated HOPO ligand in D_2O. ^{13}C NMR (101 MHz, Deuterium Oxide) δ 160.16, 143.29, 142.12, 138.89, 111.59, 52.59, 38.16, 12.26.

PFPA Network Synthesis

Network synthesis was conducted following approaches detailed previously[1,4] to prepare PFPA networks. In a representative procedure, PEGDA, PEGMEA, and PFPA were massed and added to a 20 mL vial. DMPA (photo initiator , 0.1 wt% relative to monomers)

was massed and added and the monomer mixture and vortexed until dissolved. The mixture was briefly sonicated to remove gas bubbles, and then dispensed between quartz plates, with film thickness controlled by steel spacer gauges between the plates. Network formation and crosslinking was conducted by irradiation with UV light for 120s (365nm, 3mW/cm^2) on one side. PFPA networks were then transferred to nitrogen sparged solutions for catechol or HOPO substitution.

PFPA Network Substitution

PFPA networks materials were substituted at active ester sites with either dopamine hydrochloride salts following previous procedures[1] or with the HOPO ligand prepared above. In brief, dopamine hydrochloride salts (3 equivalents relative to PFPA sites) were dissolved in a methanol solution and degassed via nitrogen sparging. PFPA networks were added, solution further degassed by sparging, and then triethyl amine was added to initiate the substitution (1.5 equivalents relative to dopamine salts). The reaction was allowed to proceed overnight at ambient temperature under N_2 sparging, followed by dialysis in 0.1M HCl for 24 hours to remove starting materials. Films were then subsequently dialyzed and stored in 1 mM HCl solutions to gradually adjust pH.

HOPO installation was conducted using similar procedures to that of catechol functionalized materials. In a representative substitution, the amine terminated HOPO ligand (dichloride salt, 2.5 equivalents relative to PFPA) was massed and dissolved in a 2:1 (vol:vol) DMSO and methanol solution at a concentration of 15 mg / mL. The ligand was dissolved with gentle heating of the solution container (warm water, approximately 30-40 °C) and

occasional, brief sonication to break up crystallites in solution. Upon complete dissolution to a clear, pale-yellow solution, the mixture was degassed via N_2 sparging and PFPA films were added. After further degassing, triethyl amine (2.5 equivalents relative to HOPO ligand) was added to initiate the substitution and the reaction was allowed to proceed under N_2 atmosphere for 48 hours. Films were then dialyzed in increasingly dilute acid conditions (0.1M HCl and 1 mM HCl) following the catechol procedures above. HOPO networks were stored in 1 mM HCl solutions.

Deswelling of Polymer Networks

Solvent gradient based deswelling methods were adapted from prior work[1] to prepare large surface area dry films for mechanical testing or dehydrate samples after metal ion patterning. Films swollen in aqueous solutions (e.g. 1 mM HCl, water dialysis solutions, etc.) could be gently deswollen to avoid cracking or fracturing of the film on drying. Water swollen materials were transferred to a 3:1 (vol.:vol.) solution of DI water and isopropanol. Isopropanol was gradually added to adjust the ratio to 2:1, 1:1, 1:2, and 1:3 (vol.:vol.) with 30 mins to 1 hour between solvent additions depending on film thickness. Films were then transferred to pure isopropanol and hexanes was added stepwise following the same progression of volumetric ratios until a 1:3 volumetric ratio of IPA:hexanes was achieved. Samples were then removed from the solvent mixture and dried under vacuum.

Oxidation Study of HOPO and Catechol Networks

Sample stability was screened under basic aqueous conditions in ambient atmosphere. Additional control oxidation experiments were performed using sodium periodate ($NaIO_4$)

also under ambient atmosphere. Sample stability to basic aqueous conditions was examined as follows, sample sections of either HOPO or catechol functionalized films were removed from their 1 mM HCl storage solutions and placed in excess aqueous solutions at pH 9 (0.2 M Bicine + KOH). Samples were then left submerged for 24 and 72 hours. After the allotted time had passed, samples were removed, blotted dry of residual basic solution, and transferred to excess fresh 1 mM HCl solution and allowed to equilibrate overnight. Samples were then removed, deswollen following above procedures, dried overnight under vacuum, and finally measured by FTIR. Periodate oxidized samples were prepared by transferring sample sections of HOPO or catechol functionalized films to excess solutions of 0.05 M $NaIO_4$ for 24 hours. Samples were then removed from the oxidant solution, dialyzed in 1 mM HCl, deswollen, dried under vacuum, and measured by FTIR.

FTIR measurements of base or periodate treated films were compared to untreated networks to demonstrate any observed changes in FTIR trace morphology. Notable changes in catechol ring resonances and C-O stretching were observed, which were consistent with literature for catechol functionalized materials[5–10]. Appreciable changes are observed in **Figure B.2**, with diagnostic changes in ring resonances (C=C) at 1600 and 1510 cm^{-1}, C-O stretching at ~1280 cm^{-1}, and C-H resonances between 750-850 cm^{-1}. While these changes are subtle in the 24-hour base treated sample, they become increasingly pronounced at 72 hours of base exposure, and are consistent with control, periodate oxidized films. Such results demonstrate the expected oxidation of catechol motifs under basic, ambient conditions. Conversely, HOPO films show no appreciable changes after 24 and 72 hours of exposure to basic conditions (pH 9), and FTIR traces of periodate oxidized samples are inconsistent with

control or base treated materials. Such results agree with prior literature[11,12] on the improved stability of the HOPO motif, relative to classical catechol counterparts, under basic aqueous conditions.

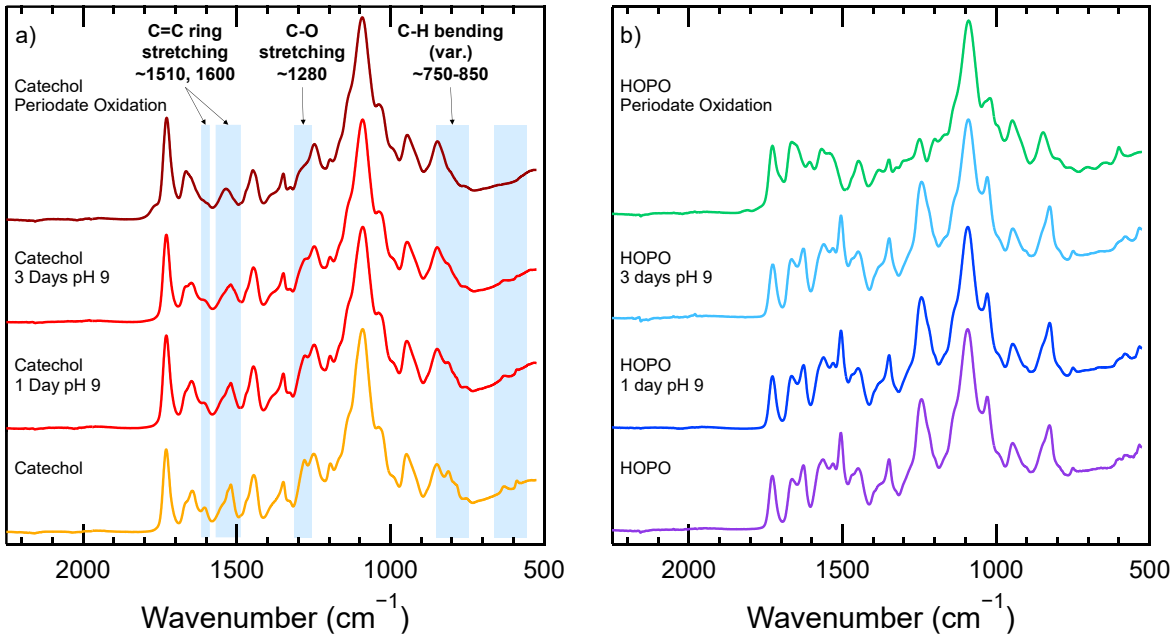


Figure B.2: (a) Bottom to top: untreated catechol network, catechol network after 24 hours of base exposure, after 72 hours of base exposure, and after periodate oxidation. Blue highlights are included to show changing FTIR signals indicative of oxidation for C=C ring resonances (approx. 1600 and 1510 cm^{-1}), C-O stretching (1280 cm^{-1}), and C-H bending modes (various, between approx. 750 and 850 cm^{-1}). (b) Bottom to top: untreated HOPO network, HOPO network after 24 hours of base exposure, after 72 hours of base exposure, and after periodate oxidation. Negligible changes between untreated and base treated HOPO films were noted after re-equilibration under acidic storage conditions, while periodate oxidized films display appreciable changes in FTIR peaks, inconsistent with untreated or base treated samples.

Bulk Metal Salt Treatment of Functionalized Networks

Metal ions were incorporated into polymer networks following previously developed procedures[1,13]. Prior to metal center installation, solutions of the desired salt were prepared at 0.05 M concentration with 0.2 M bicine, buffered to pH 7.5 by addition of a 3 M KOH stock solution. Metal salt solution volume during complexation was adjusted to be in excess (>3x) of the metal center content needed to fully crosslink the film. Unless otherwise noted, HOPO or catechol network materials were left in the representative metal center solution for 3 days. After complexation, samples were removed, blotted dry, and dialyzed in DI water to remove any residual salts. DI water was exchanged daily, followed by dehydration of the films following the deswelling procedure above. Characterization of dry, bulk films *via* Raman spectroscopy was conducted following methods detailed above. iron, holmium, and unfunctionalized HOPO network Raman spectra are displayed in main text **Figure 3.3** and additional Raman data, for Tb^{3+}-HOPO films are displayed below in **Figure B.3**. As per literature expectations of other lanthanide complexes[14], similar peak shifts for Tb^{3+}-HOPO and Dy^{3+}-HOPO films are observed relative to the Ho^{3+} films.

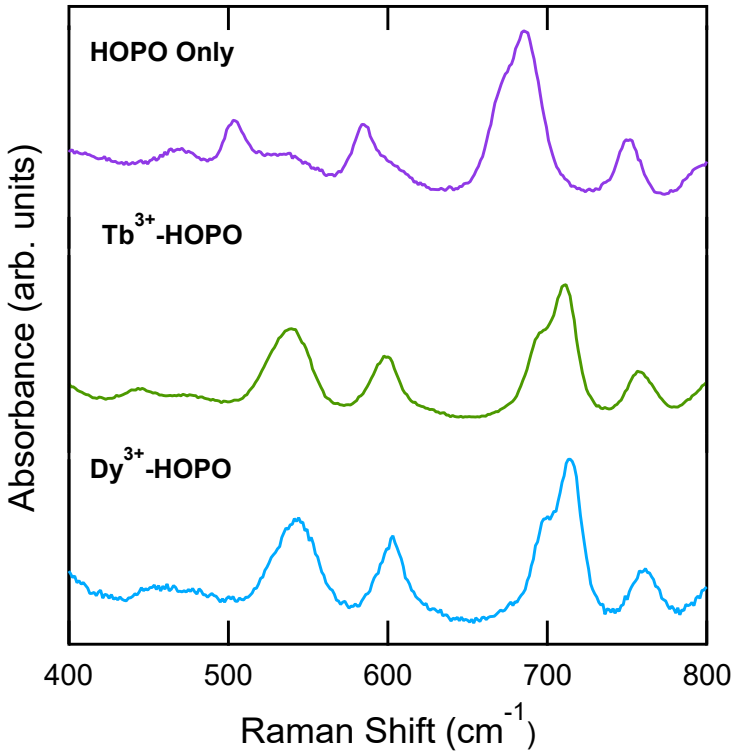


Figure B.3. Raman spectra for (top) metal free HOPO network, replotted for convenience. (middle, green) Raman spectra for Tb^{3+}-HOPO network, and (bottom, blue) Dy^{3+}-HOPO and networks after bulk metal treatment.

Beam Bending Methods

Beam bending was conducted on a TA.XT Plus Connect Texture Analyzer following previous procedures[1] using the three-point bend sample holder. Beam bending measurements were conducted at 0.1 mm/s displacement rates to turn around forces between 15 and 50 mN in accordance with sample stiffness, and sample span was appropriately adjusted to sample width between 10 and 30 mm. Sample elastic moduli were calculated according to **Equation B.1**, for sample stiffness k, beam length L, beam width b, and beam height h.[15]

$$E = \frac{kL^3}{4bh^3}$$

Equation B.1. Moduli calculation from the bending equation for a center loaded beam.

Table B.1. Beam bending summary data for metal complexed polymer networks.

Ligand or M^{n+}-Ligand	**Network Composition**			**Young's Modulus, E, (MPa)**	**Standard Deviation (MPa)**	**Number of replicates n**
	mol% ligand	mol% PEGDA	mol% PEGMEA			
HOPO	58%	2.9%	39%	3.8	1.1	4
HOPO-Fe^{3+}	58%	2.9%	39%	299	42	4
HOPO-Ho^{3+}	58%	2.9%	39%	298	13	3
HOPO-Tb^{3+}	58%	2.9%	39%	357	32	6
Catechol	58%	2.9%	39%	3.1	0.9	5
[a]Catechol-Fe^{3+}	58%	2.9%	39%	245	26	3
Catechol-Ho^{3+}	58%	2.9%	39%	11.5	1.1	5

[a]Values for catechol-Fe^{3+} elastic moduli, error, and replicates were obtained from prior work[1].

Magnetometry Measurements of Metal-Ligand Networks

Samples were prepared by punching 4 mm diameter discs from dry, metal free, HOPO or catechol networks. Sample mass was recorded and then metal containing samples were individually placed in the corresponding metal salt solution and allowed to complex for 3 days under ambient atmosphere followed by dialysis in DI water for 3 days. Samples were deswollen, dried under vacuum overnight, massed, and measured. Magnetization versus field measurements were recorded at room temperature from -70 kOe to 70 kOe, with samples secured to a quartz paddle with Kapton tape to secure the sample. For metal complexed films, data was scaled by sample mass with background magnetic moment from a metal free control subtracted.

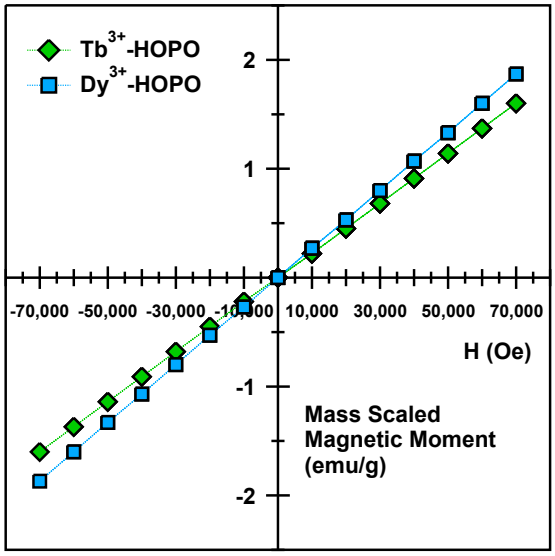


Figure B.4: Magnetization curves of HOPO functionalized polymer networks complexed with either Tb^{3+} salts (green diamonds) or Dy^{3+} salts (blue squares).

Patterning of Metal Centers into HOPO Films

Patterning of metal ions into metal free HOPO films

Patterning of metal center domains could be conducted through modification of previous procedures for patterning of one or both sides of an untreated HOPO film with one or two metal centers[1]. In a representative procedure (**Figure B.5**), a porous laser cut acrylic holder was procured, and a laser cut PDMS mask layer placed on top. A section of HOPO functionalized network would be removed from the 1 mM HCl storage solution, blotted dry, and placed against the PDMS mask. For single sided patterning experiments, an uncut PDMS backing sheet would be placed over the top of the sample, or in a double-sided patterning experiment, a second laser cut mask would be adhered over the sample. Following placement of the second PDMS layer (backing or mask), a laser cut gasket of PDMS would be placed over the second PDMS sheet (backing or mask) to act as a spacer and more evenly distribute pressure over the sample surface. The sample was then enclosed by a second rigid acrylic sheet, which can be either flat or porous for single- or double-sided patterning respectively. The stack of acrylic holders, masks, and samples could then be placed between cut acrylic tanks with laser cut PDMS gaskets at acrylic-acrylic interfaces. The system would be held under pressure using large, 1 inch metal binder clips to create watertight seals on the acrylic tanks, and metal salt solutions could be added to each side of the patterning assembly. Patterning was allowed to proceed for several hours to overnight complexations depending on the depth and extent of metal ion intrusion desired, followed by DI dialysis and sample deswelling. Note, great care should be taken to avoid iron contaminants in patterning or other metal complexation experiments due to the strong affinity of 3,4-hydroxypyridinone motifs

for Fe^{3+} ions. Staining or uptake of iron ions by HOPO networks was observed when in contact with ferric contaminants (e.g. steel tweezers, etc.)

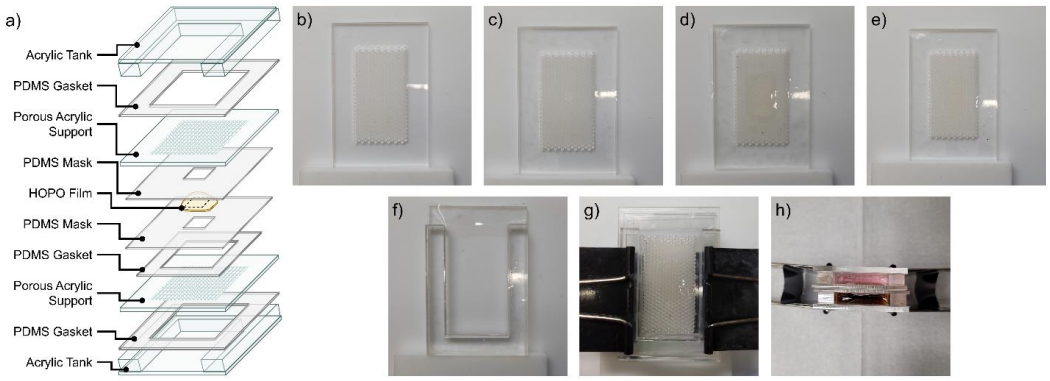


Figure B.5. An example of patterning holder assembly for a double sided solution patterning experiment. (a) A schematic detailing a representative sequence of parts and ordering for conducting a two-sided patterning experiment. (b) A laser cut, porous acrylic sample holder. (c) Placement of a small square, laser cut, PDMS mask. (d) Placement of a metal free HOPO film against the patterning stack, and enclosure of the film with the top PDMS mask and gasket layers. (e) placement of the top acrylic patterning holder (f) Image of the solvent welded acrylic tank with PDMS gasket placed on top surface. (g) Assembled patterning holder with front and back tanks placed against porous acrylic holders, and secured with large metal clasps. (h) top view after solution filling of double sided patterning with holmium (light pink) and iron (brown) filling each of the patterning solution tanks.

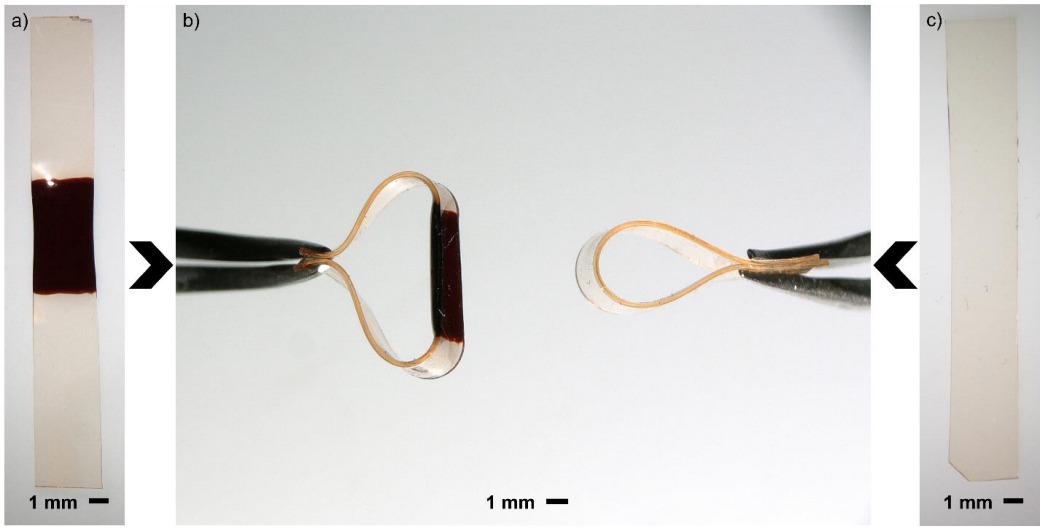


Figure B.6. An example of Fe3+ patterning into an untreated HOPO film analogous to main text **Figure 3.7**. (a) Polymer film of 3/39/58 mol% PEGDA/PEGMEA/HOPO with a central section functionalized with Fe^{3+}-HOPO complexes. (b) Comparison of film mechanical behavior under folding between metal-patterned (left) and metal free (right). (c) Polymer film of 3/39/58 mol% PEGDA/PEGMEA/HOPO without any metal ions installed in the network.

Patterning of Metal Centers into Tb^{3+} Films via Ion Exchange

Patterning of metal ions into Tb^{3+} films was conducted via exchange of Tb^{3+} metal centers with either Ho^{3+} or Fe+. In a representative procedure, a section of HOPO network would be allowed to complex in a 0.05 M Tb^{3+}, 0.2 M Bicine solution at pH 7.5 for three days following above procedures. The sample would then be removed from solution, blotted dry, and patterned in either a double or single sided fashion as described above for the untreated HOPO films. Following sample surface patterning, films would be dialyzed in DI water, and deswollen using the gentle solvent gradient.

References:

(1) Shannon, D. P.; Moon, J. D.; Barney, C. W.; Sinha, N. J.; Yang, K.-C.; Jones, S. D.; Garcia, R. V.; Helgeson, M. E.; Segalman, R. A.; Valentine, M. T.; Hawker, C. J. Modular Synthesis and Patterning of High-Stiffness Networks by Postpolymerization Functionalization with Iron–Catechol Complexes. *Macromolecules* **2023**, *56* (6), 2268–2276. https://doi.org/10.1021/acs.macromol.2c02561.

(2) Ke, D.; Zhang, L.; Zhong, X.; Shao, J.; Yu, Y.; Chen, W. Boronic-Acid-Accelerated Electrophilic Activation of Unprotected Maltols to N-Substituted Hydroxypyridinones in Water. *Org. Lett.* **2022**, *24* (6), 1263–1267. https://doi.org/10.1021/acs.orglett.1c03833.

(3) Gomes, M. C.; Costa, D. C. S.; Oliveira, C. S.; Mano, J. F. Design of Protein-Based Liquefied Cell-Laden Capsules with Bioinspired Adhesion for Tissue Engineering. *Advanced Healthcare Materials* **2021**, *10* (19), 2100782. https://doi.org/10.1002/adhm.202100782.

(4) Moon, J. D.; Sujanani, R.; Geng, Z.; Freeman, B. D.; Segalman, R. A.; Hawker, C. J. Versatile Synthetic Platform for Polymer Membrane Libraries Using Functional Networks. *Macromolecules* **2021**, *54* (2), 866–873. https://doi.org/10.1021/acs.macromol.0c02414.

(5) Patai, S. *The Chemistry of Quinonoid Compounds*; The Chemistry of Functional Groups; 1974.

(6) Knorr, D. B. Jr.; Tran, N. T.; Gaskell, K. J.; Orlicki, J. A.; Woicik, J. C.; Jaye, C.; Fischer, D. A.; Lenhart, J. L. Synthesis and Characterization of Aminopropyltriethoxysilane-Polydopamine Coatings. *Langmuir* **2016**, *32* (17), 4370–4381. https://doi.org/10.1021/acs.langmuir.6b00531.

(7) Zangmeister, R. A.; Morris, T. A.; Tarlov, M. J. Characterization of Polydopamine Thin Films Deposited at Short Times by Autoxidation of Dopamine. *Langmuir* **2013**, *29* (27), 8619–8628. https://doi.org/10.1021/la400587j.

(8) Lagutschenkov, A.; Langer, J.; Berden, G.; Oomens, J.; Dopfer, O. Infrared Spectra of Protonated Neurotransmitters : Dopamine. *Physical Chemistry Chemical Physics* **2011**, *13* (7), 2815–2823. https://doi.org/10.1039/C0CP02133D.

(9) Aktaş, N.; Şahiner, N.; Kantoğlu, Ö.; Salih, B.; Tanyolaç, A. Biosynthesis and Characterization of Laccase Catalyzed Poly(Catechol). *Journal of Polymers and the Environment* **2003**, *11* (3), 123–128. https://doi.org/10.1023/A:1024639231900.

(10) Pillar-Little, E. A.; Zhou, R.; Guzman, M. I. Heterogeneous Oxidation of Catechol. *J. Phys. Chem. A* **2015**, *119* (41), 10349–10359. https://doi.org/10.1021/acs.jpca.5b07914.

(11) Menyo, M. S.; Hawker, C. J.; Waite, J. H. Versatile Tuning of Supramolecular Hydrogels through Metal Complexation of Oxidation-Resistant Catechol-Inspired Ligands. *Soft Matter* **2013**, *9* (43), 10314–10323. https://doi.org/10.1039/C3SM51824H.

(12) Andersen, A.; Krogsgaard, M.; Birkedal, H. Mussel-Inspired Self-Healing Double-Cross-Linked Hydrogels by Controlled Combination of Metal Coordination and Covalent Cross-Linking. *Biomacromolecules* **2018**, *19* (5), 1402–1409. https://doi.org/10.1021/acs.biomac.7b01249.

(13) Filippidi, E.; Cristiani, T. R.; Eisenbach, C. D.; Herbert Waite, J.; Israelachvili, J. N.; Kollbe Ahn, B.; Valentine, M. T. Toughening Elastomers Using Mussel-Inspired Iron-Catechol Complexes. *Science* **2017**, *358* (6362), 502–505. https://doi.org/10.1126/science.aao0350.

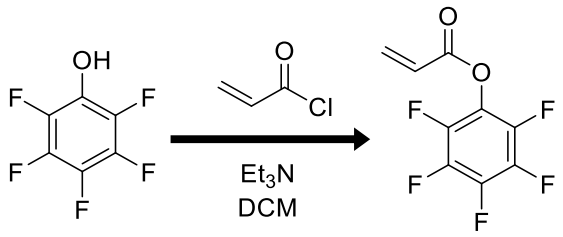
(14) Jianlin, Y.; Yaxian, Y.; Renao, G. Raman Spectroscopic Studies on Tropolone Complexes with La, Nd, Sm, Yb. *Spectrochimica Acta Part A: Molecular and Biomolecular Spectroscopy* **2006**, *64* (4), 1072–1076. https://doi.org/10.1016/j.saa.2005.09.017.

(15) Love, A. *A Treatise on the Mathematical Theory of Elasticity*; 1892; Vol. 1.

Appendix C. Supporting Information for Chapter 4

Reagents and Active Ester Synthesis:

All reagents were purchased and used as received. Poly(ethylene glycol) diacrylate (PEGDA, Mn 700), poly(ethylene glycol) methyl ether acrylate (PEGMEA, Mn 480), 2,2-dimethoxy-2-phenylacetophenone (DMPA, photoinitiator), acryloyl chloride, pentafluorophenol, triethyl amine (TEA), erythrosine B, 4-Amino-2,2,6,6-tetramethylpiperidine (ATMP), diethylene glycol amine (DEG, 2-(2-Aminoethoxy)ethanol), lauryl amine, triethylene glycol ether amine (OligoPEG, 2-(2-(2-methoxyethoxy)ethoxy)ehanamine), and FC-70 were all purchased from Sigma Aldrich. FC-40 was purchased from Ran Biotechnologies. 4-amino-TEMPO (4-Amino-2,2,6,6-tetramethylpiperidine-1-oxyl) was purchased from Ambeed, and 4-(aminomethyl)piperidine was purchased from TCI. Isopropanol, hexanes, methanol, THF, and other solvents were procured from Sigma Aldrich and used as received without further drying or distillation, with the exception of DCM used in PFPA synthesis, which was dried via a PureSolv MD-5 dry solvent system.



Scheme C.1. Synthesis of pentafluorophenyl acrylate (PFPA) monomer.

Pentafluorophenyl acrylate (PFPA) was synthesized following previous procedures[1]. In brief, pentafluorophenol (50 g, 0.27 mol) and Et_3N (40 mL, 0.29 mol) were dissolved in anhydrous DCM (700 mL) and cooled to 0 °C. In a separate flask, acryloyl chloride (24.5 mL, 0.303 mol) was dissolved in 50mL of anhydrous DCM and was added dropwise to cooled pentafluorophenol solution. The mixture was stirred and allowed to warm to room temperature overnight. The reaction was washed with 1 M HCl (3x 300mL), then washed with concentrated NaHCO3 (2x 300mL), and dried over MgSO4. The organic phase was then filtered through a layered plug of basic alumina and charcoal and allowed to sit with additional charcoal for 3 hours to remove yellow coloration, filtered, and then concentrated to obtain a clear oil (75% yield). 6.70 (d, J= 17.5Hz, 1 H), 6.36 (dd, 1 H), 6.18 (d, J=10.5 Hz, 1 H).

Active ester content in microparticle and bulk networks was determined *via* Fourier Transform Infrared Spectroscopy with Attenuated Total Reflection (FTIR-ATR) analysis (*vide infra*), conducted on a Thermo Nicolet iS10 spectrometer equipped with a diamond ATR accessory using 64 scans. FTIR measurements were taken at room temperature under ambient atmosphere.

Additional Information for Flow Synthesis of PEGDA Microparticles and Compositions:

Microfluidic parts were purchased from IDEX Health and Science and used without further modification. The entire system was designed from simple, off the shelf parts listed below. Unless otherwise specified, all tubing used was High Purity PFA Plus tubing (Part# 1932) with a 360 micron outer diameter and 100 micron inner diameter; all tubing ends trimmed *via* a capillary tubing cutter; and connections were made with coned, PEEK, MicroTight ferrules for 360 micron diameter tubing (Part# F-152) and the corresponding screw fittings (Part# P-416). Syringes were connected with PEEK, threaded Luer adapters, with a 0.006" Bore, (IDEX, Female Luer x MicroTight® Assembly Part# P-662). The T-connector used in the fluorous line was the PEEK MicroTee for 360 micron tubing (Part# P-888), and the 4-way cross connector was the PEEK MicroCross for 360 micron tubing (Part# P-889)

Materials of varied final water content could be prepared through modulation of the PEGDA (crosslinker) content, and PFPA content was varied to account for dilution of spin label signal from microparticle swelling. For initial materials with low PFPA content, flow rates of 10:1, vol:vol, FC-40 to monomers were used with an approximate residence time of 30 seconds, reactor length of 15 cm, and total flow rate of ~140 ul/hr, with slight modulation (e.g. 5-10 uL/hr) to avoid clogging in individual runs. Comparable approaches were used for flow synthesis of microparticles with higher active ester content, however higher flow rates and consequentially longer reactor tubing lengths were used, as well as a more fluorinated carrier solvent (FC-70) to reduce sidewall sticking and increase active ester incorporation. Flow synthesis was conducted at relative flow rates of 4.5:1, vol:vol, FC-70 to monomer

mixtures, with a total flow rate of 330 ul/hr and residence time of approximately ~22 seconds. Representative monomer compositions for starting resins can be seen in **Table C.1**.

After flow polymerization, particles were collected in acetone, the fluorous layer was pipetted off, and particles were washed in acetone (ca. 20 mL) three times to remove residual monomer. To remove trace amounts of fluorous solvent remaining, the acetone layer was pipetted off, particles were washed with hexanes (ca. 20 mL) to bring them into a non-polar solvent, followed by a wash (ca. 20 mL) with a 10:1 mixture of hexanes and decafluoropentane to wash away remaining fluorous solvent. Particles were washed again with hexanes to further remove trace fluorous solvents, and lastly three times with acetone. Microparticle samples were washed & dialyzed in THF three times prior to substitution in order to change solvents.

Table C.1: Precursor resin compositions of PEG-acrylate microparticles.

Mol% PEGDA	**Mol% PEGMEA**	**Mol% PFPA**
1.7%	97.5%	0.8%
7%	92.4%	0.65%
16%	83.4%	0.59%
37%	62.5%	0.54%
92%	7.5%	0.5%

Table C.2: Precursor resin compositions for high PFPA content microparticles and bulk films with varied sidechain chemistries, and relative amine stoichiometries used in mixed amine substitutions of high PFPA content particles. Note, for TEMPO free samples, ATMP was used in place of amino-TEMPO at equivalent stoichiometric ratios. Abbreviations: diethylene glycol (DEG), triethylene glycol ether (OligoPEG).

Mol% PEGDA	**Mol% PEGMEA**	**Mol% PFPA**	**Amine 1**	**Amine 2**	**Amine Molar Equivalents Ratio (mmol Amine 1: mmol Amine 2)**
1.7%	78.3%	20%	Amino-TEMPO	Lauryl Amine	1:10
1.7%	78.3%	20%	Amino-TEMPO	Triethylene glycol ether (OligoPEG) amine	1:10
1.7%	78.3%	20%	Amino-TEMPO	Diethylene glycol (DEG) amine	1:5
7%	73%	20%	Amino-TEMPO	Lauryl Amine	1:15

7%	73%	20%	Amino-TEMPO	Triethylene glycol ether (OligoPEG) amine	1:10
7%	73%	20%	Amino-TEMPO	Diethylene glycol (DEG) amine	1:5
16%	64%	20%	Amino-TEMPO	Lauryl Amine	1:20
16%	64%	20%	Amino-TEMPO	Triethylene glycol ether (OligoPEG) amine	1:10
16%	64%	20%	Amino-TEMPO	Diethylene glycol (DEG) amine	1:5

Synthesis of Bulk PEGDA Networks

As outlined in the main text, bulk networks could be prepared from the same precursor resin stocks by curing the polymer network between quartz plates, with film thickness

controlled at 250 microns by spacers between the plates as outlined in previous work[1,2]. In a representative procedure, the monomer mixture was dispensed to a clean quartz plate, spacers were placed on the plate edges, and then a second quartz plate was gently placed on top so as to avoid air-bubbles in the network. Polymer network films were cured via UV irradiation (3 mW/cm^2) and functionalized following prior procedures adapted from microparticle networks. Representative schematic is included in **Figure C.1**.

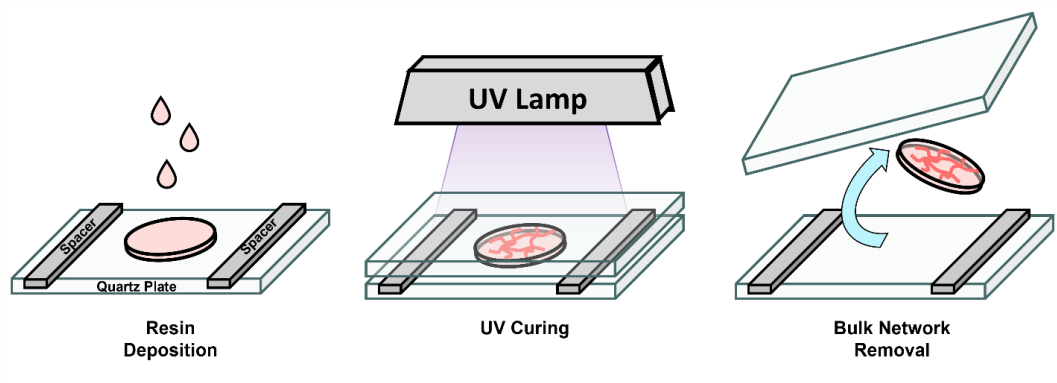


Figure C.1 Schematic of bulk network curing via UV irradiation and film casting between quartz plates. Left to right resin dispensed onto a quartz plate with spacers of the desired thickness, covered with a top quartz plate and cured via UV, followed by removal from the casting assembly.

Characterization of Active Ester Content:

As referenced above, active ester content was determined *via* Fourier Transform Infrared Spectroscopy with Attenuated Total Reflection (FTIR-ATR) analysis. Measurements were conducted on a Thermo Nicolet iS10 spectrometer equipped with a diamond ATR accessory using 64 scans. FTIR measurements were taken at room temperature under ambient atmosphere.

Active ester content for high PFPA content particles was determined via FTIR and compared to control (bulk) networks to confirm PFPA incorporation and substitution. Successful incorporation and substitution of the PFPA moiety was determined *via* the presence and disappearance of diagnostic peaks of the pentafluorophenol at 1780, 1520, and 985 cm^{-1} in agreement with previous procedures[1,2]. Representative IR traces comparing microparticle and bulk networks are included in **Figure C.2**.

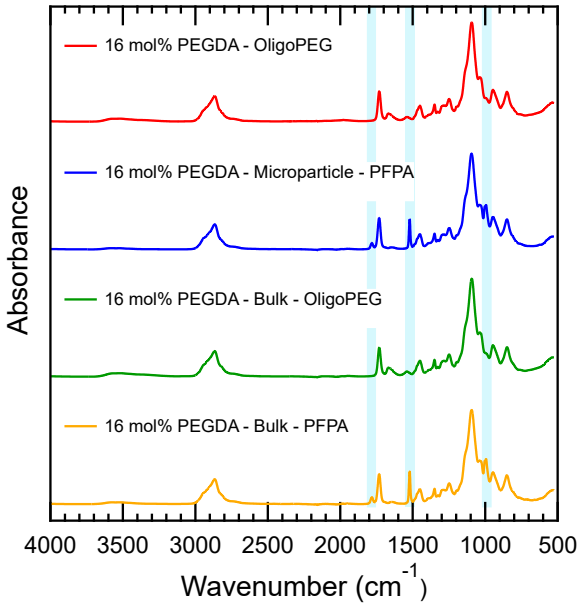


Figure C.2: Representative FTIR traces of PFPA containing and substituted networks with starting resin composition of 16 mol% PEGDA / 64 mol% PEGMEA / 20 mol% PFPA. Diagnostic bands for PFPA are highlighted in blue (C=O stretching 1780 cm^{-1}, C=C vibrations 1520 cm^{-1}, and C-F bending 985 cm^{-1}). From top to bottom, (red) microparticle networks substituted with oligoPEG-amine (triethylene glycol ether amine); (blue) PFPA containing microparticle networks; (green) bulk network substituted with oligoPEG-amine (triethylene glycol ether amine); (yellow) PFPA containing bulk network.

In addition to validating PFPA incorporation, FTIR was used to estimate the relative content of active esters in microparticle networks due to potential miscibility of PFPA with the carrier (FC-40 or FC-70). Monomer mixture resins of known PFPA content were prepared and cured as control (bulk) films and used to construct a calibration curve. PFPA content was determined by initially integrating the PFPA and PEG-acrylate carbonyl stretching bands (1780 cm^{-1} 1730 cm^{-1}, respectively) in Igor Pro using the multi-peak fitting tool. The relative fraction of absorbance of active ester carbonyls relative to total carbonyl absorbance (e.g. PFPA + PEG-acrylate) was plotted against the mol% of active ester in the starting network. From this, a linear relationship was observed and used to build a calibration curve (**Figure C.3**, dashed line). Microparticle networks with high PFPA content in the initial resin were then dried in vacuum overnight, measured via FTIR, their carbonyl peaks integrated, and relative fraction of active ester absorbance computed. This value can be compared to the calibration curve to determine the approximate mol% of PFPA in the final microparticle network (x-axis value, **Figure C.3**, triangles). In all cases, microparticle samples showed comparable active ester content (17-19 mol%) to initial formulations within limitations of error (**Table C.2**).

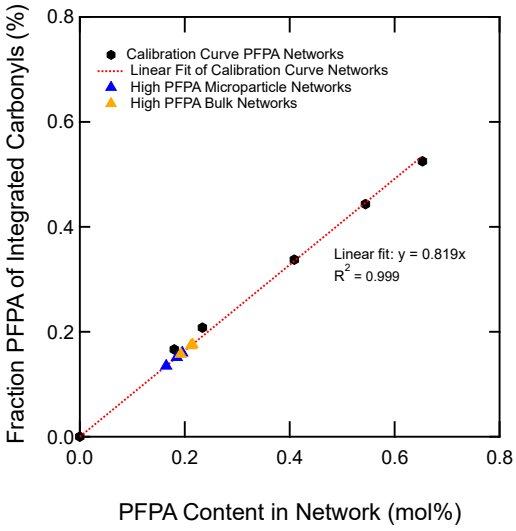


Figure C.3: FTIR Calibration curve (red) of PFPA containing PEGDA networks (black hexagons) of varied composition; and demonstration of PFPA content estimation in microparticle networks (blue triangles) from fraction of PFPA carbonyl integration out of total carbonyl integration. For reference, bulk networks of equivalent composition are also plotted (orange triangles), and demonstrate similar PFPA content by this approach.

Active Ester Substitution by Amines:

For the various materials prepared in this study the general substitution procedure was as follows. Network samples as either microparticles or bulk films were dialyzed in THF prior to active ester substitution. Substitutions were conducted in THF (ca. 10 mL) using significant excess (>3x molar) equivalent of amine(s) relative to PFPA active ester sites in the network. In all cases, after amine installation, particles or films were again washed and dialyzed for extended periods (60+ min) three times with THF to remove residual amines, then washed and dialyzed into DI water three times prior to measurement.

Single amine installations into low PFPA content networks (**Table C.1**) were conducted with an excess (>>3x molar) of the desired amine functionality. Spin labels were

installed in low PFPA content microparticles (compositions in **Table C.1**) according to main text **Scheme 4.1** with 4-amino-TEMPO (4-Amino-2,2,6,6-tetramethylpiperidine-1-oxyl). Spin label-free analogues for $T_{1,0}(0)$ measurements in ODNP were prepared from the same PFPA containing parent materials but were substituted with 4-(aminomethyl)piperidine (AMP). Bulk films for PFG-NMR spectroscopy measurements were prepared from the same monomer mixtures but cast between quartz plates as outlined above and substituted with AMP.

Mixed amine installation was conducted on high PFPA content (**Table C.2**) microparticle networks to prepare spin labeled materials with hydrophilic or hydrophobic substituents according to main text **Scheme 4.2**. Network resin compositions and amine stoichiometries used are included in **Table C.2**. Relative amine stoichiometric ratios were adjusted so as to achieve particles with sufficient TEMPO content for ODNP measurements. Bulk films with hydrophilic or hydrophobic substituents were prepared from the same monomer resin mixtures used for microparticle networks (**Table C.2**), with only minor modifications to the approach outlined in **Scheme 4.2**. Notably, radical free moieties were used for PFG-NMR spectroscopy measurements. As such, instead of 4-amino-TEMPO, the nitroxide-radical free analogue, 4-amino-2,2,6,6-tetramethylpiperidine (ATMP) was used. Mixed amine substitutions were conducted at the same stoichiometric ratios outlined in **Table C.2** (e.g. 20:1 ratio of lauryl amine:ATMP). Given the high structural similarity of ATMP to TEMPO and relative excess of the secondary amine in substitution, we anticipate there are negligible changes to amine reactivity with active ester sites in the network and minimal impact on final network water volume fraction (**Figure C.5**).

Additional Microscopy Characterization Control Study

As discussed in the main text, control study measurements of swollen and dry particle diameters after staining with erythrosine B were conducted. In brief, substituted particles were allowed to swell to equilibrium in deionized (DI) water and segregated into control (unstained) and stained subsets. Control particle diameters were measured manually using distance measurement tools of the Keyence software in the swollen and dry state. Experimental group particles were stained in a 0.1 wt% solution of erythrosine B in deionized water, followed by repeated washing in an excess of DI water (3x) until clear. Particle diameters were then measured in the swollen and dry state with manual and automated distance measurement tools. Results for stained particles measured with automated and manual tools revealed comparable particle diameters. Diameter values were within error of both each other, as well as manually measured, unstained particles. These observations were consistent in both the dry and wet states. Moreover, utilization of automated measurement tools enabled facile measurement of large numbers of particles to get representative populations for swelling measurements without manual measurement error and bias.

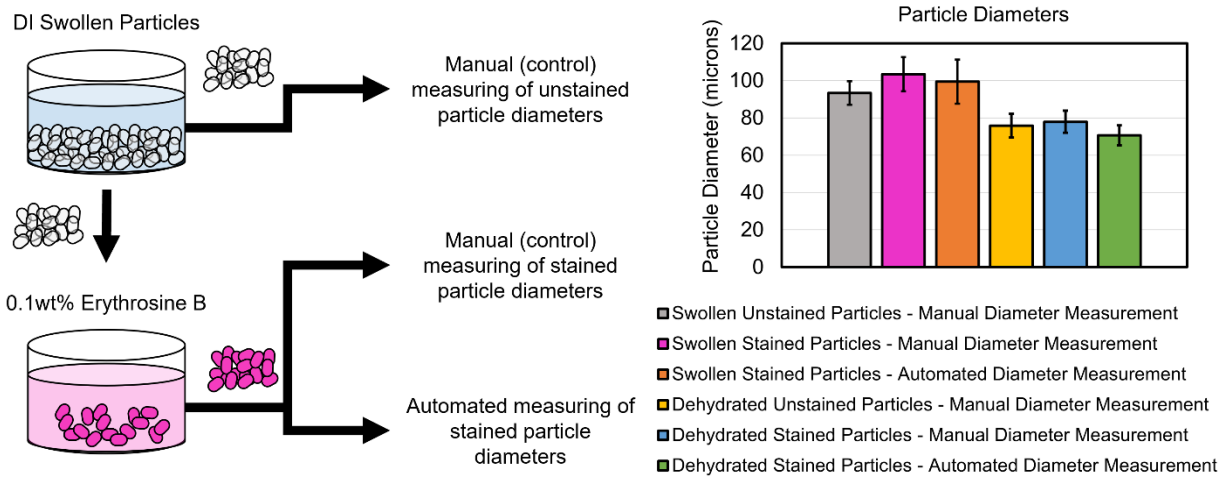


Figure C.4: Control tests of particle measurements. Left: schematic cartoon of microparticle preparation for staining and microscopy measurements. Right: average particle diameter in microns for swollen and dried particles.

Water Content in Mixed Substitution Networks

Water content in mixed substitution microparticles and bulk networks was conducted following methods detailed in the main text. **Equation 4.1** (main text) was used to determine the water content of the microparticle networks from their average wet and dry diameters, in line with prior samples. Similarly, the water content of bulk networks was determined by measuring the wet and dry diameters of punch samples and computing the volume fraction of water in line with **Equation 4.1.** Water content in bulk and microparticle networks with mixed amine substitutions for varied crosslinker content is displayed in **Figure C.5**.

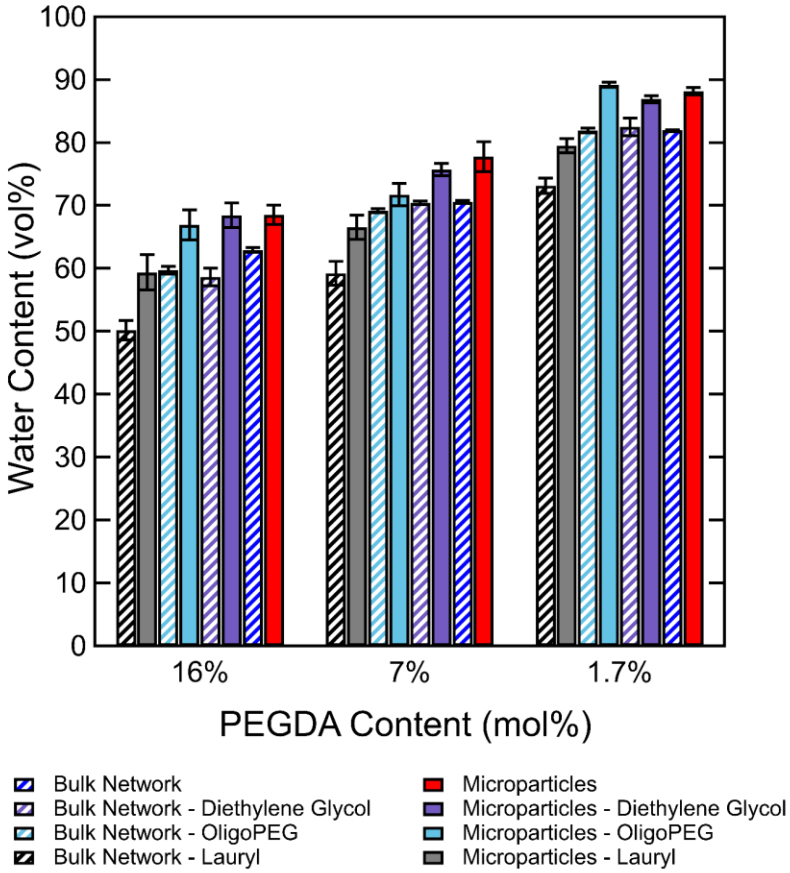


Figure C.5: Water volume fraction for bulk and microparticle networks with varied PEGDA contents, water contents, and side chain functionalities. Microparticle networks were prepared in flow synthesis and mixed functionality materials were substituted with 4-amino-TEMPO and a secondary amine at stoichiometric ratios listed in **Table C.2**. Bulk networks were prepared between quartz plates (250 microns thick) and substituted following above procedures, with mixed functionality networks substituted using ATMP and a secondary amine at the stoichiometric ratios listed in **Table C.2**.

Microparticle Loading:

Polymer microparticles were loaded into EPR capillaries using combined suction and packing of microparticles from plastic syringes connected via simple connectors of PDMS, Tygon, or equivalent. In a representative loading, a section of Tygon tubing could be cut to

approximately 0.5-1 cm in length and quartered. A channel could be punched from the section using an 18-gauge blunt tipped, stainless steel dispensing needle and the capillary could be connected in one end. A 25-gauge conical plastic pipette tip could be installed in the syringe and connected at the opposite end. The assembly was checked for water flow via simple withdrawal and dispensing of deionized water, and microparticles could be suctioned up from a solution with mild agitation. Capillaries were filled completely to provide consistent particle numbers and decrease error during EPR measurements. Filled capillaries were stored submerged in DI water prior to sealing and EPR measurement.

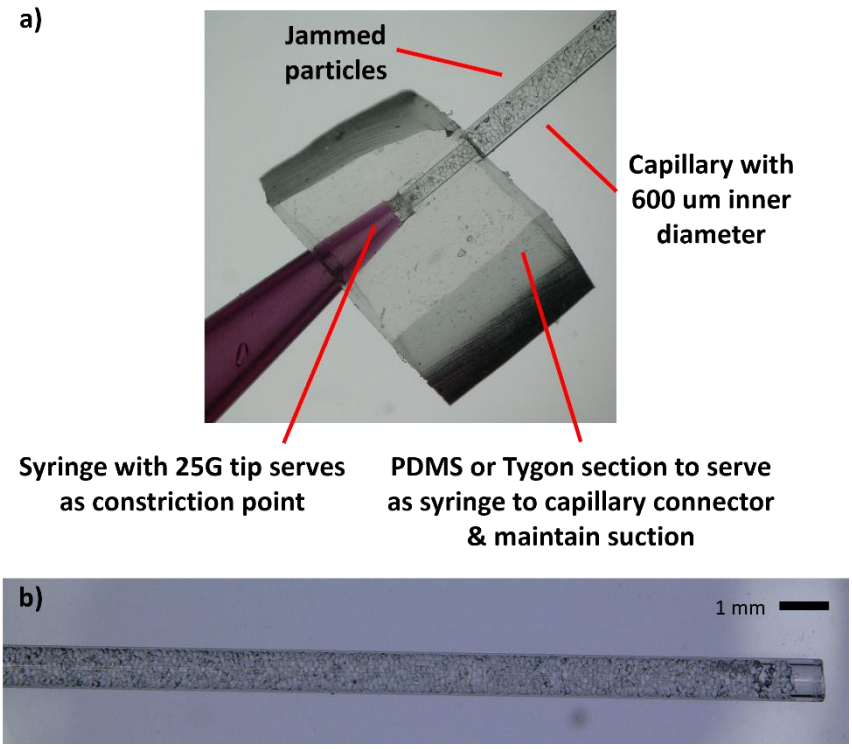


Figure C.6: (a) Optical microscope image of microparticle loading assembly with conical pipette tip, Tygon connector, and loaded capillary. (b) Optical microscope image of capillary filled with microparticles over long length-scales reproduced from main text **Figure 4.1**.

EPR fitting to extract rotational correlation times

In addition to sensing water dynamics through ODNP, spin labels are sensitive to changes in label environment by lineshape analysis of cw-EPR spectra. By fitting experimental cw-EPR spectra to known dynamical models[3], the rotational correlation time, τ_c, of the spin label may be determined which describes the time in which the label rotates and loses correlation to its initial orientation relative to the applied magnetic field. cw-EPR lineshape analysis has been successfully applied to study dynamics of tau protein[4], T4 lysozyme protein[5], polymer micelles[6], and self-assembled nanoribbons[7]. For spin labels tethered to the acrylate backbone of cross-linked PEGDA, τ_c reflects on the polymer backbone mobility, or rigidity, in its hydrated environment. **Figure C.7a** displays the experimental cw-EPR spectra and the two-component fits for the spin-labeled, cross-linked PEGDA networks studied in this work. The fitting parameters are found in **Table C.3 and C.4**. As the crosslinker content of the network decreases, thus expanding its swelling, the cw-EPR lineshape changes such that the percent population of the "faster" component increases with the amount of network swelling (**Figure C.7b**). This indicates that networks with lower crosslinker contents absorb more water and contain more mobile polymer chains. This is expected in part due to increasing distances between crosslinks with decreasing crosslinker content, as networks transition from star-like microstructures at high PEGDA content to more brush-like structures with decreasing crosslinker content as observed in similar systems[1]. The mobility of the network chains, in addition to the irregular network microstructure may explain why fixed obstruction-based diffusion models such as Mackie-Meares fail to completely capture ODNP water diffusion trends in PEGDA hydrogels (see **Appendix C**). Water's ability to navigate

through the irregular network structure, in addition to some mobility from the polymer chains, both aid in the rapid water transport through the material.

Table C.3. EPR fitting parameters used in Multicomponent which were kept constant. 1 and 2 subscripts indicate the first and second component for the fit. When unspecified, it was used for both components.

g	A_1 **(G)**	A_2 **(G)**	R_1	R_2	βD_2	$C_{20,2}$
[2.00781 2.00581 2.00231]	[5.85 6.15 37.65]	[0.95 1.25 32.75]	7.913	7.205	36°	0.4778

Table C.4. EPR fitting parameters used in Multicomponent which were varied between sample spectra of varying mol% PEGDA composition. 1 and 2 subscripts indicate the first and second component for the fit.

Mol% PEGDA	$population_1$	$population_2$	**Fit error**
1.7%	98.59%	1.41%	5.65×10^{-4}
7%	90.65%	9.35%	4.18×10^{-4}
16%	71.80%	28.20%	6.14×10^{-4}
37%	70.39%	29.61%	6.32×10^{-4}
92%	63.58%	36.42%	1.00×10^{-3}

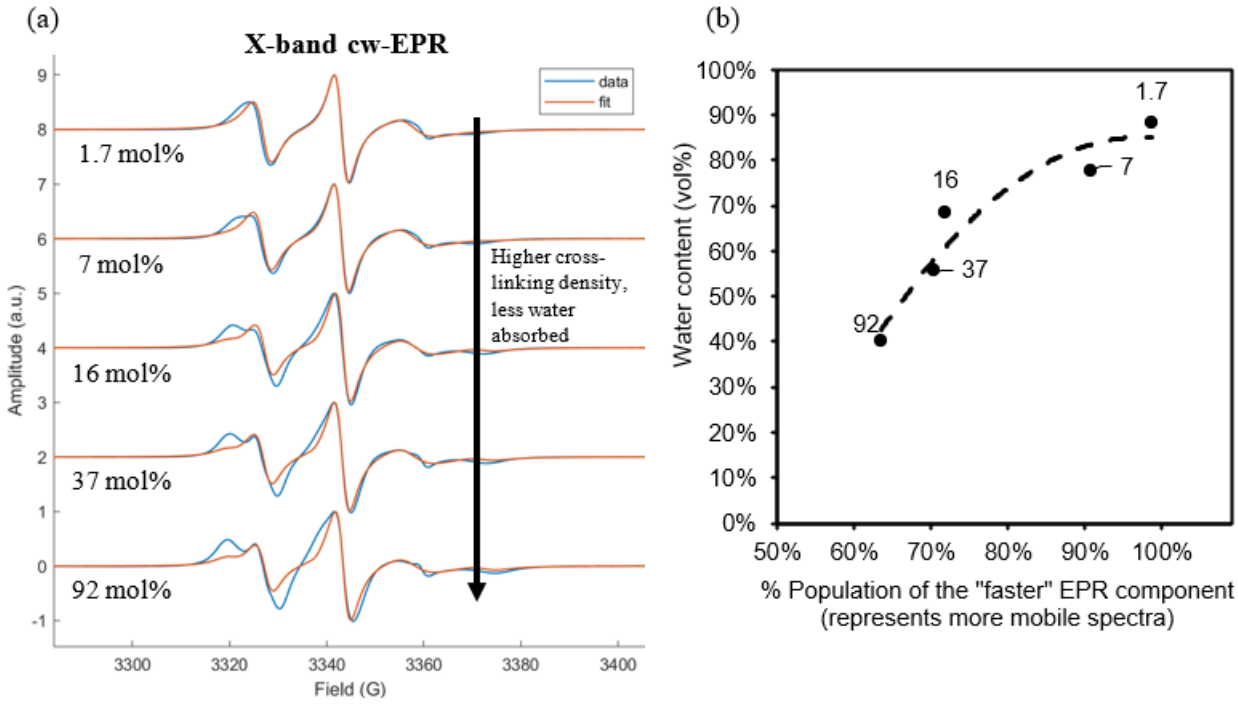


Figure C.7. (a) Experimental X-band cw-EPR spectra (blue) and fit (orange) of spin-labeled, cross-linked PEGDA microparticles of varying crosslinker composition. (b) Absorbed water content in the networks scale with the fitted population of the EPR component with a faster rotational correlation time (component 1), which represents an EPR spectrum of a spin label environment with greater rotational mobility. Data labels indicate the PEGDA monomer composition (mol%) and the dashed line is a polynomial fit to guide the eye.

ODNP Data Tables and Results

Table C.5. ODNP results for cross-linked PEGDA microparticles with TEMPO amines only. Error bars represent one standard deviation on the mean of three experimental repeat values.

Mol% PEGDA	$T_1(0)$ (s)	$T_{1,0}(0)$ (s)	k_σ $(s^{-1}M^{-1})$	k_ρ $(s^{-1}M^{-1})$	ξ	D_{ODNP} $(10^{-6}\ cm^2/s)$
1.7%	1.05 ± 0.03	1.95 ± 0.06	64.8 ± 0.6	713 ± 70	0.103 ± 0.010	8.35 ± 0.73
7%	0.74 ± 0.02	1.55 ± 0.01	69.9 ± 1.7	854 ± 25	0.092 ± 0.003	7.56 ± 0.21
16%	0.54 ± 0.05	1.08 ± 0.13	64.3 ± 6.3	928 ± 99	0.078 ± 0.005	6.60 ± 0.36
37%	0.60 ± 0.03	1.31 ± 0.15	52.4 ± 1.1	1021 ± 59	0.058 ± 0.002	5.26 ± 0.16
92%	0.63 ± 0.03	0.95 ± 0.02	46.3 ± 1.6	1434 ± 316	0.038 ± 0.007	3.93 ± 0.49

Table C.6. ODNP parameters for cross-linked PEGDA microparticles with mixed amine installations. Abbreviations: diethylene glycol (DEG), triethylene glycol ether (OligoPEG). Error bars represent one standard deviation on the mean of three experimental repeat values.

Mol% PEGDA	Secondary amine	$T_1(0)$ (s)	$T_{1,0}(0)$ (s)	k_σ $(s^{-1}M^{-1})$	k_ρ $(s^{-1}M^{-1})$	ξ	D_{ODNP} $(10^{-6}\ cm^2/s)$
1.7%	DEG	1.32 ± 0.14	2.06 ± 0.07	77.9 ± 1.6	897 ± 360	0.087 ± 0.015	7.20 ± 0.10
1.7%	OligoPEG	1.54 ± 0.10	1.98 ± 0.04	78.3 ± 5.5	682 ± 244	0.115 ± 0.047	9.36 ± 0.65
1.7%	Lauryl	1.27 ± 0.09	1.64 ± 0.46	54.2 ± 4.2	927 ± 269	0.059 ± 0.014	5.31 ± 0.96
7%	DEG	1.02 ± 0.03	1.81 ± 0.54	76.5 ± 5.0	978 ± 106	0.078 ± 0.004	6.62 ± 0.27
7%	OligoPEG	1.03 ± 0.04	1.52 ± 0.14	73.7 ± 0.4	638 ± 90	0.115 ± 0.015	9.22 ± 0.11
7%	Lauryl	1.12 ± 0.04	1.44 ± 0.05	50.9 ± 2.6	934 ± 135	0.055 ± 0.006	5.05 ± 0.37
16%	DEG	0.76 ± 0.03	1.35 ± 0.20	61.1 ± 3.4	819 ± 97	0.075 ± 0.010	6.38 ± 0.68
16%	OligoPEG	1.07 ± 0.10	1.52 ± 0.14	56.9 ± 1.4	521 ± 211	0.109 ± 0.038	8.88 ± 0.14
16%	Lauryl	1.11 ± 010	1.29 ± 0.07	41.6 ± 4.6	801 ± 192	0.052 ± 0.083	4.88 ± 0.78

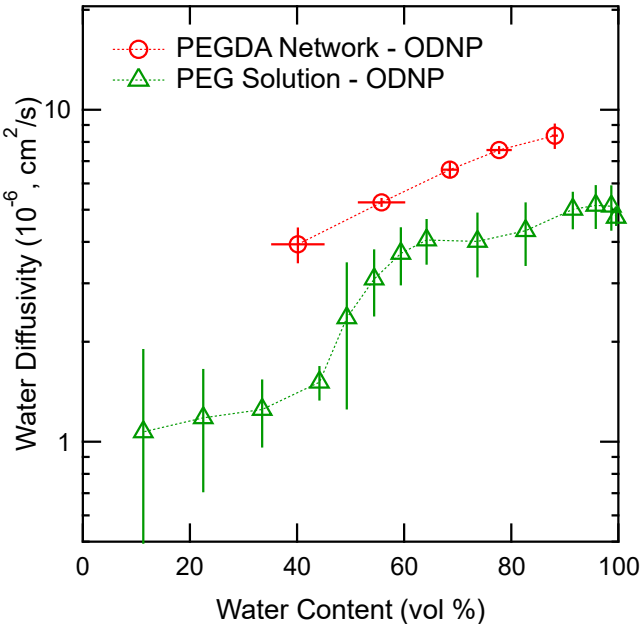
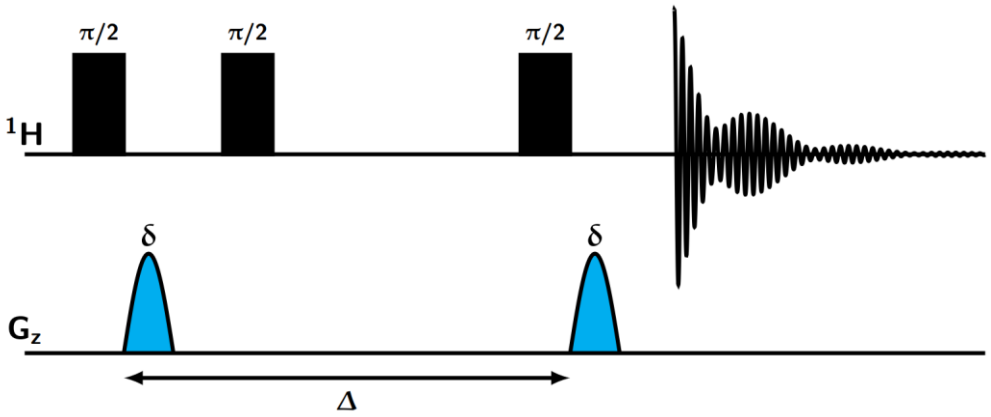


Figure C.8: ODNP water diffusion coefficients near the spin label tethered to the acrylate backbone in cross-linked PEGDA microparticles (open red circles) and near the chain end of linear PEG in aqueous solution (550 Da) (green open triangles), reproduced from prior work[8].

PFG-NMR Characterization

Experimental details for PFG-NMR characterization are described in the Methods section (main text), with additional figures to demonstrate the technique provided below.



Scheme C.2: Visualization of the stimulated-echo pulse sequence employed in this work for PFG-NMR measurements.

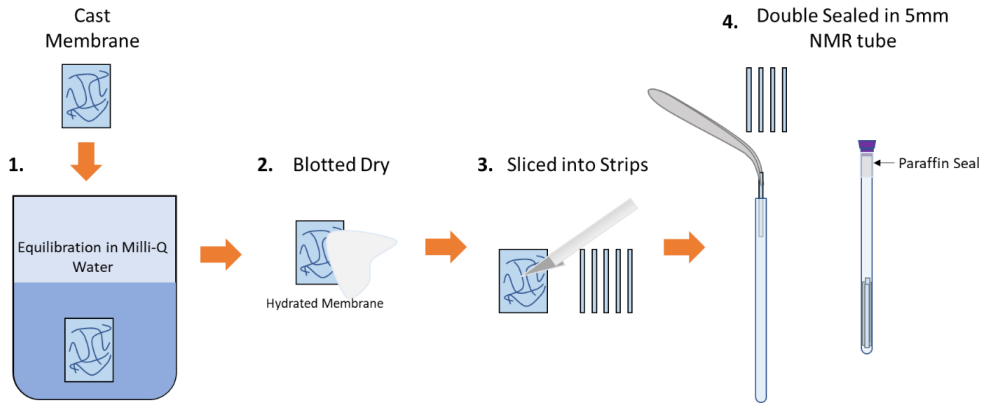


Figure C.9: Sample preparation for PFG-NMR measurements, following the water equilibration steps (1) membranes were immediately blotted dry (2) and sliced into thin slivers (3), then subsequently double sealed with into 5 mm NMR tubes (4).

Diffusion models for PEGDA water transport

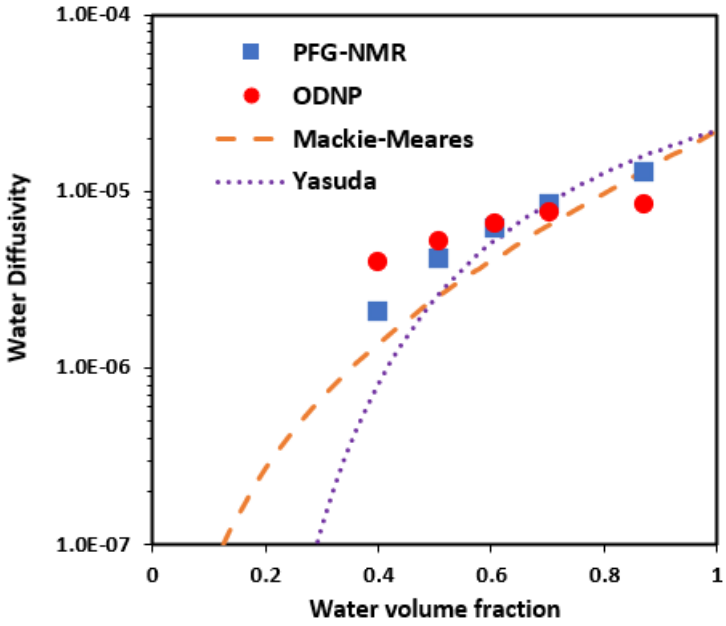


Figure C.10. Comparison of water diffusion coefficients from PFG-NMR and ODNP experiments to conventional, obstruction-based diffusion models: Mackie-Meares and Yasuda theory. The Mackie-Meares model has been used extensively in membrane literature to model solute and solvent transport in cross-linked polymers, including PEGDA.[9,10] Measured water diffusion coefficients show positive deviation from predictions, possibly due to PEGDA's irregular network structure or the mobility of the network chain, as measured by cw-EPR lineshape analysis, which breaks down the assumption of polymer volume being a fixed obstruction to the path of water diffusion.

References

(1) Shannon, D. P.; Moon, J. D.; Barney, C. W.; Sinha, N. J.; Yang, K.-C.; Jones, S. D.; Garcia, R. V.; Helgeson, M. E.; Segalman, R. A.; Valentine, M. T.; Hawker, C. J. Modular Synthesis and Patterning of High-Stiffness Networks by Postpolymerization Functionalization with Iron–Catechol Complexes. *Macromolecules* **2023**, *56* (6), 2268–2276. https://doi.org/10.1021/acs.macromol.2c02561.

(2) Moon, J. D.; Sujanani, R.; Geng, Z.; Freeman, B. D.; Segalman, R. A.; Hawker, C. J. Versatile Synthetic Platform for Polymer Membrane Libraries Using Functional Networks. *Macromolecules* **2021**, *54* (2), 866–873. https://doi.org/10.1021/acs.macromol.0c02414.

(3) Budil, D. E.; Lee, S.; Saxena, S.; Freed, J. H. Nonlinear-Least-Squares Analysis of Slow-Motion EPR Spectra in One and Two Dimensions Using a Modified Levenberg–Marquardt Algorithm. *J. Magn. Reson. A* **1996**, *120* (2), 155–189. https://doi.org/10.1006/jmra.1996.0113.

(4) Pavlova, A.; Cheng, C.-Y.; Kinnebrew, M.; Lew, J.; Dahlquist, F. W.; Han, S. Protein Structural and Surface Water Rearrangement Constitute Major Events in the Earliest Aggregation Stages of Tau. *Proc. Natl. Acad. Sci.* **2016**, *113* (2), E127–E136. https://doi.org/10.1073/pnas.1504415113.

(5) Fleissner, M. R.; Bridges, M. D.; Brooks, E. K.; Cascio, D.; Kálai, T.; Hideg, K.; Hubbell, W. L. Structure and Dynamics of a Conformationally Constrained Nitroxide Side Chain and Applications in EPR Spectroscopy. *Proc. Natl. Acad. Sci.* **2011**, *108* (39), 16241–16246. https://doi.org/10.1073/pnas.1111420108.

(6) DeStefano, A. J.; Nguyen, M.; Fredrickson, G. H.; Han, S.; Segalman, R. A. Design of Soft Material Surfaces with Rationally Tuned Water Diffusivity. *ACS Cent. Sci.* **2023**, *9* (5), 1019–1024. https://doi.org/10.1021/acscentsci.3c00208.

(7) Lindemann, W. R.; Christoff-Tempesta, T.; Ortony, J. H. A Global Minimization Toolkit for Batch-Fitting and X2 Cluster Analysis of CW-EPR Spectra. *Biophys. J.* **2020**, *119* (10), 1937–1945. https://doi.org/10.1016/j.bpj.2020.08.042.

(8) Moon, J. D.; Webber, T. R.; Brown, D. R.; Richardson, P. M.; Casey, T. M.; Segalman, R. A.; Shell, M. S.; Han, S. Nanoscale Water–Polymer Interactions Tune Macroscopic Diffusivity of Water in Aqueous Poly(Ethylene Oxide) Solutions. *Chem. Sci.* **2024**, *15* (7), 2495–2508. https://doi.org/10.1039/D3SC05377F.

(9) Nordness, O.; Moon, J. D.; Marioni, N.; Zofchak, E. S.; Richardson, P. M.; Landsman, M. R.; Katz, L. E.; Hawker, C. J.; Ganesan, V.; Segalman, R. A.; Clément, R. J. Probing Water and Ion Diffusion in Functional Hydrogel Membranes by PFG-NMR. *Macromolecules* **2023**, *56* (12), 4669–4680. https://doi.org/10.1021/acs.macromol.3c00306.

(10) Jang, E.-S.; Kamcev, J.; Kobayashi, K.; Yan, N.; Sujanani, R.; Dilenschneider, T. J.; Park, H. B.; Paul, D. R.; Freeman, B. D. Influence of Water Content on Alkali Metal

Chloride Transport in Cross-Linked Poly(Ethylene Glycol) Diacrylate.2. Ion Diffusion. *Polymer* **2020**, *192*, 122316. https://doi.org/10.1016/j.polymer.2020.122316.